Permanent Magnet Based Magnetic Resonance Sensors

STEVEN THOMAS PARSLOW

A thesis submitted in partial fulfilment of the requirements of Nottingham Trent University for the degree of Doctor of Philosophy

September 2019

DECLARATION

ACKNOWLEDGEMENTS

Firstly, I would like to express my gratitude towards Nottingham Trent University and the Vice Chancellor's PhD Bursary scheme for funding my PhD research project. My supervisory team, Michael Newton and Robert Morris, have been a constant source of support, ideas and inspiration throughout this project. Thanks to Theodore Hughes-Riley for his support in the early years of the project and other members of the physics team for being instrumental in aiding my understanding and innovating new developments.

A huge thank you to the physics technicians, especially Dave Parker who was always there to help with engineering concepts and the times I accidentally got multiple rare earth magnets stuck together (sorry!).

A special thanks to my family including my parents, grandparents and siblings for their continual support and an even greater thank you to my partner Jennifer Evans for her unconditional love and support during my PhD and constantly believing in me even through my "this paper is due in 2 days" mood.

Another huge thank you to my three best friends Daniel Polak, James Town and Thomas Lees for the support, the laughs and the memes…

Finally, I would like to thank all of the friends I've made along with way in CELS003 and ERD170 who have kept the workplace a social and (mostly) sane environment and everyone else who has been involved in this project.

ABSTRACT

In 2006 patent EP2069769A2 described using magnetic resonance (MR), instead of fluorescence, as the detection method for microarrays. This covered the concept of binding magnetic particles, such as Superparamagnetic Iron Oxide (SPIO), to a surface in order to change the MR signal that would normally be expected from the fluid covering the surface to which the particles were bound. In this thesis, measurement techniques are presented, utilising both pulsed and continuous wave nuclear magnetic resonance (CWNMR), where surface bound magnetic nanoparticles disrupt the MR signal that would normally be detected in the fluid covering the surface, using low magnetic field sensors constructed from permanent magnets. A pulsed technique is presented with a sensor constructed using permanent magnets in a Halbach arrangement. Using a technique called Magnetic Resonance Disruption (MaRDi), it is shown that the T_2^{eff} relaxation time of a test liquid, polydimethylsiloxane (PDMS), reduces as the proportion of the surface area covered with SPIO increases. In addition, a linear decrease in the signal amplitude from the PDMS as a function of SPIO coverage, which is observed both for an integral over 4096 NMR echoes and even just in the first echo. The latter result suggests the potential for a technique to be developed with simplified and low cost electronics. A CWNMR technique is also presented by revisiting the Look and Locker's tone-burst experiments but modified to use a commercial marginal oscillator. Though observing the transient effect when a sweep coil is switched on, a parameter T_x can be determined that is related to relaxation time T_1 that can subsequently be calculated with the aid of calibration samples. This Transient Effect Determination of Spin Lattice relaxation time (TEDSpiL) was automated using low cost microcontrollers. A potential industrial application of detecting moisture uptake through improperly stored dehydrated milk powder is also presented.

PREFACE

This thesis is divided into three chapters detailing all work undertaken in the development of the various table top systems and NMR experiments performed with them.

Chapter 1 provides the reader with a basic introduction to the phenomenon of NMR as well as giving a background into the different types of instruments, both low and high field, which can be used to perform an NMR experiment. It further details the fabrication and functionalisation of different types of available nanoparticles.

Chapter 2 focuses on the experiments and designs incorporating pulse sequencing and Fourier Transformation NMR. It explains the various steps taken from system optimisation through to assay design, finishing with an example of a working magnetic resonance disruption (MaRDi) technique, the data for which was published in Analytical Methods.

Chapter 3 focuses on the experiments and designs incorporating continuous-wave instrumentation and the different electronic systems that were used to perform measurements, including a Teensy™ microcontroller setup. It includes a number of techniques and the development of Arduino™ code utilised by the final microcontroller system. A proof of concept for the early system is presented in Magnetic Resonance in Chemistry where the details of the final system and its applications in food science were published in The 5th International Electronic Conference on Sensors and Applications and Magnetic Resonance in Chemistry respectively.

Appendix A contains the final working code used in each of the Teensy™ microcontrollers (both the 3.5 and 3.6) as well as scripts used in MATLAB™ analysis.

Appendix B hosts copies of all 4 peer-reviewed manuscripts.

TABLE OF CONTENTS

CHAPTER 1: AN INTRODUCTION TO NMR

1.1. The Physics of Nuclear Spin, Precession and Relaxation

1.1.1. Nuclear Spin

In an atom, nuclear spin is an intrinsic form of angular momentum possessed by elementary nuclei (Abragam and Hebel, 1961; Blümich, 2005; Ernst et al., 1989). Each nuclear spin has a magnetic moment, which is associated with the angular momentum of the nucleus. The phenomenon known as magnetic resonance requires nuclei with a non-zero spin which occurs in nuclei with an odd mass number. Protons and neutrons are fermions. In particle physics, a fermion is a particle that follows Fermi–Dirac statistics and generally has half odd integer spin (Thomson, 2013). As such, these particles are composed of "up" (spin ½) and "down" (spin -½) quarks with a proton consisting of two "up" and one "down" and a neutron containing one "up" and two "down. When placed into a magnetic field, multiple spin states can exist based on the spin number of the nucleus. The spin quantum number describes the orientation of the intrinsic angular momentum of an elementary particle. An example of this is for the proton (^{1}H), which has a spin of ½, existing with one spin up and one spin down, where one aligns with the magnetic field and the other opposes it. Two or more particles with spins having opposite signs can pair up to eliminate the observable manifestations of spin such as in helium. In nuclear magnetic resonance, it is unpaired nuclear spins that are of note.

The energy difference between two spin states increases as the strength of the external field is increased and the frequency (ν_0) at which nuclear spins precess is proportional to the strength of the magnetic field (B_0) (Equation 1). The gyromagnetic ratio (γ) has a constant value depending on the nuclei. For hydrogen, this value is 42.58 $MHzT^{-1}$.

Equation 1:

$$\boldsymbol{\omega_0 = 2\pi\nu_0 = \gamma B_0}$$

1.1.2 Quantum NMR: Energy Levels, Transitions and the Zeeman Effect

When a proton is placed within an external magnetic field (B_0), the spin vector aligns with the external applied field. There are two possible configurations that can occur; a high energy state where the North Pole follows the direction of the applied field and a low energy state where the North Pole is aligned in the opposite direction to the applied field.

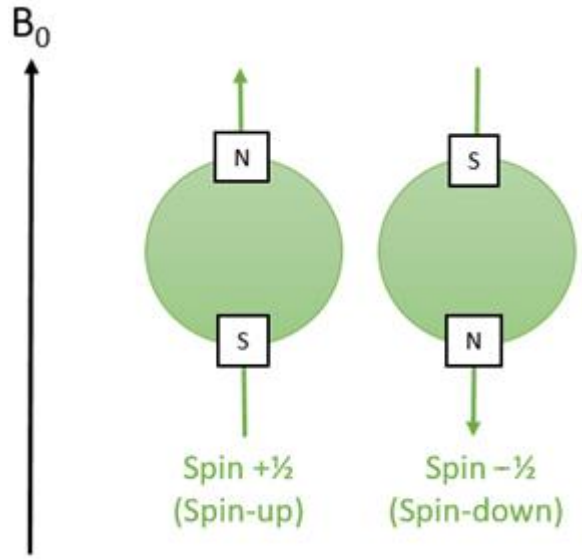

Figure 1: A diagram showing how the spin state of a nucleus can be aligned with and against an externally applied magnetic field. Spin +1/2 follows an N-N-S-S alignment where the north pole of the nucleus points in the same direction as the North Pole of the externally applied field. Spin -1/2 follows an N-S-N-S alignment where the spin of the nucleus points in the opposite direction to the external field.

Particles can transition between these two energy states though the absorption of energy from a photon. A low energy state particle can transition to a high energy state if the energy received exactly matches the energy difference between the two spin states. As the energy of a photon is related to its frequency, $\boldsymbol{\nu}$, and by Planck's constant, h, the energy, E, of the photon can be calculated. The frequency of the photon required for particle transition is referred to as the resonance or Larmor frequency.

Equation 2:

$$\boldsymbol{E = h\nu}$$

Determining whether a spin aligns parallel or anti-parallel with the direction of the externally applied magnetic field is a probabilistic question successfully described using Boltzmann statistics. At room temperature, and in the absence of an externally applied magnetic field, there is a higher number of spins in the lower energy state (N^-) than there is in the high energy state (N^+). These statistics can be demonstrated using the following equation:

Equation 3:

$$\mathbf{N^-/N^+ = e^{-E/kT}}$$

The ratio of spin states is denoted as N^-/N^+; E is the energy difference between the spin states; k is the Boltzmann constant (1.3805×10^{-23} JK^{-1}); and T is the temperature of the system (in Kelvin). The magnitude of the NMR signal can be shown to be proportional to the ratio of the population difference between states. As such, improvements in NMR signal can be obtained by increasing the energy difference between spin states through applying a stronger external magnetic field, or through lowering the temperature of the system. Even though the population difference can be miniscule (1 particle per 10,000), even at very high fields or very low temperatures, spectrometers are still capable of detecting these small exchanges of energy.

1.1.3. Classical NMR: Rotating Frames, Bulk Magnetisation and Larmor Precession

So far NMR has been described through quantum mechanics in the form of Zeeman splitting and transitional energy levels, but it is convenient to describe the precession of a nucleus in a frame of reference rotating at the Larmor frequency to provide a classical description of NMR to assist in the description of pulsed techniques.

To better explain the process of precession and how particles behave in a magnetic field, spin is often thought of as a magnetic moment vector causing a nucleus to behave like a miniscule bar magnet, or more precisely, a magnetic moment. When

considering an NMR experiment, it is not just a single nucleus which is observed, but the net effect of all NMR capable nuclei. If all magnetic moments were to point in different directions to one another, the magnetic fields would cancel each other out and there would be no overall net effect. However, when at equilibrium, the moments align in a way that provides a net magnetic field in the direction of the applied external field (B_0). This net magnetic field is known as the bulk magnetisation of the sample. It is possible to represent the magnetization by a vector in the direction of the externally applied magnetic field. The magnetization vector can be shown against coordinates *x*,*y*,*z* with it on the *z*-axis of a fixed or laboratory frame.

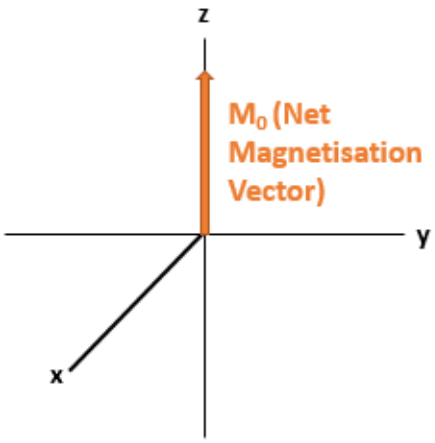

Figure 2: When there is a larger number of spins aligned with the external magnetic field than against it, this leads to a net magnetisation vector in the direction of this field.

This bulk magnetisation vector can be tilted through the application of external energy supplied at the Larmor frequency. Due to the gyromagnetic ratio of various nuclei, the frequency of this energy sits within the radiofrequency band of electromagnetic energy and as such is known as radiofrequency (RF) energy. This RF energy is applied over a short period of time and is termed an RF pulse. The spins respond to this pulse of energy, causing the net magnetisation vector to rotate about the axis of RF pulse, which is generally given the notation B_1 to help distinguish it from the original magnetic field B_0. The angle of rotation, θ, is

proportional to the length of time that the field is switched on (τ) and the magnitude of the field (B_1).

Equation 4:

$$\theta = 2\pi\gamma\tau B_1$$

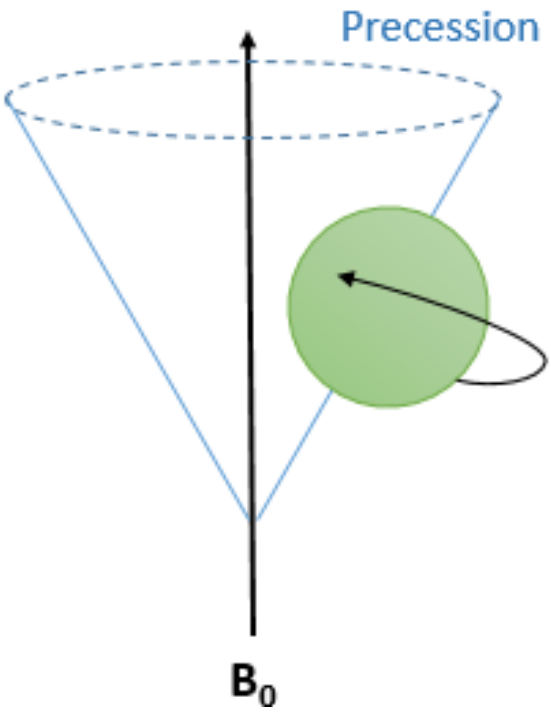

Figure 3: A spinning proton precesses about an externally applied magnetic field (B0) after its magnetisation is tilted by another field (B1) applied perpendicular to the original field direction.

Once the B_1 field is switched off, the system returns to equilibrium and the bulk magnetisation vector returns to aligning itself with B_0. The time it takes to return to equilibrium is proportional to the sample's NMR longitudinal relaxation time.

1.1.4. Bloch Equations and Relaxation

The spin-lattice (longitudinal) relaxation time T_1 is simply the rate at which the magnetisation returns to its equilibrium value, which can be relatively long due to the inability to transfer energies of NMR transitions into thermal energy. The rate of change of the magnetization is given by the Bloch equations (Bloch et al., 1946)

shown below where M_z is the magnetisation in the direction of the externally applied field, referred to as the "z axis", and M_0 is the initial magnetisation:

Equation 5:

$$\frac{\delta M_z}{\delta t} = \frac{M_0 - M_z}{T_1}$$

This can be integrated with $M_z = -M_0$ at t=0 to provide:

Equation 6:

$$M_z = M_0(1 - 2e^{\frac{-t}{T_1}})$$

The spin-spin (transverse) relaxation time T_2 describes the rate of magnetization loss within the system. By applying RF energy at the Larmor frequency, the nuclear spins can be aligned in the x,y plane instead of the initial z axis. Over time, the nuclear spins begin to dephase and the net magnetisation vector begins to decrease due to circumstances such as field inhomogeneity and/or interactions between the spins. This is known as a decay of the transverse magnetisation.

T_1 is related to T_2 as an increase in magnetization about the z axis without a decrease in the magnetization in x,y plane is impossible.

The transverse relaxation time is given in another Bloch equation below where M_x and M_y are the magnetisations in the X and Y plane respectively:

Equation 7:

$$\frac{\delta M_{xy}(t)}{\delta t} = -\frac{M_{xy}}{T_2}$$

This can be solved for Mxy to provide:

Equation 8:

$$\mathbf{M_{xy} = M_0 e^{\frac{-t}{T_2}}}$$

There are two major factors which contribute to the decay of transverse magnetisation. Firstly, molecular interactions within the sample can result in losses of magnetisation but also field inhomogeneity where spins in a sample will possess a different Larmor frequency as a function of position within the B_0 field, leading to destructive interference. It is the combination of these two factors which causes the loss of transverse magnetisation and this combined time constant is referred to as T_2^*.

1.2. NMR Hardware

1.2.1. Magnets

When it comes to a complete NMR experiment, the magnetic field is often one of the most expensive components. The magnets used in NMR systems are typically superconducting electromagnets, achieving field strengths typically in the range of 1.5-7T, although the technology for producing strong static magnetic fields in the range of 0.1-0.5T has become more developed in recent years with Neodymium (NdFeB) and Samarium Cobalt (SmCo) permanent magnets. Superconducting wire has a resistance close to zero when it is cooled using cryogenic fluids such as liquid helium to bring the temperature of the magnet close to absolute zero. Once current flow occurs within the superconducting electromagnet it will continue to flow whilst the temperature remains close to absolute zero, although some small losses do occur even with the infinitesimally small internal resistance of the electromagnet. To achieve such high magnetic field strengths, the length of wire in the superconducting electromagnet is typically several miles and is contained within a large Dewar with the liquid helium which is generally surrounded by a secondary Dewar filled with liquid nitrogen to act as a thermal buffer as liquid nitrogen is cheaper, easier to produce and more widely available. Vacuum shielding is also introduced to ensure thermal losses are reduced as much as possible. The result is a

large, expensive and heavy device but one that can perform many highly sensitive NMR experiments for both clinical and industrial applications.

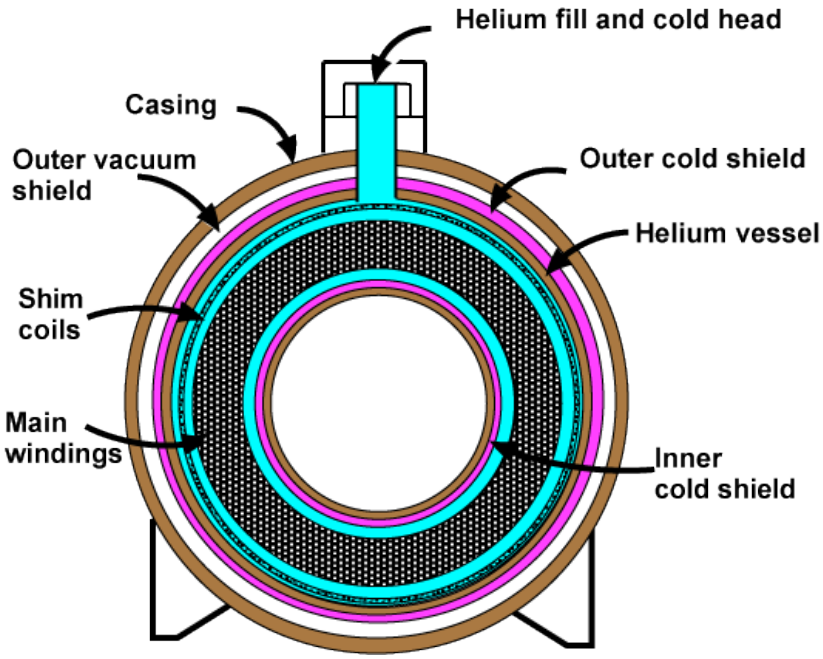

Figure 4: A cutaway diagram of a superconducting, cryogen-cooled electromagnet. There are numerous components dedicated to keeping the temperature of the superconducting copper wire as close to absolute zero as possible to ensure no resistive losses occur. Liquid helium and nitrogen vessels hold the cryogenic fluids whilst vacuum shielding exists to reduce thermal convection to the surroundings. These devices often contain "recyclers" to capture the gaseous elements as the cryogenic material boils off. (Elster, 2019)

As mentioned previously, rare-earth permanent magnets have become widely reported in several NMR devices (Danieli et al., 2010; Lee et al., 2008; Sun et al., 2013). NdFeB magnets, made from an alloy of neodymium, iron and boron to form an $Nd_2Fe_{14}B$ crystalline structure, are the strongest type of permanent magnets commercially available. Production of these magnets is often divided into two categories; sintered NdFeB and bonded NdFeB.

Sintered NeFeB magnets are prepared by melting the raw materials in a furnace and then casting and cooling to form ingots. These ingots are smashed and milled into a powder before sintering into dense blocks. These blocks are heat treated, shaped and then surface treated with materials such as a nickel-copper mixture, before being magnetised with an electromagnet roughly 3 times stronger than the field

intended for the permanent magnet. Neodymium magnets are graded according to their maximum energy product, which relates to the magnetic flux output per unit volume with higher values indicating stronger magnets. Sintered NdFeB magnets use a widely recognized international classification where their values range from 28 up to 52. The first letter N before the values is short for neodymium, meaning it is a sintered NdFeB magnet. Letters following the values indicate intrinsic coercivity and maximum operating temperatures (positively correlated with the Curie temperature). If there are no letters following the grade (The magnet is just graded 'N52') then the magnet is the standard temperature of neodymium (up to 80 °C or 176 °F). The temperature ratings are standard, with the highest rating given the suffix AH (grading it 'N52AH') which provides the highest operating temperature (220 °C or 428 °F). In 2015, Nitto Denko Corporation of Japan announced their development of a new method of sintering neodymium magnet material (Energy, 2011). The method exploits an "organic/inorganic hybrid technology" to form a clay-like mixture that can be fashioned into various shapes for sintering. Most importantly, it is said to be possible to control a non-uniform orientation of the magnetic field in the sintered material to locally concentrate the field to improve the performance of electric motors. 3D printing technology is also being utilised to print magnets with a range of shapes and field profiles (Domingo-Roca et al., 2018; Huber et al., 2016; Jaćimović et al., 2017).

Bonded NdFeB magnets are produced by combining the quenched magnetic powders with resin binders (epoxy, nylon/polyamide) so they can be manufactured though extrusion or injection allowing them to obtain complex geometries. By controlling the amount of magnetic powder in each point within the manufacturing it is easier to create diverse magnetisation properties.

1.2.2. Magnetic Shims

Magnetic shims correct minor spatial inhomogeneity within a magnetic field. This inhomogeneity can exist for a variety of reasons from the design of the magnetic system, to the proximity of ferromagnetic materials. Shims are designed to either create their own magnetic field, in the case of shim coils or shim magnets, which

can oppose and dispose of field inhomogeneity, or to redirect magnetic flux which is performed with ferromagnetic materials.

In large equipment, shimming is often achieved through the use of coils where the amount of current moving through each coil can be controlled to create a homogenous B_0 magnetic field. The optimum shim settings are deduced by minimising the NMR line width or maximising the time in which a free induction decay (FID) remains coherent. Recently, passive shimming techniques have been explored where a standard inkjet printer can be loaded with magnetic ink to print fixed-strength shims so that the field errors in a 0.5T magnet can be corrected (McDowell, 2018).

1.2.3. Radiofrequency Coils, Tuning and Matching

Radiofrequency (RF) coils are required to produce the B_1 field necessary to create a rotation in the net magnetisation in a pulse sequence and also detect the transverse magnetisation due to precession in the xy plane. RF coils can come in a variety of geometries such as solenoids, saddles and birdcages. Each of these RF coils must resonate at the Larmor frequency of the nucleus under examination within the NMR device. The primary elements within an RF coil are its inductive and capacitive capabilities as the resonant frequency ($\boldsymbol{\nu}$) of an RF coil is determined by its inductance (L) and capacitance (C).

Equation 9:

$$\boldsymbol{\nu = \frac{1}{2\pi\sqrt{LC}}}$$

When a sample is placed within the RF coil the resonant frequency can be altered due to the conductivity and dielectric constant of the sample being observed. If the frequency of the RF coil is different to the Larmor frequency of the observed sample, the net magnetisation will not be rotated as efficiently producing less transverse magnetisation and less signal and poor signal-to-noise ratio. The RF coil is no use if it can only operate at a single resonant frequency, due the fact that the

larmor frequency of the sample can change slightly. To compensate for this, coils often come with tuning/matching electronics such as variable capacitors or inductors which can be altered. Correct tuning of the RF coil ensures that the probe circuitry is operating at the relevant transmission frequency, where matching ensures that the maximum amount of power arriving at the probe is transmitted towards the coil, minimising reflections. Tuning/matching is generally achieved using a network analyser to produce what is known as a "wobble curve". A network analyser is an instrument that measures the network parameters of electrical networks. More specifically to this example, it measures scattering parameters such as reflection and transmission. When connected to a network analyser a wobble curve is seen which provides a measure for the amplitude of reflected signal against frequency. Using this curve, the tuning/matching electronics can be modified to ensure the RF coil is correctly tuned by ensuring that the dip in the curve is located exactly at the resonant frequency of the observable sample when placed in the B_0 field and also correctly matched by ensuring the depth of the dip is as low as possible which demonstrates a low amount of reflection and in turn a high transmission rate.

1.2.4. Magnetic Field Gradients

Gradient coils are necessary for producing gradients in the B_0 field and are used in more enhanced forms of NMR such as magnetic resonance imaging (MRI). The gradient field slightly distorts the B_0 field into a predictable pattern which changes the resonant frequency of the observable nucleus as a function of its position within the coil effectively spatially encoding the NMR signal. These coils are sat at room temperature and, like the RF coil, can come in a range of geometries such as saddle, Helmholtz and Figure of Eight.

1.3. Compact NMR

1.3.1. Magnets and Instruments

When considering modern electronics, the general trend is that they become smaller and more powerful as time progresses. This is a trend which is commonly

countered by NMR by the belief that only higher fields lead to better instruments as sensitivity increases proportionally with field strength (Abragam and Hebel, 1961; Ernst et al., 1989). As strong magnets are generally large and expensive, access to such devices can often be seen as a privilege.

NMR magnets in the range of 1-5T were commonly used in the early days, but major manufacturers began moving away from such devices as they exhibited inferior performance. However, a range of small NMR devices with field strengths of up to 2T are now being realised which are mobile, cost-effective and portable (Blümich et al., 2008; Danieli et al., 2010, 2009; Eidmann et al., 1996; McDowell and Fukushima, 2008; Perlo et al., 2006; Sillerud et al., 2006). There are a few disadvantages to performing NMR experiments at low field, primarily the low sensitivity due to small differences in thermodynamic equilibrium population of spin states providing a lower net transverse magnetisation vector. Many of these disadvantages can be overcome with a variety of techniques such as hyperpolarisation (Cherubini and Bifone, 2003; Middleton et al., 1995; Möller et al., 2002), polarising spins beyond their equilibrium populations, shimming (Gruetter et al., 1998; Hugon et al., 2010; McDowell, 2018), to improve field homogeneity, and use of pulse sequencing (Carr and Purcell, 1954; Hahn, 1950; Meiboom and Gill, 1958), to compensate for field homogeneity.

There are two principal types of NMR magnet geometry; open and closed (Blümich et al., 2009). Closed magnets accommodate a sample inside a magnet bore and generally achieve higher field strengths and homogeneity. The major disadvantage is that you are limited to the size of the bore when choosing a sample to investigate. Open geometries allow the investigation or larger objects but are much harder to achieve large homogenous fields with due to high field gradients. Both designs can be miniaturised and it's important to understand the requirements of the sensor before selecting the relevant geometry.

One particular example of an open geometry is the NMR Mobile Universal Surface Explorer (MoUSE) (Eidmann et al., 1996; Haber et al., 2011; Perlo et al., 2005, 2004). A static magnetic field is generated by two permanent magnets with anti-parallel magnetisation positioned onto an iron yoke. A solenoidal RF coil is placed within the gap of the two magnets so that the static magnetic field B_0 and RF field B_1 are

orthogonal to each other within a large volume above the surface of the coil. This region is often referred to as the “sensitive slice”. This coil can also be mounted in such a way that the sensitive region can be moved up and down through a sample providing spatial information.

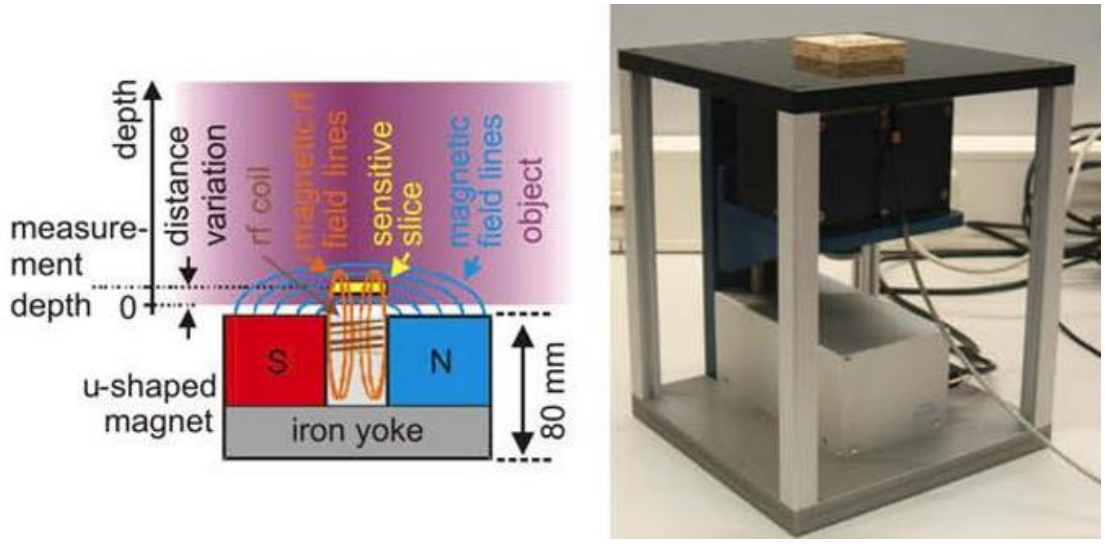

Figure 5: A schematic of an NMR MoUSE. The single-sided geometry provides a small sensitive region in which the field is homogenous in two directions only. A planar RF coil is used to provide NMR measurements from within this sensitive region. (Blümich et al., 2009)

A particularly successful closed geometry is the Halbach sensor (Halbach, 1980; Raich and Blümler, 2004; Soltner and Blümler, 2010). This geometry relies on multiple permanent magnets arranged in a cylindrical pattern to produce a large internal magnetic field whilst cancelling external stray fields to almost zero. The magnetic field direction is transverse to the cylinder axis allowing a simple axial solenoid to be used as an RF coil.

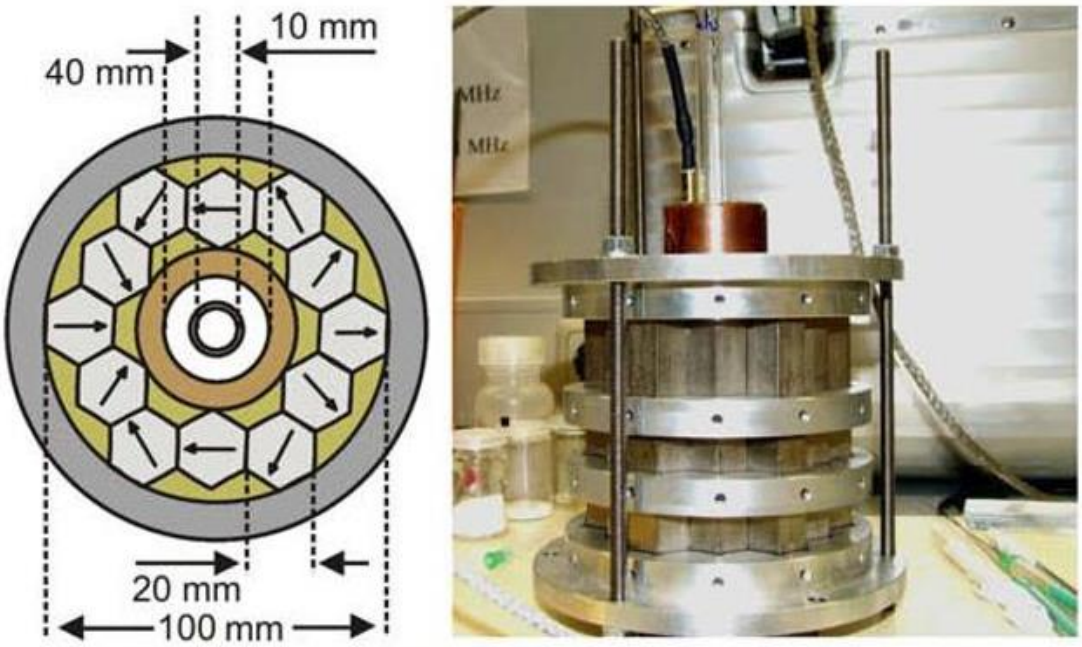

Figure 6: A schematic of a Halbach sensor. The pole direction of the magnets is important to ensure a strong, homogenous field inside the device, whilst also cancelling the external stray fields as much as possible. The NMR coil is a solenoid, positioned inside the homogenous region. (Blümich et al., 2009)

1.3.2. Applications

With many devices, one of the easiest applications for low field sensors is relaxometry which refers to the study and measurement of relaxation variables within NMR. An NMR signal is often detected in the form of echoes such as Hahn echoes, collected from a series of 90° pulses (Eidmann et al., 1996; Hahn, 1950) or CPMG echo trains, collected by a series of 180° refocussing pulses following the initial 90° pulse (Blümich, 2005; Meiboom and Gill, 1958; Perlo et al., 2005).
An inverse Laplace transform of the echo train envelope demonstrates how it is composed of the distribution of different relaxation times, with each peak identifying a specific relaxation environment. Relaxation measurements have been optimised in counting cells that have been labelled with ferromagnetic nanoparticles (Koh et al., 2008; Lee et al., 2008; McDowell and Fukushima, 2008; Sillerud et al., 2006), demonstrating great promise in the area of biomedical research. Unilateral sensors have shown potential in depth profiling of layered objects (Perlo et al., 2006) in both biological systems, such as human skin (Blümich et al., 2008), and man-made objects such as artwork (Haber et al., 2011).

Diffusion can be measured with high accuracy using unilateral sensors like the NMR MoUSE. Because of the high field gradients found in unilateral sensors, short position-encoding times are required to mark the initial and final positions in displacement measurements. If too much time passes between the original 90° and successive refocussing pulses, the nuclei under investigation can diffuse from its original position, moving into a region with a differing magnetic field strength which in turn will change its larmor frequency.

Imaging is another application possible with low field sensors, although they require higher field uniformity than what is needed for relaxometry. As such, simple Halbach sensors need to be shimmed, which has been achieved and tested for imaging plants and fluid flow through a pipe (Danieli et al., 2009). Slice-selective 2D images have also been obtained using a unilateral magnet with a profile similar to the NMR MoUSE (Perlo et al., 2004).

Finally, spectroscopy is another application for low field sensors. Spectroscopy places the highest demand on field homogeneity, requiring a long FID to achieve high enough spectral resolution to identify individual types of nuclei within a sample. Traditionally this is achieved through a homogenous, high B_0 field strength to lengthen the T_2 of the sample, however Halbach magnets have been constructed which can provide NMR spectra from liquids in conventional 5mm sample tubes (Danieli et al., 2010).

1.4 Pulsed NMR

1.4.1. Pulsed NMR

An NMR sample may contain many different magnetization components, each with its own Larmor frequency. In pulsed NMR spectroscopy, signal is detected after these magnetization vectors are rotated into the x,y plane. Once a magnetization vector is in the x,y plane it rotates about the direction of the B_o field, the z axis. As transverse magnetization rotates about the z axis, it will induce a current in a coil of wire that is located perpendicular to the z axis. Plotting current as a function of time gives a sine wave. This wave decays with time constant T_2* due to dephasing of the spin packets. This signal is known as free induction decay (FID).

1.4.2. Pulse Sequences

There is a near infinite number of pulse sequences that can designed to collect a time domain signal in NMR. To be concise, only the sequences that are used in the methodology will be discussed. These sequences are the 90-FID, inversion recovery and Carr-Purcell-Meiboom-Gill (CPMG). The 90-FID sequence involves tilting the net magnetisation from the z axis into the x,y plane (Lowe, 1959; Lowe and Norberg, 1957). The net magnetisation will precess about the z axis and begins to decay with time.

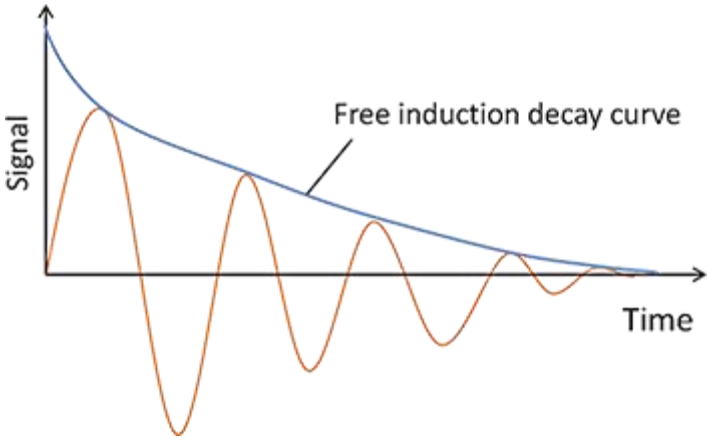

Figure 7: A 90° RF pulse is applied to a system using a transmit coil. A radio signal is read by a receive coil which eventually decays at a rate proportional to the T_2^* relaxation time. (Clarke, 2019)

Often, this sequence is repeated, and the results of successive pulses are averaged to improve signal to noise (SNR) ratios. The amplitude of the signal after being Fourier transformed will have a dependency on T_1 and the time between each repeat, known as the repetition time (T_R). If the T_R of the experiment is not set to the optimal time, which is dependent on the T_1 value of the nucleus, then the system will not have enough time to return to equilibrium resulting in successive pulses tilting the magnetisation beyond 90°.

The SNR is demonstrated by equation 10 where the total time duration of the NMR experiment is given by $NT_R = \tau$:

Equation 10:

$$\mathbf{SNR} = \mathbf{M_0}\sqrt{\frac{\boldsymbol{\tau}}{\mathbf{T_R}}}\left(\mathbf{1} - \mathbf{e}^{\frac{-\mathbf{T_R}}{\mathbf{T_1}}}\right)$$

When this function is plot graphically, it exhibits a maximum around T_R=1.2T_1. This means that a well-designed experiment should take note of the longest value T_1 that the system under investigation possesses. The operator should then look to set the T_R of the experiment to this optimum value of 1.2T_1 to obtain the highest possible SNR for a given experimental time period. The signal amplitude can be represented using a signal equation where the signal (S) is dependent on the time between repetitions (T_R), the T_1 relaxation time, a proportionality constant (k) and the density of spins in the sample (ρ).

Equation 11:

$$\mathbf{S} = \mathbf{k\rho}\left(\mathbf{1} - \mathbf{e}^{-\frac{\mathbf{TR}}{\mathbf{T_1}}}\right)$$

Another commonly used pulse sequence is known as the spin-echo pulse and is often performed using a Carr-Purcell-Meiboom-Gill (CPMG) sequence, named for the scientists involved in its design and optimisation (Carr and Purcell, 1954; Meiboom and Gill, 1958). Like with the FID sequence before, a 90° pulse is used to tilt the net magnetisation vector from the z axis into the x,y plane where it will begin to precess and dephase. However, after a set point in time another pulse is applied although this time by transmitting a 180° pulse. This causes the magnetisation to refocus, eventually coming back into phase almost as it was after the application of the starting 90° pulse. The signal generated from the rephased magnetisation is known as an echo.

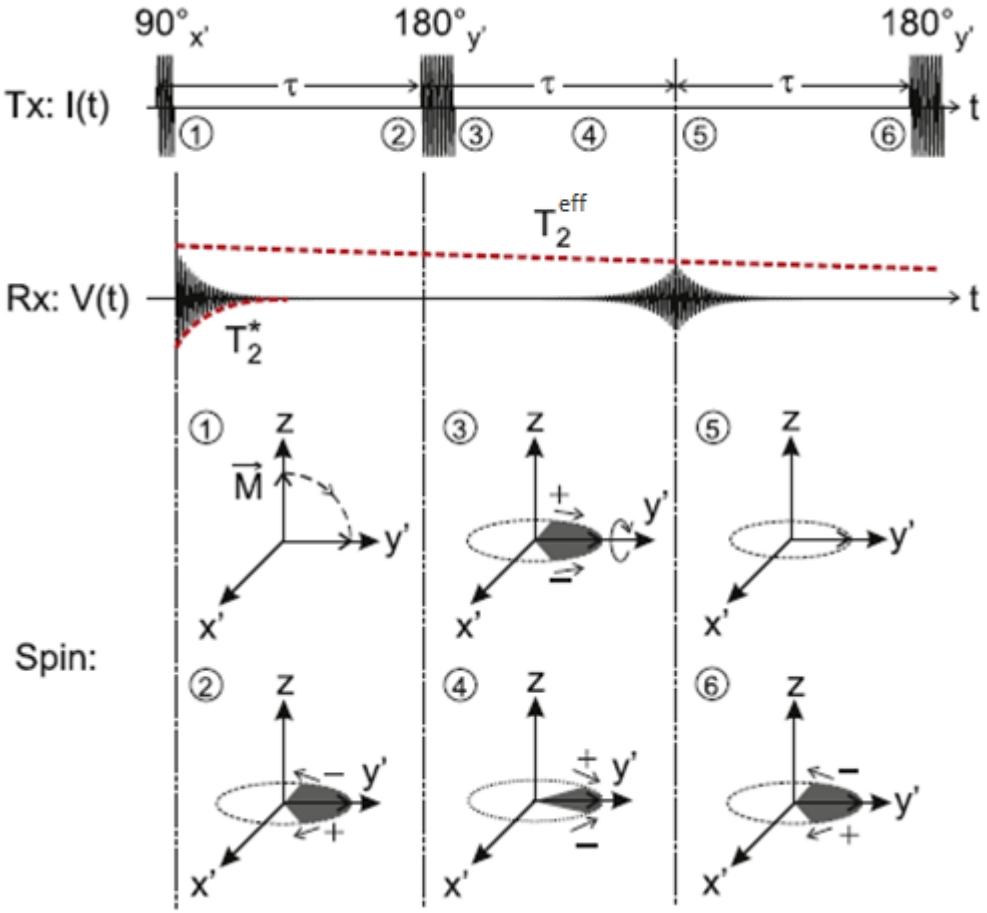

Figure 8: The Carr-Purcell-Meiboom-Gill (CPMG) pulse sequence. (1) The magnetisation is tilted from the z-axis onto the y-axis (90°) using an external RF pulse. (2) After this pulse is applied the spins begin to dephase, rotating about the z axis and becoming less coherent resulting in a loss of signal. (3) A 180° refocussing pulse is applied and all spins begin to precess at the same speed back towards the point they were at the end of the initial 90° pulse. (5) Eventually, all of the spins reconvene back to a single point and become coherent again resulting in an NMR signal being produced once more due to summation of all the magnetisation vectors. (6) The spins begin to dephase once more to be later refocussed by another 180° pulse. (Sun et al., 2013)

The output signal for a repeated spin echo sequence can be defined as a function of the repetition time (T_R), the time (T_E) between each 180° pulse and relaxation constants (T_1 and T_2) to provide the following equation:

Equation 12:

$$S = k\rho(1 - e^{-\frac{T_R}{T_1}})e^{-\frac{T_E}{T_2}}$$

The inversion recovery (Bydder and Young, 1985) sequence starts by utilising a 180° pulse to tilt the net magnetisation along the z axis effectively inverting it from its original orientation. The magnetisation undergoes spin lattice relaxation to return to its equilibrium position along the z axis, but before this equilibrium is met, a 90° pulse is applied to orient the net magnetisation into the x,y plane. Once the magnetisation is in the x,y plane it rotates about the z axis and dephases just like in the previous examples of pulse sequences.

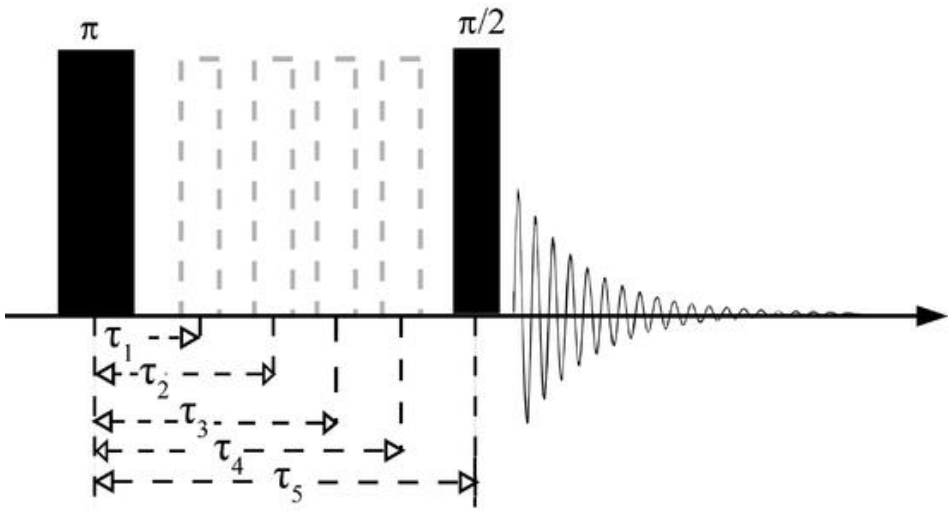

Figure 9: An inversion recovery sequence. A 180° RF pulse is applied to the system to invert the net magnetisation along the z axis. After a pre-set amount of time (Inversion time), a second 90° pulse is applied, and the resulting signal is collected. This sequence can be followed by a series of 180° refocussing pulses to collect an echo train. (Libretexts, 2019)

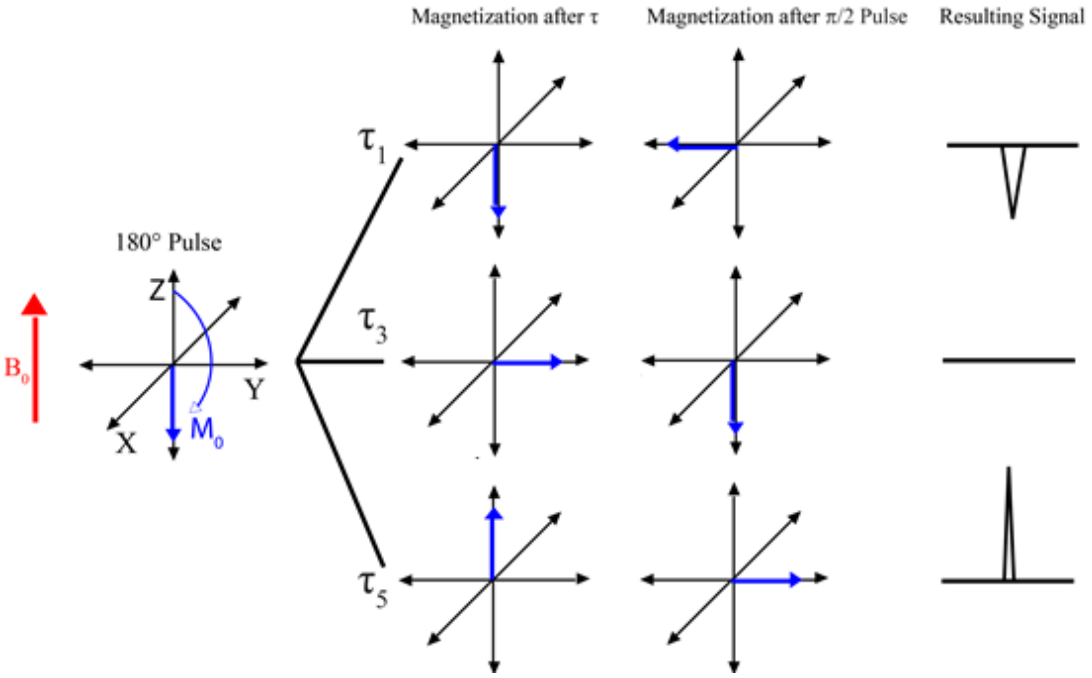

Figure 10: The effect of inversion time. τ_1 demonstrates a 90° pulse directly following the 180° inversion pulse. The result is the net magnetisation vector rotated fully into the x,y plane leading to a large negative signal. τ_3 demonstrates a 90° pulse after such a time as the net magnetisation vector is entirely in the x,y plane. After applying this 90° pulse, the magnetisation vector is rotated into the z axis resulting in zero signal. Finally, τ_5 demonstrates a 90° pulse after the system has been allowed to return to equilibrium. This pulse takes the net magnetisation vector from the z axis into the x,y plane resulting in a strong positive signal. (Libretexts, 2019)

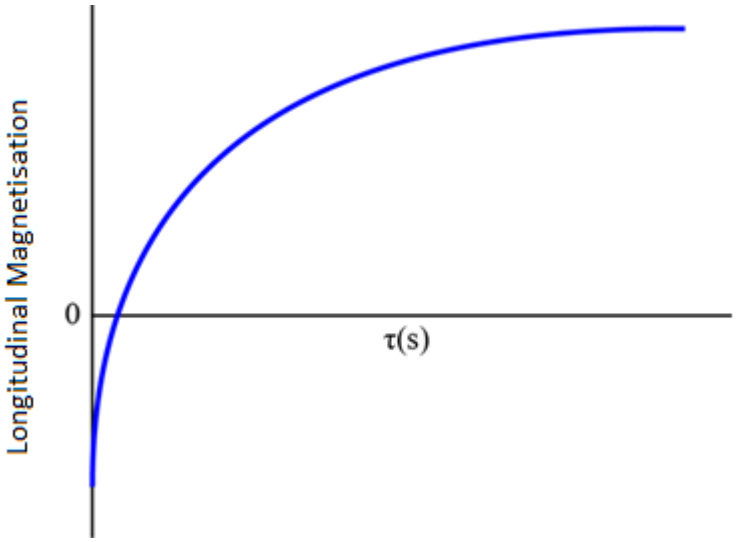

Figure 11: An inversion recovery curve built from recording the longitudinal magnetisation as a function of inversion time. (Libretexts, 2019)

1.4.3. Spectrometer Electronics

The probe is the part of an NMR spectrometer that does much of the work, in terms of exciting the nuclear spins, and detecting the NMR signal. The probe goes into the centre of the magnetic field, and the sample is inserted into the probe to perform the NMR experiment.

In the earliest NMR spectrometers, the probe consisted of a pair of orthogonal coils, where one coil was coupled to the RF transmitter and used to generate a homogeneous RF electromagnetic field over the sample area of interest. By applying a continuous stream of RF energy, or pulses of coherent RF radiation it is possible to induce transverse magnetization in the sample. The precession of this transverse magnetization would cause induction in a second coil known as the receiver coil which was installed to be orthogonal to the transmission coil. However, nowadays, most NMR spectrometers use a single coil for both transmission and receiving due to advanced electronics being able to switch quickly between transmit/receive modes. This is necessary to prevent the high energy input through the transmit system overloading the sensitive preamplifier in the receive system. The MR transceiver contains two major subsystems: The transmitter and the receiver subsystems.

Contained within a transmitter subsystem are the RF synthesizers and amplifiers. This subsystem is responsible for generating pulse sequences containing RF pulses of a specific frequency, amplitude, phase, shape and duration at desired time intervals. Multiple RF synthesizers are required because many MR experiments require simultaneous application of RF pulses of different frequencies. Older MR systems utilised waveform generators for RF synthesis with subsequent phase modulation but more recent systems rely on DDS (direct digital synthesis).

Housed within the receiver subsystem are several components, namely the Preamplifier, Amplifier, Mixer and the Analog-to-Digital converter (ADC). The relatively minuscule returned signal is sent through sensitive amplifiers before being sent to the ADC to digitise the signal for processing.

There is also an RF switch within the subsystem which is responsible for coupling either the Transmitter or the Receiver subsystem to the probe. This ensures that

the sensitive receiver subsystem is not overloaded with the high-powered RF signal generated by the transmitter system.

1.5 Continuous Wave NMR (CW-NMR)

1.5.1. CW-NMR

The first experiments involving NMR were performed using the continuous wave methodology before shortly being replaced with pulsed, Fourier transform instrumentation (Bloch et al., 1946; Bloembergen et al., 1948; Robinson, 1951). CW-NMR instrumentation consists of many of the same units as previously discussed, such as magnets to split the nuclear spin energy states, a RF coil to apply the matched B_1 frequency and some form of detector to process the NMR signals such as an oscilloscope. The major difference that CW-NMR holds over pulsed is that a wave generator is included to sweep either the magnetic or RF field through the resonance frequencies of the sample. These two methods are known as the field-sweep and frequency-sweep method.

In the case of the frequency-sweep method the magnetic field is fixed, and the RF frequency is varied over the sample. In the field-sweep method, the B_1 frequency is held constant whilst the B_0 magnetic field is varied. This can be achieved through applying a slowly increasing direct current through sweep coils and electronically speaking, is much simpler. The field is varied over across the precessional frequency of the nuclei in the sample.

Several different sources demonstrate how to calculate relaxation values of a sample from a CW-NMR spectrum using electronics such as Marginal (Makarov and Ryzhov, 2010), Robinson (Wilson and Vallabhan, 1989) and Van Der Pol oscillators (Robinson, 1987) or analysing the ‘wiggles’, known as transient effects (Bloembergen et al., 1948; Smith, 1953).

1.5.2 Bridge Circuits

Bridge circuits are a particularly effective method at detecting RF absorption. A bridge circuit design incorporates a pair of “arms”, shown in figure 49, which have similar impedance values in the absence of a sample. Once a sample is introduced to the system, and satisfies resonance conditions, the relative impedance changes

which provide a measurable voltage at the output of the bridge. If the system is off resonance, only the noise is amplified instead of the large output signal which allows more delicate electronics to be used. Bridge circuits are particularly popular in magnetometers - a device in which the resonance of a known sample can be used to determine the strength of the magnetic field in which the sample resides. Balancing the two arms of this bridge circuit is incredibly important. They must be balanced in terms of impedance, when off resonance, otherwise the output will be RF leakage which may be sufficient to overload sensitive detectors.

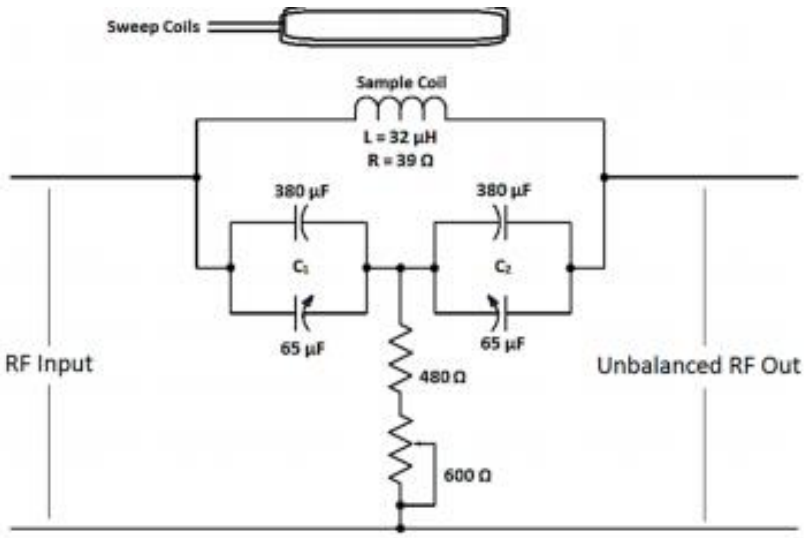

Figure 12: Example of a bridge circuit used in early magnetometers. The two arms are located at C_1 and C_2. (Newton et al. 2017)

In most cases, bridge balancing is a lengthy and complicated task, often requiring a high degree of proficiency and patience on behalf of the experimentalist. A possible solution to this was suggested in 1957, where voltage-controlled capacitors were used, allowing automatic bridge balancing (Collins, 1957). A small oscillating voltage with high frequency is used to check for balance, which is then automatically corrected with minimal deterioration of the NMR signal. Despite this rather elegant solution to the issue of bridge balancing, this technique has not been widely adopted.

Unfortunately, the signal output from a bridge circuit is particularly small and often indistinguishable from other sources of noise. A lock-in amplifier and rectifier is often used to combat this limitation.

The lock-in amplifier is a common instrument used in solving signal-to-noise problems in research laboratories. A signal of interest can be detected even when it is smaller than the noise signal accompanying it (signal-to-noise ratios of less than 1). An example of this is when lock-in amplifiers are used to detect and measure very small AC signals, in the region of nanovolts, where noise is always a concern. Lock-in amplifiers utilise a technique known as phase sensitive detection to single out the component of the signal at a specific frequency and phase. Once this task has been performed, noise signals at other frequencies or random phases are rejected through electronic or software filtering. In works such as Bloembergen and others where bridges are utilised, the modulation coil voltage is used as the lock-in reference, although this can also be achieved by applying an additional audio frequency to the sweep, which offers further sensitivity to the reference.

Rectifiers are electronic devices which convert alternating current to direct current. Direct current flows in only one direction as opposed to alternating current, which periodically reverses direction.

1.5.3 Rise of the Marginal Oscillator

A marginal oscillator is a tank circuit with nonlinear output feedback applied to maximize the change in amplitude with respect to the circuit's internal resistance. A tank circuit is a simple electrical circuit composed of an inductor and a capacitor connected together. This circuit acts as an electrical resonator, storing energy oscillating at the circuit's resonant frequency. Although it is used in many applications, the marginal oscillator is most commonly used in applications of CW-NMR. The primary component of this system is a tank circuit composed of a sample coil and a capacitor. This is then driven with energy from a valve or transistor circuit which is just sufficient to sustain oscillation. This device is then swept through resonance where an increase of loading can occur which results in a reduction of

amplitude in the energy of the tank circuit. This reduction can be observed by incorporating oscilloscope-based detection methods.

When regarding bridge circuits, a change in the resonance condition must be accounted for by retuning the RF source. This differs from the marginal oscillator where it is itself part of the resonant circuit and therefore tracks the resonance. This provides an advantage as the detected signal is purely absorption, thanks to the inherent feedback. Dispersive components of susceptibility produce slight frequency modulation of the oscillator, which is not rectified in the detection stage. Pound and Knight are credited with their classic paper describing the construction of a valve-based marginal oscillator in the early 50's (Pound and Knight, 1950). Valves, or vacuum tubes, became a key component of electronic circuits for the first half of the twentieth century. They were crucial to the development of radio, television, radar and early digital computers. It was the invention of the thermionic vacuum tube that made these technologies widespread and practical, and created the discipline of electronics.

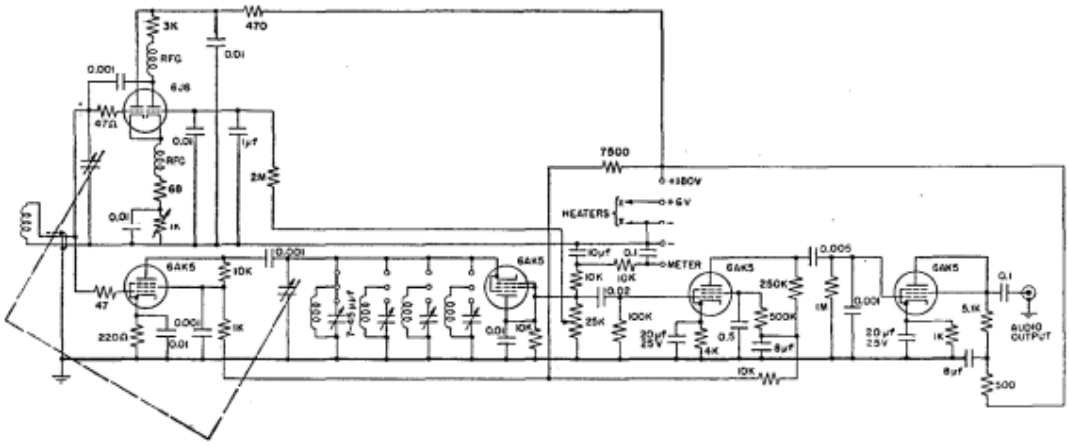

Figure 13: Pound and Knight's classic valve-based marginal oscillator circuit. There are five valves located in this particular circuit identifiable by circles with dashed lines through them. Valves were used in numerous radio electronics until the advent of semiconductor devices.
(Pound and Knight, 1950)

In the following decade the technology and availability of transistorised electronics developed considerably, leading to a more sophisticated device, based around a

2N393 PNP germanium transistor, to be developed by Donnally and Saunders (Donnally and Sanders, 1960). Despite having a lower SNR to Pound and Knight's original valve-based oscillator, this new design consumed significantly less power and suffered less from other issues such as mechanical movement contributing to noise.

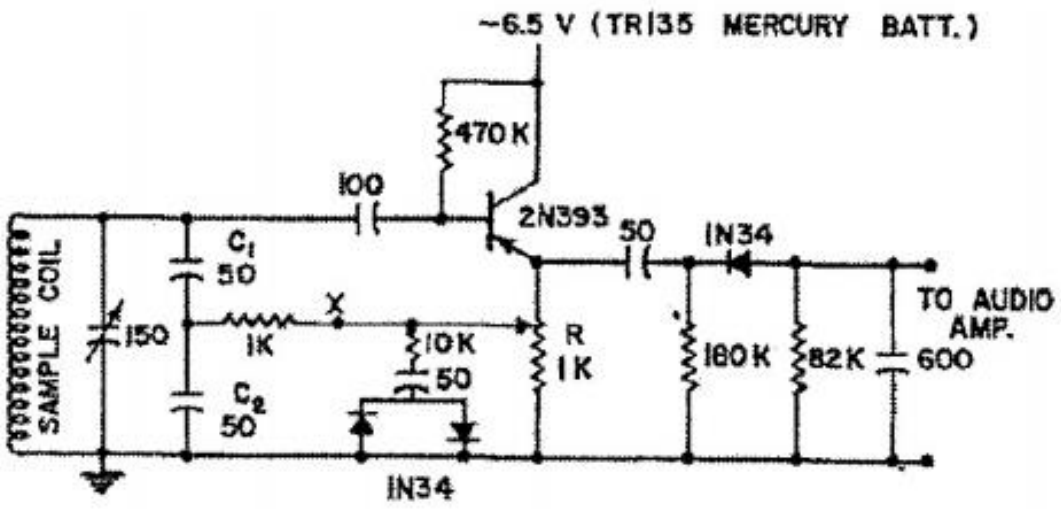

Figure 14: Donnally and Saunder's germanium transistor-based marginal oscillator circuit. In this specific circuit there are no valves as seen in the previous figure. Instead of using valves, a germanium diode (2N393) is used instead. The invention of semiconductor devices made it possible to produce solid-state devices, which are smaller, more efficient, reliable, durable, safer, and more economical than thermionic tubes. (Donnally and Sanders, 1960)

The Donnally and Saunders marginal oscillator circuit is based on a tank circuit which feeds into the base of a Germanium transistor. The output signal from the transistor is then passed through a rectifying diode and narrow bandwidth audio filter with a cut off at twice the sweep rate of the magnetic field modulation coils. The paper also provides an audio amplifier circuit which is of standard design. The work presented in the publication is based upon swept magnetic fields, but the authors state that C_1 and C_2 can be substituted with voltage variable capacitors to allow for a variable oscillator sweep.

These early circuits operated successfully due to a number of properties of transistors that are less desirable for many modern designs, such as those that limit maximum frequency of operation in amplifier circuits.

This issue was later addressed by Frank Willingham in a thesis published in 1988 through replacing the Germanium transistor of the Donnally/Sanders oscillator circuit with a pair of Field Effect Transistors (FETs) (Willingham, 1988).
An FET is an electronic device which uses an electric field to control the flow of current. Composed of three terminals: source, gate, and drain, FETs control the flow of current by the application of a voltage to the gate, which in turn alters the conductivity between the drain and source. FETs are also known as unipolar transistors as they involve single-carrier-type operation meaning that they use electrons or holes as charge carriers in their operation, but not both.
The use of an Operational Amplifier based audio amplifier is also presented, as well as lock-in detection, where one sweep coil is used for sweeping the resonance of the sample, whilst the second is responsible for applying a small, higher frequency oscillation, which is fed into a phase sensitive detector.

1.5.4. Non-Marginal Oscillators

As Donnally and Saunders were making alterations to the Pound/Knight value-based system, Robinson had begun work on an alternative type of oscillator which would later be known as a Robinson Oscillator (Robinson, 1959). The major difference between a Robinson Oscillator and Marginal Oscillator is located within the feedback loop. In a Robinson oscillator, the signal is fed back through a limiter instead of a resistor which returns a square wave current back to the tank circuit. The construction of the tank circuit allows it to act as a filter, selecting the fundamental of the square wave. As with the Pound/Knight oscillator, the original design utilised a valve-based system, but transistorised versions were eventually developed (Robinson, 1965). The original paper published by Robinson also spoke of the disadvantages of marginal oscillators claiming low sensitivity, difficulty of adjustment when working at levels below 20mV and an incompatibility with circuits with a low inductance to capacitance ratio.
In a later publication, Faulkner and Holman hypothesised that many transistorized Robinson oscillators that had previously been published were in fact not true to the functionality of the original and that even the version published by Robinson

himself in 1965 did not meet the original feedback criteria. Faulkner and Holman discussed these findings with Robinson leading to a transistor version of a true Robinson oscillator and demonstrating the circuit's functionality as a magnetometer with a rubber sample material up to a frequency of 30 MHz (Faulkner and Holman, 1967).

In 1990, a metal oxide semiconductor field effect transistor (MOSFET) version of a true Robinson oscillator was developed by Wilson and Vallabhan (Wilson and Vallabhan, 1990). A MOSFET is a type of FET, discussed earlier, except that the gate is insulated from the channel by a layer of metal oxide providing a higher input impedance.

1.5.5. T_1 Relaxation Measurements using CW-NMR

Performing T_1 measurements using pulsed NMR can be time consuming, however pulsed NMR is still prevalent over using CW-NMR. As the forerunner to pulsed experiments, CW-NMR has been investigated over the years to perform T_1 relaxation measurements using a variety of systems and techniques.

One of the earliest experiments in which T_1 was measured was published in 1949 by Drain (Drain, 1949) expanding upon the original work performed by Bloch (Bloch et al., 1946). The experiment is performed utilising a two coil system. The transmit coil is used to excite the sample, while a receive coil detects the resultant absorption and the time difference in which the absorption is measured will dictate the polarity of the signal. As the magnetic field is swept through resonance, the magnetisation tends to return to equilibrium at an exponential rate. When the sweep rate is in the same order of time as T_1, this change occurs whilst the system is out of resonance. When the sweep voltage is balanced at resonance, the peak generated from sweeping low to high will have similar amplitude to the one sweeping back. Finally, if the sweep voltage is offset above or below resonance, the two peaks will have different amplitudes. Using these measured peaks allows for a plot of peak amplitude against the difference between the time spent above and below resonance resulting in a trace providing a measurement for T_1. This is verified with measurements of the T_1 value for glycerine at varying viscosities.

An additional method, which is similar to a pulsed NMR inversion recovery experiment, is presented by Firth (Firth, 1982). In this experiment a commercial Newport magnetometer based on a Robinson oscillator is used. To start with, the sample is saturated either with significant RF power or low modulation amplitude. The saturation is then suddenly reduced by either by reducing the RF power or increasing the modulation amplitude. The signal recovers with a time constant ZT_1, where $Z = (1 + 2PT_1) – 1$, where P is the probability of inducing a nuclear transition for the nuclei of interest. This recovery was captured through an oscilloscope to demonstrate how the system returns to equilibrium from saturation.

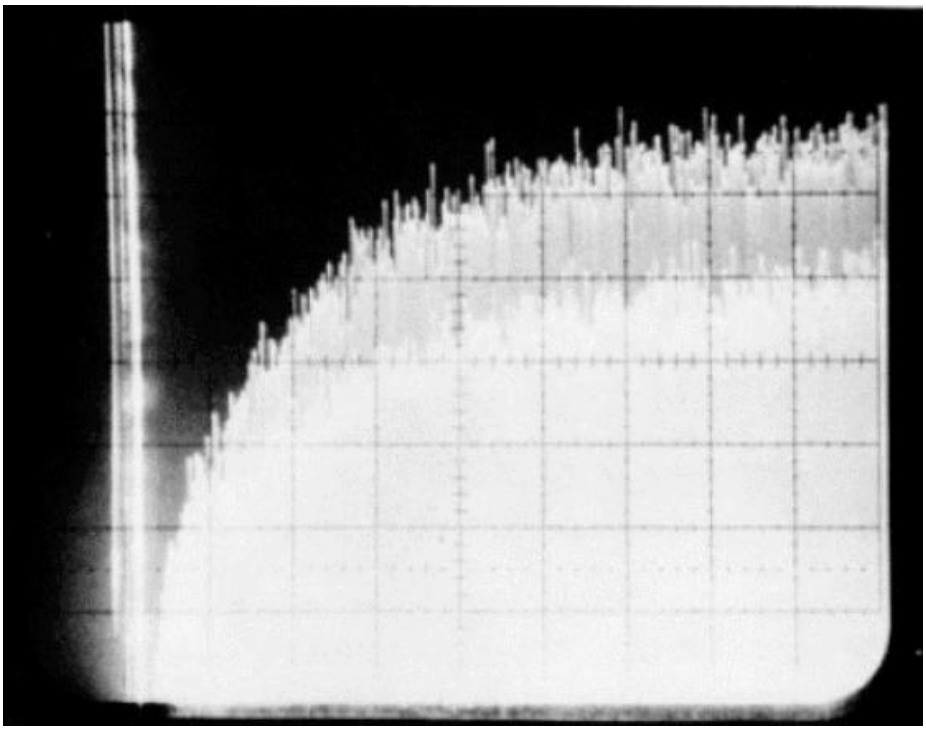

Figure 15: An oscilloscope trace for the recovery of water protons presented by Firth. (Firth, 1982)

Another method was presented by Donnally and Enrique in 1963 (Donnally and Bernal G, 1963). This experiment utilises the different flow rates of a liquid sample down a pipe, varying the amount of time the atomic nuclei spend within the magnetic field. The sample is then passed through a coil which is connected to a marginal oscillator such as the one described earlier. While the atomic nuclei inside the sample are outside the magnetic field, the nuclear spins are randomly

distributed with the field, eventually becoming polarised at a rate exponentially related with T_1 as they enter. When the flow rate is rapid, the sample does not have enough time to become polarized leading to a small signal. In contrast, if the flow rate is low, then the signal increases up to the time at which the sample is fully polarized. After this time, any further decrease in the flow rate does not lead to an increase the signal amplitude. The signal amplitude can be plotted against the time from the edge to the centre of the magnet, an exponential with time constant T_1 is traced which can be measured down to 200 milliseconds.

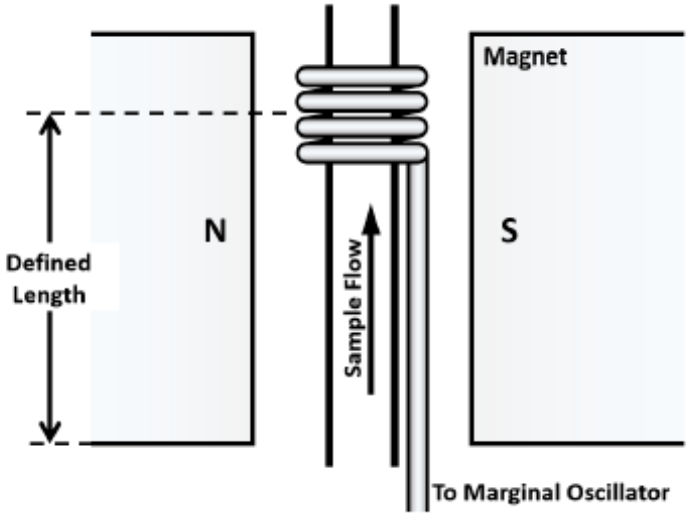

Figure 16: A flow-based experimental setup proposed by Donnally and Enrique to measure the T_1 relaxation time of a sample. (Donnally and Bernal G, 1963)

A final alternative method was presented by Look and Locker (Look and Locker, 1968, 1970) in which a gated sweep waveform was used. This method details how a sample which is left polarised with the magnetic field but held off resonance before the start of a measurement, can be used to measure T_1. The sample is then swept through resonance cycles by the sweep coils and an absorption trace is collected for each sweep. The amplitude of each trace varies exponentially with time constant T_1, until it is fully saturated as shown in the figure below. Of all of the methods, this one shows great promise in its ability to be automated and will be the ideal focus for a modernised, automated experimental setup.

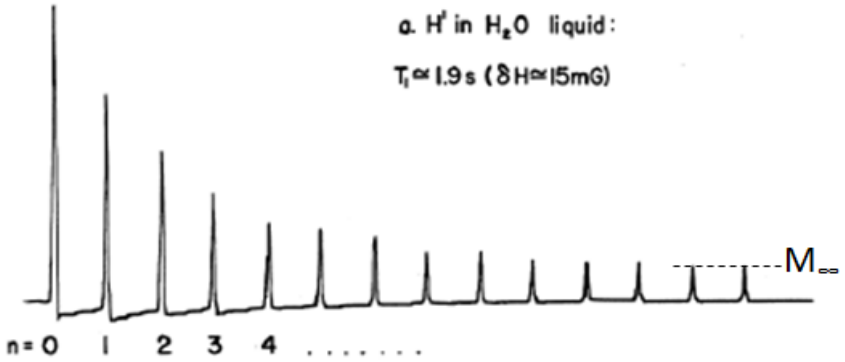

Figure 17: An example NMR trace of water from Look and Locker's experimental paper. After each sweep through resonance, an absorption peak signal is collected and plotted against the number of sweep cycles. An exponential reduction in signal amplitude is observed until a steady state is reached (referred to as M_∞). (Look and Locker, 1968)

1.5.6. T_2 Relaxation Measurements using CW-NMR

When considering a pulsed NMR experiment, the direction of some of the nuclei of interest are aligned with an externally applied magnetic field and begin to precess. This perturbation generates a small, localised magnetic field that perturbs their neighbours, leading to slightly different precessional frequencies. During this precession, the number of nuclei rotating through the original point in each revolution decreases exponentially allowing the time constant T_2^* to be measured. When considering a continuous wave system, energy is supplied off resonance, which has little or no effect on the nuclei of interest. As resonance is approached the nuclei begin to feel an effect. When sweeping past resonance, the signal may continue to exist thanks to storage of energy. If a sample has a significantly long T_2^*, this effect will be more noticeable than for those with short T_2^*. This is advantageous as if the sweep of field or frequency is slow enough to approximate the steady state absorption, T_2^* can be measured from the line width of an absorption curve. By measuring the half-height width of the absorption peak or the interval between the maximum and minimum slope, T_2^* can be calculated using the equation below, where $\Delta\nu_{1/2}$ is the linewidth of the absorption peak:

Equation 13:

$$\Delta v_{1/2} = (\pi T_2^*) - 1$$

An alternative method for determining T_2^* is presented by Bloembergen et al. (Bloembergen et al., 1948). A beat signal is created by the increasing difference between the frequency of the nuclei that are still precessing and the RF excitation frequency. The result of this is a signal which decreases exponentially with T_2^* and which becomes increasingly higher in frequency as a function of the sweep rate (Blamey and Smith, 1950). This signal was given the term "wiggles"

However, there is a limitation in which such a signal will not be seen. The signal is only observed when the sweep rate is short compared with $1/\gamma\Delta H_0$, where ΔH_0 is the magnitude of field inhomogeneity. Jacobsohn and Wangsness provide an overview on this limitation, suggesting that the sweep must be at least ten times faster than the shortest T_2^* value of interest to achieve such a signal (Jacobsohn and Wangsness, 1948). This experiment is often referred to as the fast passage experiment. As the inhomogeneity of the field, $H_{0,}$ increases, the distribution of precessional frequencies causes additional beat frequencies making it progressively more difficult to meet the criteria for fast passage and it ultimately becomes impossible to measure T_2* using this method.

There are not many other instances of CW-NMR being used for T_2* measurements. Despite this, it would be pertinent to believe that a technique which would allow T_2^* to be measured for a fraction of the cost of a commercial pulsed system would be achievable. The stringent requirement for high field is most likely the reason for this and combining this requirement with the difficulty of determining the value of T_2^* which is straightforward with pulsed NMR, has resigned CW-NMR primarily to literature.

1.6. Magnetic Nanoparticles in NMR

1.6.1. Fabrication and Functionalisation

Nanoparticles are tiny particles, usually in the size range of 1-100nm, and composed of organic or inorganic materials. The main feature of nanoparticles is that their

magnetic and electronic characteristics behave differently to those of bulk materials of the same composition due to size effects (Huang and Juang, 2011). During the last few years, a large portion of the published articles about magnetic nanoparticles (MNP) have described efficient routes to attain shape-controlled, highly stable, and narrow size distribution MNPs (Lu et al., 2007; Saha et al., 2012; Sandhu et al., 2010; Shipway et al., 2000). Spray-drying is one technique that is used to fabricate nanoparticles from a liquid sample (De Frates et al., 2018). The liquid sample is sprayed into a chamber, where heated nitrogen and carbon dioxide gas flows in the direction of the spray, and electrodes are used to collect the nanoparticles becoming electrostatically charged. This is a one-step process that is quick and cost effective but limited to small scale production. Milling is another technique which utilises mechanical energy to break larger particles into finer nanoparticles. This is another cost-effective technique that can be utilised for large scale production, but as heat is released during the milling process additional cooling must be supplied to the chamber. There is also little control of nanoparticle shape, although size can be easily controlled by modifying the speed of rotation in the cylindrical chamber (De Frates et al., 2018).

A wide variety of ligands have been incorporated onto nanoparticle surfaces, allowing them to be used in sensing of biomolecules and cells, diagnosis of diseases, and intracellular delivery (Bridot et al., 2007; Brigger et al., 2012; Christofer Adding et al., 2001; Mornet et al., 2004). In protein-ligand binding, the ligand is a molecule that binds to a target site on a protein. The rate of this binding is referred to as the affinity.

The primary interest with regards to this thesis is to their uses in NMR, where they are used as contrast agents. Commonly, paramagnetic complexes such as gadolinium diethylenetriaminepentaacetic acid (Gd-DTPA) are used as T_1 contrast agents and magnetic nanoparticles are used as T_2 contrast agents (Bridot et al., 2007). When a magnetic field is applied, the nanoparticles become magnetised and generate their own induced magnetic fields, which perturbs the relaxation of protons around them leading to a shortening of their relaxation times.

1.6.2. Uses as Contrast Agents

T_1-based contrast agents are often composed of paramagnetic metal ion complexes that shorten the longitudinal relaxation time of surrounding water protons. These are also referred to as "positive" agents because they typically produce image brightening in T_1-weighted imaging sequences (Caravan et al., 1999). This is due to T_1-weighted images having short echo and repetition times.

Nuclei with a short T_1 quickly realign their longitudinal magnetisation with B_0, Appearing bright on a T_1-weighted image. Conversely a molecule with a high T_1 has much slower longitudinal magnetisation realignment and therefore appears dark. The gadolinium ion is a lanthanide series element and is the metal of choice for nearly all T_1-based agents because of its seven unpaired electrons in its 4f orbitals, a high magnetic moment, and an unusually long electronic spin relaxation time (Lauffer, 1987). Free Gadolinium ions are toxic in most biological systems as the ion has an ionic radius close to that of ^{21}Ca but also possesses a higher positive charge. Due to this property, proteins cannot distinguish between a ^{31}Gd versus ^{21}Ca ion, meaning any free ^{31}Gd that is introduced into a biological system quickly binds to ^{21}Ca ion channels and other ^{21}Ca requiring proteins. The mechanisms involved for ^{31}Gd toxicity, however, are still not very well understood (Reilly, 2008; Wiginton et al., 2008; Yantasee et al., 2010). Potential toxicity can be suppressed by binding ^{31}Gd to an organic ligand to form a complex. The ligand influences the chemistry of ^{31}Gd by reducing toxicity, altering the tissue distribution of the agent, and influencing the efficiency of ^{31}Gd in shortening T_1 and T_2 (De Leõn-Rodríguez et al., 2015).

T_2 contrast agents decrease the water signal intensity by shortening the transverse relaxation times. The magnetic susceptibility induced by these agents create local magnetic field gradients that dephase the transverse magnetization and this efficiency is characterised by its relaxivity, r_2. Currently, the majority of T_2 contrast agents are iron oxide-based superparamagnetic nanoparticles coated with dextran (a gum created through condensing glucose) and other similar polymers (Lu et al., 2007). Superparamagnetic materials behave similarly to paramagnetic materials in that an externally applied magnetic field can magnetise the particles, but the

magnetic susceptibility is much higher due to their smaller size. Surface coating is useful to improve biocompatibility, so they are suitable for clinical applications, as a large buildup of iron oxide in the body can lead to toxicity through oxidative stress (Hanini et al. 2011). Polymer coatings can be functionalised for a number of therapeutic applications such as blood purification (Herrmann et al., 2010; Bannas et al., 2010). The size of iron-oxide heavily influences how they are used. Two examples are SPIO (superparamagnetic iron oxide, 50–500 nm) and USPIO (ultrasmall superparamagnetic iron oxide, 4–50 nm) nanoparticles which both have widely differing T_2 relaxivities and tissue biodistribution (Ittrich et al., 2013). Such nanoparticles are attractive for detecting specific biological targets by MRI as particles of a large size can impede or alter tissue penetration and delivery.

It is also important to understand that all contrast agents shorten both T_1 and T_2 as it is the relative contribution to r_1 or r_2 that influence contrast agent behaviour. When considering iron agents specifically, several factors contribute such as the crystalline symmetry, the size of the core and the nature of the coating used for the core (Pouliquen et al., 1989; Wolf and Halavaara, 1996).

CHAPTER 2: MAGNETIC RESONANCE DISRUPTION (MARDI) FOR THE DETECTION OF SURFACE IMMOBILISED NANOPARTICLES.

2.1. Introduction and Aims

Traditionally, MR based systems fall broadly into the chemical fingerprinting by NMR or the large body scanners of MRI (Mansfield, 1977).

Most NMR equipment is large, owing to the necessary sizes of the magnets, and boast high costs regarding purchase and use though the requirement of high-power loads and cryogens. Both limitations can incur serious issues for institutions where space and funding can be difficult to dedicate to such equipment. The technology for producing high field static magnets has become more developed in recent years allowing greater control over the shape and magnetic field profile of permanent magnets. This has aided the availability of low field NMR equipment that is compact and affordable (Shafiee et al., 2013; Sillerud et al., 2006; Sun et al., 2013; Wignarajah et al., 2015).

Point of Care NMR systems are becoming more readily available in recent years, promising rapid diagnosis of many ailments including tumours (Haun et al., 2011) and even fungal infections (Bilir et al., 2015; Skewis et al., 2014).

This chapter of the thesis aims to develop a platform technology to detect the presence of surface-bound magnetic nanoparticles. The effects of a virus/antibody immunoassay can be simulated through the use of an avidin/biotin complex (Green, 1975; Livnah et al., 1993; Michael Green, 1990; Wilchek et al., 2006). Though developing this simulated method and platform technology it will open future work to allow an investigation into specific biological and chemical applications.

2.2. Current Literature

2.2.1. Assays and Chemical Immobilisation

A Microarray can almost be considered a “lab on a chip”. It is a two-dimensional array on a solid substrate (such as a glass slide or silicon thin-film cell) which can test large amounts of biological material through numerous detection methods. Microarrays allow the simultaneous monitoring of expression for many genes and proteins using fluorescent labelling and radioisotope markers (Alhogail et al., 2016; Kozitsina et al., 2016; Schena et al., 1995). Unfortunately, fluorescent systems have several disadvantages, such as false-positive and false-negative data in samples due

to cross-reactivity and issues with binding (De Smet et al., 2004). The sensitivity of fluorescent systems can also be reduced by quenching, which demands the use of additional resources to optimise and evaluate the data (Ramdas et al., 2001). These problems have been challenged using a detection system utilising MRI on a microarray inside an NMR imaging fluid which does not depend on fluorescent probes. In the procedure performed by Hall et al. (Hall et al., 2010), replacing fluorescent markers with immobilised magnetic nanoparticle such as super paramagnetic iron oxide (SPIO) creates a MRI readable DNA array system.
The addition of the SPIO enhances the T_2* relaxation times due to an increased efficiency regarding the dephasing of the system's protons.
A 2.35T Bruker® BIOSPEC MRI scanner with a rapid acquisition with relaxation enhancement (RARE) protocol (Hennig et al., 1986) was used to image the fluid immersed arrays. By exploiting the T_2* contrast, DNA hybridisation can be located in areas of negative contrast. The highest contrasts were discovered in fluids with a larger diffusion coefficient or using a longer echo time.

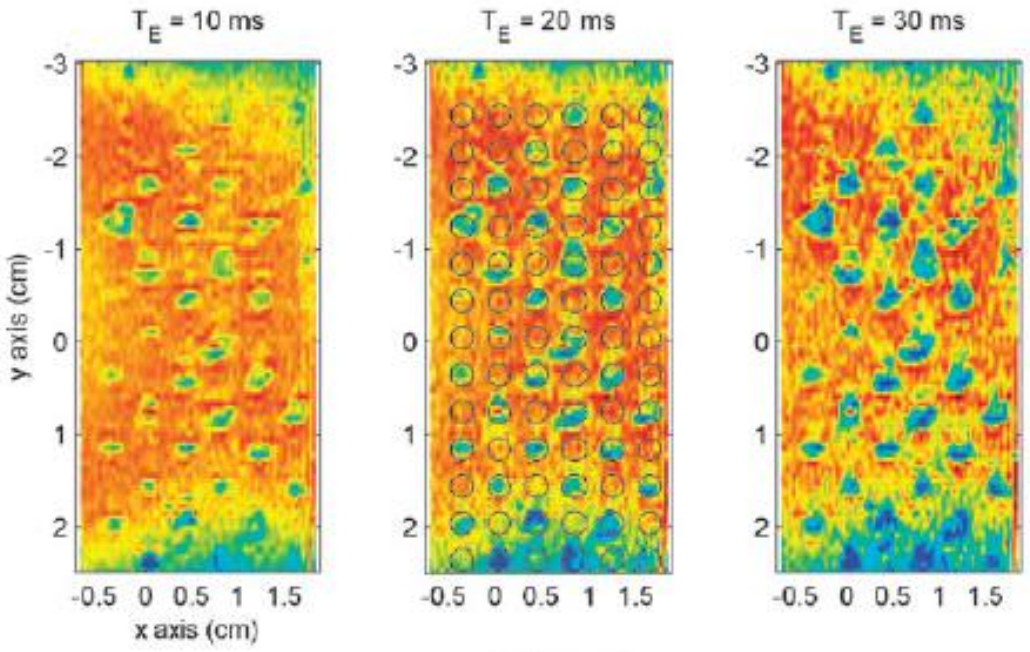

Figure 18: Colour coded MRI images of a water saturated system with increasing echo time. The readable array was designed so that control regions and SPIO-labelled regions were intermittently placed left-to-right along the area. Black circles have been used to highlight the boundaries of the SPION-labelled and control areas. As can be seen, every other circle in the array has a much lower (blue) relaxation time than the control regions (red/orange). The presence of paramagnetic material acts as a contrast agent enhancing the relaxation rate of nearby protons. (Hall et al., 2010)

As the previously discussed microarrays are used for the detection of DNA strands, the method will need to be modified for biotin-avidin interaction. The protein-ligand interaction has been of interest to researchers when developing nucleic acid sensors (Furlong, 1997), utilising this strong affinity to detect biotinylated strands of DNA. One experimental method demonstrates how biotin can be affixed directly to a polystyrene surface through evaporation and UV immersion (Stanley et al., 2006).

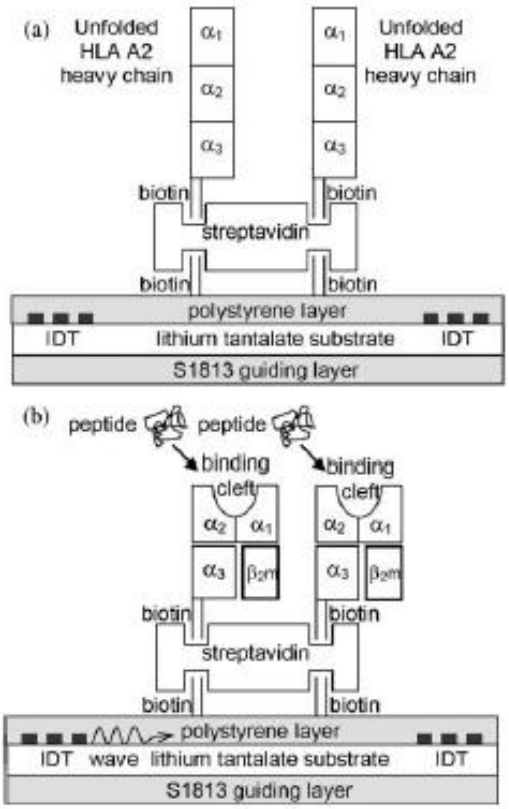

Figure 19: The binding schematic used for the acoustic plate mode biosensors. (Stanley et al., 2006)

Utilising the direct biotin immobilisation method mentioned previously, it should be possible to bind SPIO-labelled avidin/streptavidin to the polystyrene which should cause signal interference in an area around the nanoparticles, as demonstrated by Hall et al., which would then be detectable by a T_2^{eff} change in a surrounding fluid medium.

2.2.2. The Biotin/(Strept)Avidin Interaction and Uses in Biomedical Research

Streptavidin is a protein purified from the bacteria Streptomyces avidinii whereas a similar protein avidin is extracted from egg whites. These proteins exhibit the highest known affinity (K_a of roughly 10^{15} M^{-1}) in nature between a ligand, in this case biotin, and a protein (Green, 1975). This interaction has been widely exploited for its applications in diagnostic sciences (Lee et al., 2008; Sun et al., 2013). The structure of the avidin and streptavidin monomer are closely related, consisting of eight antiparallel protein strands which form a classical beta barrel structure (Livnah

et al., 1993). A beta barrel is a sheet composed of an array of proteins which twists into a closed toroidal structure until the last strand becomes hydrogen bonded with the first strand. Beta barrel structures are named for their resemblance to the barrels that normally contain liquids.

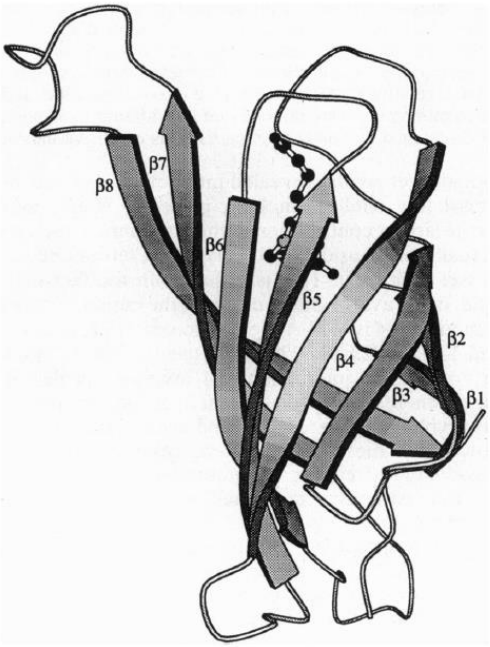

Figure 20: A ribbon diagram of avidin and biotin bonded. The biotin molecule is shown in a ball and stick model. (Kraulis, 1991)

Biotin (vitamin H or B_7) is composed of an ureido (tetrahydroimidizalone) ring fused with a tetrahydrothiophene ring (Du Vigneaud et al., 1941). Valeric acid is attached to a carbon atom in the thiophene ring.

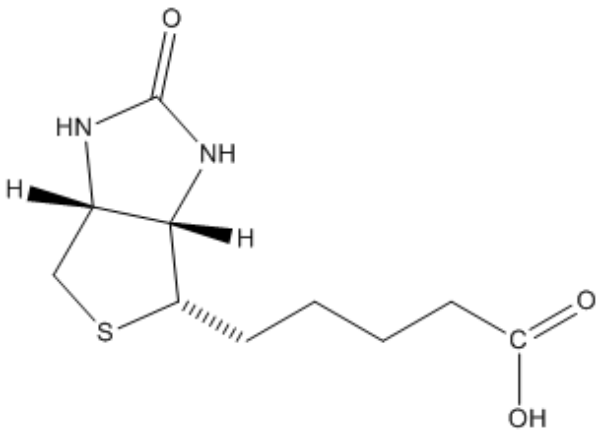

Figure 21: The structure of biotin. (Drawn using ChemBioDraw Ultra 14.0)

Avidin and streptavidin both contain a tyrosine-containing stretch, composed of eight amino acid residues, which forms a critical hydrogen bond with the oxygen group located in the ureido ring of the biotin (Livnah et al., 1993).

There are only two major differences with regards to the binding sites of avidin and streptavidin. Firstly, avidin possesses an extra aromatic group (an amino acid that contains an aromatic ring) containing five in comparison to streptavidin's four. The second difference is located in the hydrogen bonding network within the valeric acid of the biotin, where streptavidin only forms two hydrogen bonds compared to avidin's five. These two factors may explain why the binding of avidin to biotin is slightly higher than that of streptavidin to biotin ($6x10^{-16}$ M vs $4x10^{-14}$ M respectively)(Michael Green, 1990). This interaction has been used in order to investigate how NMR systems can be used as a biomolecular sensor (Sun et al., 2013). Using magnetic nanoparticles with attached biotin, T_2^{eff} was recorded for a solely nanoparticle solution and again for a nanoparticle solution with avidin proteins present. The value of T_2^{eff} was reduced when the biotin molecules were added to the avidin. The biotin particles remained mono dispersed, but clusters form with the addition of the avidin proteins reducing the homogeneity of the solution therefore reducing T_2^{eff}. The reduction of T_2^{eff} was only 8ms, a reduction of 16.7%. Such a small reduction would require sensitive equipment and repeated readings to detect.

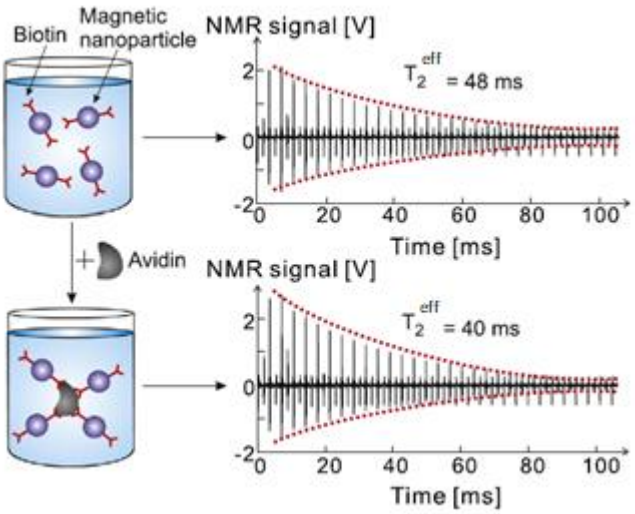

Figure 22: The recorded T_2^{eff} values of 2 solutions - One with biotin and another with biotin and avidin. (Sun et al., 2013)

On the other hand, miniaturised diagnostic magnetic resonance (DMR) systems have been developed consisting of four major components: a micro NMR chip consisting of microcoils, a micro-fluidic network for handling samples, an electronics system and a small permanent magnet (Lee et al., 2008).

Using this DMR system, the differences in T_2^{eff} measurements between the biotin and avidin-biotin complex were much greater. The smaller volume of liquid in the microfluidic system lowers the amount, and therefore cost, of reagents needed making it a suitable system for point of care devices. This system has also been reportedly used to successfully measure values of T_1.

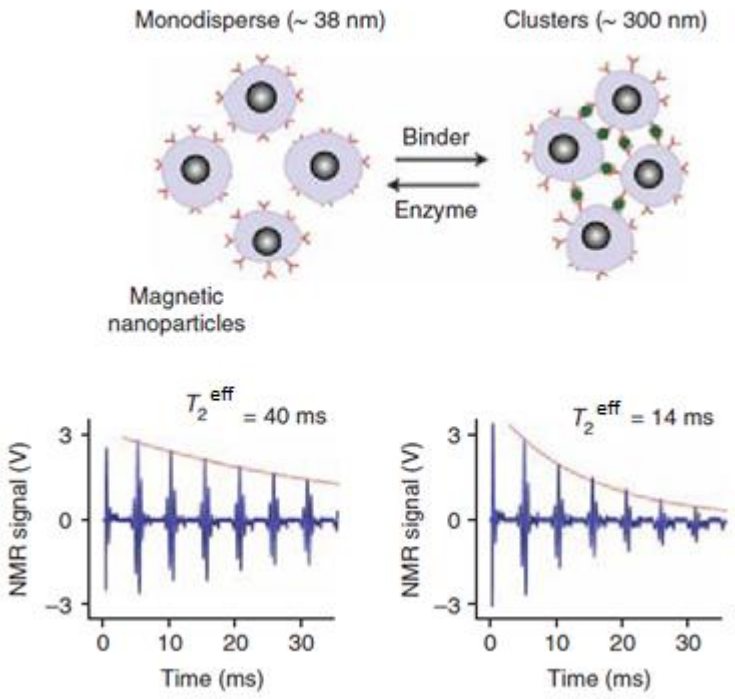

Figure 23: The T_2^{eff} values of biotin and biotin-avidin using the DMR system. (Lee et al., 2008)

2.2.3. Diagnostic Medicine Utilising Low Field T_2 Relaxometry

Using the various techniques discussed above, a number of developing businesses have begun work and trials on a range of diagnostic devices (Bilir et al., 2015; Cuker et al., 2016; Hong Nguyen et al., 2019; Muñoz et al., 2018; Skewis et al., 2014). Of note, is T2 Biosystems who have developed the T2 Magnetic Resonance (T2MR) platform which enables the detection and measurement of a variety of diagnostic targets. Two major advances of T2 Biosystems have been in the diagnosis of sepsis, a severe whole-body inflammatory response caused by bacteria or fungi, and haemostatic disorders such as haemorrhage and thrombosis.

Sepsis is often diagnosed through blood culture which can take up to 5 days for a positive result and 5-7 days for a negative result. False negatives are prolific in slow-growing or uncultivatable pathogens which causes additional limitations and misses diagnosis.

2.3. Halbach Development

To begin the task of collecting pulsed NMR data, a sensor must be constructed. An 8 magnet Halbach sensor was initially selected as it fulfils the criteria of being compact, homogeneous and cost-effective as 10x 0.5T NeFeB magnets could be purchased for under a hundred pounds. Radio-frequency pulse sequences were handled by commercial electronics during testing and fabrication to ensure the sensor was correctly assembled.

2.3.1. Initial Sensor Development

In order to begin detecting an NMR signal, a sensor was constructed. This sensor consists of a set of eight 0.5T neodymium magnets (First4Magnets, UK) which provides a static magnetic field (B_0) as well as a coil connected to a pair of variable capacitors which allows tuning and matching to the Larmor frequency that a sample will experience once it is placed within the static field.

Figure 24: An example display of a network analyser as a resonance circuit is tuned and matched. The closer the peak is to the Larmor frequency, the less off-resonance effects will contribute to signal interference. A deep peak corresponds to a high amount of transmitted power, reducing the amount of reflection from the probe resulting in higher efficiency. A narrow peak width corresponds to a narrow bandwidth ensuring transmission only occurs close to the desired frequency.

The magnets are arranged in a closed Halbach geometry in order to obtain the highest possible field strength and homogeneity of a permanent magnet system. This sensor arrangement is then connected to a commercial KEA^2 spectrometer

(Magritek, New Zealand) driven by its associated Prospa (Magritek, New Zealand) software program.

Once fully assembled, the field inside the centre of the bore was measured with a Gauss meter. Some small field variations were present in the bore, but the central field was measured to be 510±20mT corresponding to a proton resonant frequency of 21.7MHz.

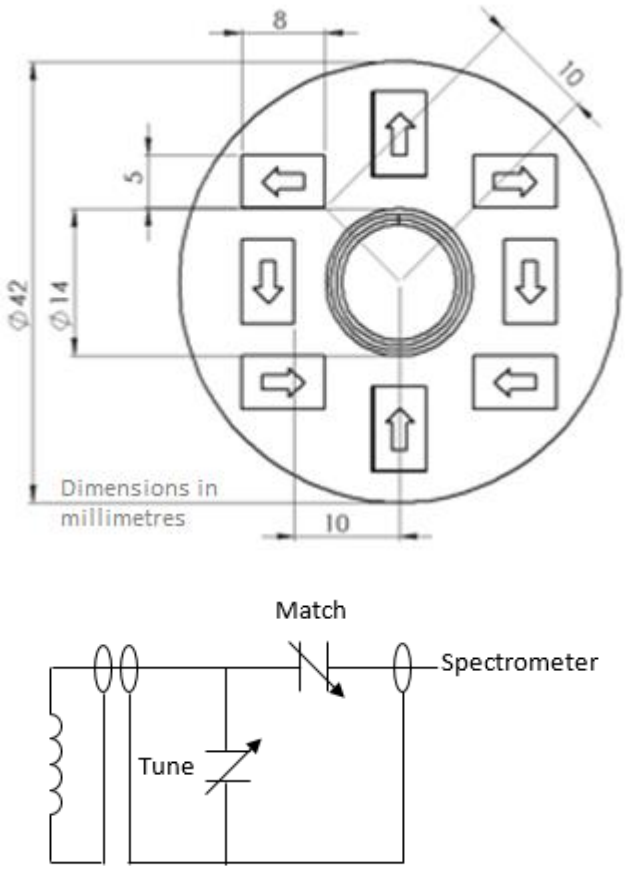

Figure 25: (top) Schematic for the Initial Sensor Design and (bottom) tuning circuit. The arrows on the sensor diagram indicate the north to south direction of the magnet. The pole faces must be arranged in this exact manner when designing an 8-magnet sensor to ensure a strong homoegenous magnetic field inside the bore whilst minimising stray fields outside the sensor. The tuning circuit is composed of variable ceramic capacitors which can change their capacitance through a screw at the surface of the component. Ceramic capacitors are used as they can sustain higher voltages without sparking.

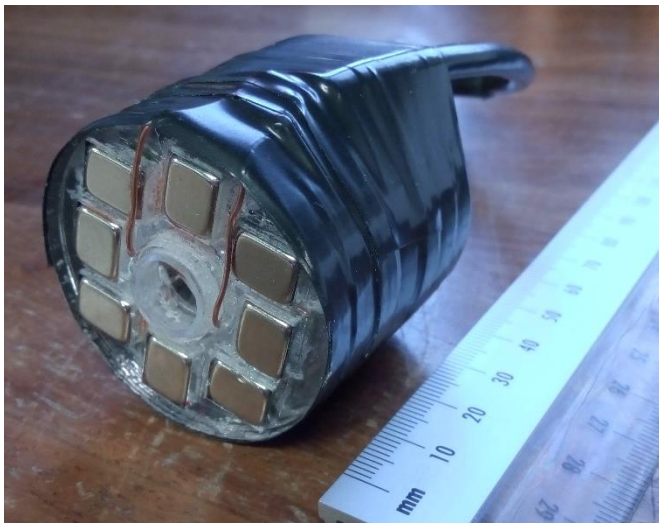

Figure 26: Photograph of finished sensor.

Upon assembly, the sensor and tuning circuit was connected to a KEA^2 Spectrometer (Magritek, New Zealand) which was controlled though its associated Prospa (Magritek, New Zealand) operating software. A CPMG sequence was executed after placing a sample of olive oil inside the sensor using the following parameters: B_1 Frequency = 21.7MHz, Echo Time = 200µs; Number of Echoes = 512; Number of Averages = 256; Pulse Length = 8µs, Repetition Time = 5s.
The result of this scan was a confirmation of a working system. Although not optimized, the sensor demonstrates the capacity to perform NMR measurements.

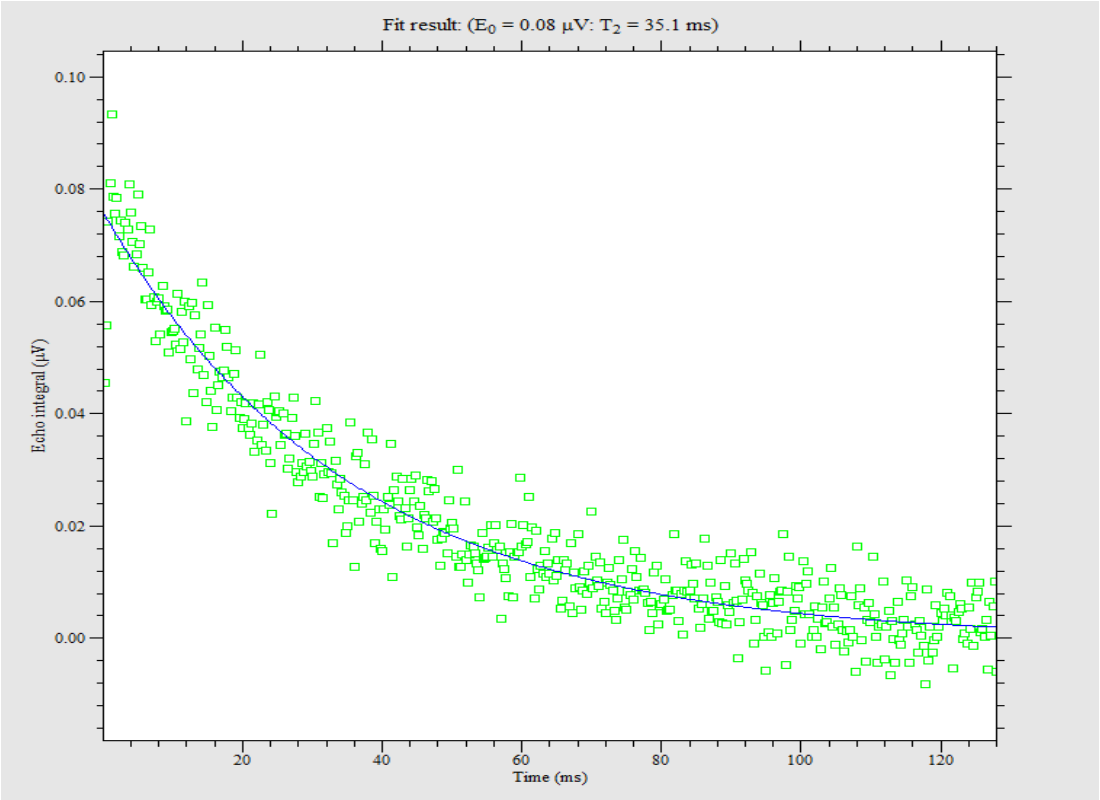

Figure 27: Prospa plot of echo integral for each CPMG echo. An exponential fit has been calculated, but the points are particularly scattered around this fit due to poor optimisation.

2.3.2. Sensor Optimisation

Optimisation of the sensor was performed though a number of steps.

Firstly, the optimal pulse length and RF power was determined. Using Prospa's built-in CPMG sequence, multiple RF powers were tested. It was found that at -18dB for the 90° and -12dB for the 180° settings, there was no sparking or electrical noise emanating from the ceramic capacitors within the tuning circuit. With this power setting in mind, the pulse sequence "CPMGDurationSweep" was executed, in which a CPMG sequence is performed at different pulse durations. The echo train is integrated, and the integral value is plotted against the pulse duration to visually represent the time in which an optimal 90° is obtained. This was found to be 11.7µs at the current -18/-12dB power settings.

The pulse duration and power level determines the bandwidth of frequencies that are excited. This bandwidth is roughly 0.25τ and is centred around B_1 frequency Short pulse durations (in the form of microseconds) at high power will simultaneously excite the entire NMR spectrum whereas long pulse durations (in

milliseconds) will only excite a small region of the spectrum, allowing it to be more selective.

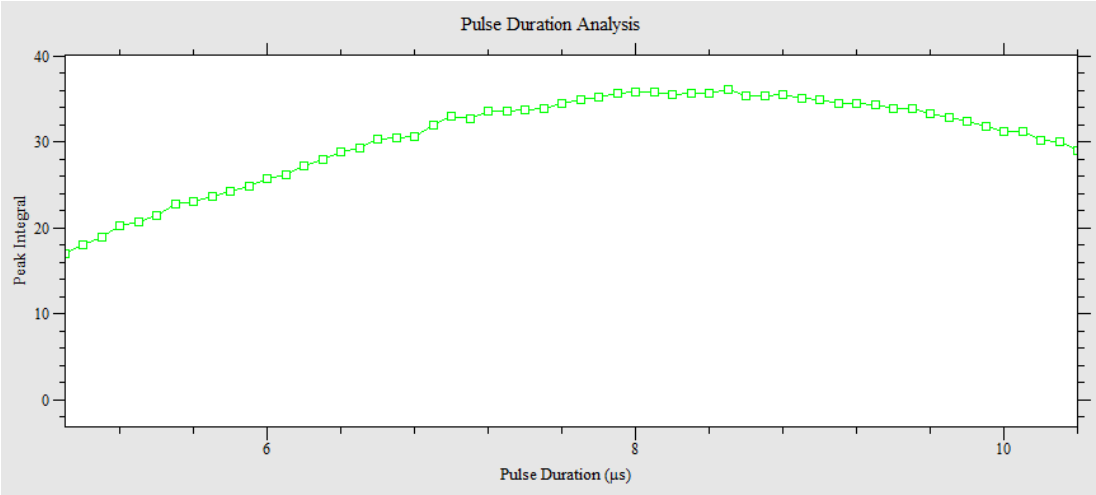

Figure 28: An example of a pulse duration experiment to measure the optimal pulse length. A CPMG sequence is run for different pulse durations and the resultant echo train sum is integrated for a peak integral value. The highest peak integral is measured when the system has performed a perfect 90° pulse.

Secondly, shielding was introduced into the system to provide protection from external RF noise. A copper box was fashioned from copper plates, soldered at the joints and insulated with copper tape at the edges. A Male-to-Male BNC connector was fixed to the front of the shielding box to allow connecting wires to pass through.

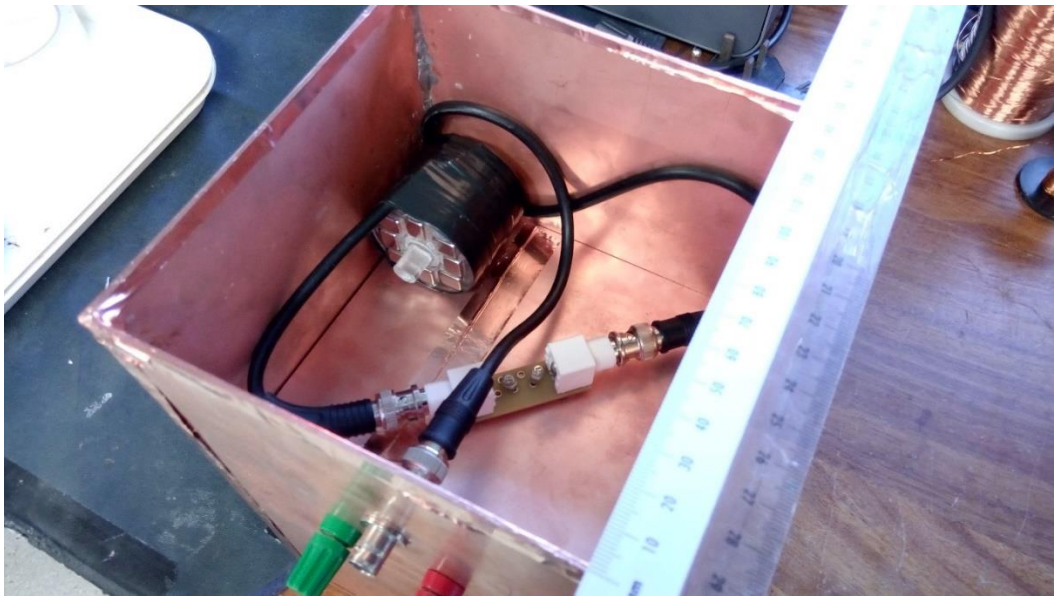

Figure 29: A photograph of the sensor and tuning circuit encased within a copper box to provide RF shielding.

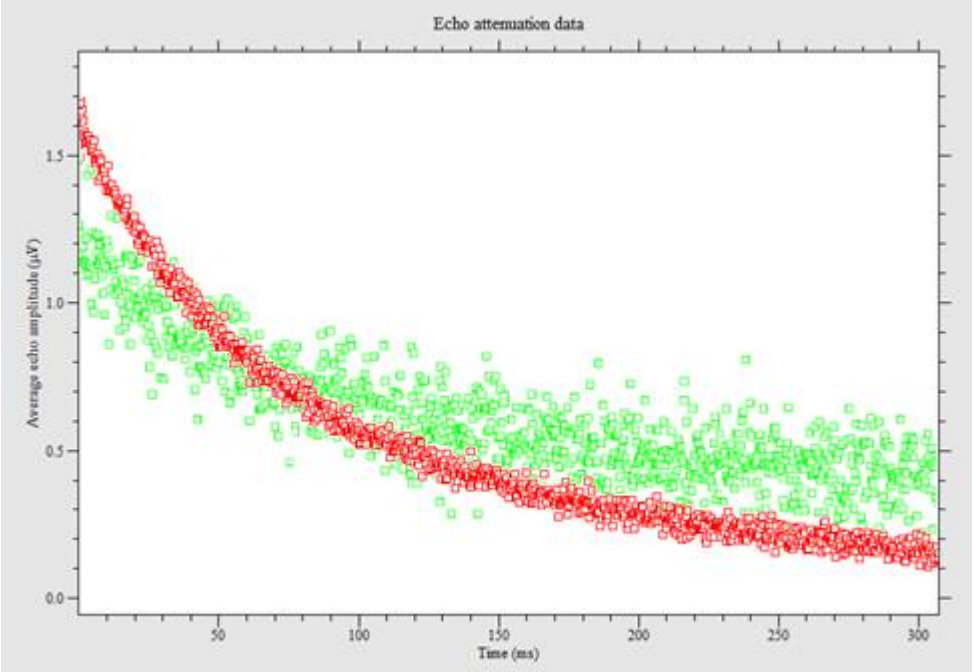

Figure 30: A comparison of CPMG echo trains for a sample of water placed within the shielded sensor (red) and without shielding (green) using the same sample and pulse sequence parameters. As can be seen, the echo integral over time has a much smaller deviation due to the shielding provided by the copper box.

Finally, the necessity of magnetic susceptibility matching was investigated. As a FormLabs 3D printer with a photoresin was available, this was used to provide the

best match for surrounding the solenoid coil. Using the Solidworks software suite, a structure was designed which would allow a solenoid coil to be wound whilst also able to contain an NMR sample fluid. The design was loaded into FormLabs' associated software Preform where it was converted to an STL file and transmitted to the printer for fabrication.

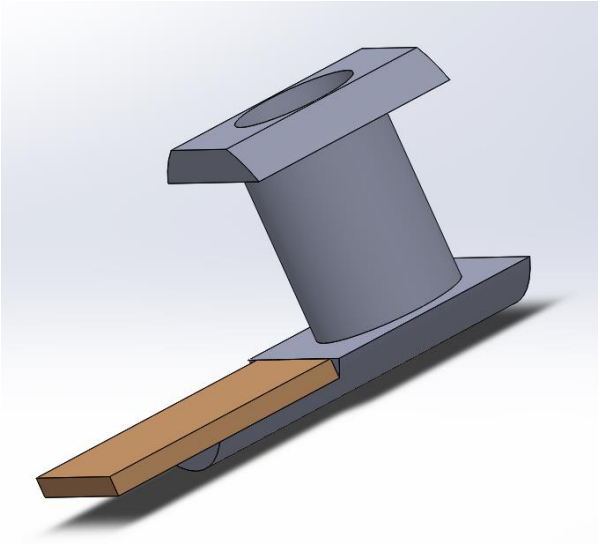

Figure 31: A 3D rendering of the casing used to hold the solenoid RF coil. The coil is wound around the middle section of the structure with the ends soldered to a BNC which is fixed to a copper plate (shown in orange)

Upon creation of the structure, the solenoid coil was wound around the middle section and the well was filled with vegetable oil to provide an NMR signal. After running multiple CPMG readings, the middle section of the structure, where the solenoid coil was wound, was coated in the same photoresin as before allowing it to cure for 8hrs. This process was repeated over the course of three days to ensure a thick enough layer of the resin had coated the coil. Multiple CPMG readings were performed again under the same parameters and with the same vegetable oil to provide signal.

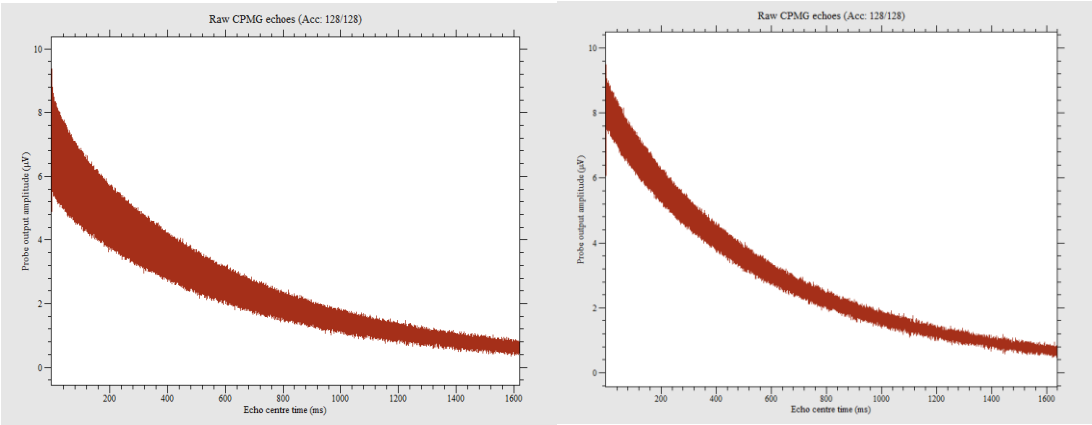

Figure 32: CPMG echo train plots using Prospa. The left plot represents the unmatched coil whereas the right plot represents the matched coil. The use of photoresin to match the magnetic susceptibility of the structure results in a smaller amount of noise as demonstrated in the smaller deviation of echo integrals, particularly at the beginning of the echo sequence.

2.3.3. Magnetic Field Strength Mapping

As the Halbach geometry proved to be a reliable design, the magnetic field inside the bore was mapped as a function of displacement through the central bore. The idea behind this exercise was to gain a greater understanding of the sensor's homogenous region to which future measurement samples could be tailored around this restriction.

Initial measurements were performed on the small 8-magnet Halbach using a Gauss meter mounted onto an adjustable clamp. The Gauss probe was lowered gradually through the central bore where the field was recorded from the display.

The 42mm long magnets demonstrate a small, 3mm region of homogeneity in the centre of the bore. Unfortunately, this region is not large enough to accommodate the entire width of a commercial well plate but is large enough for an NMR sample tube. Using this information, it was hypothesised that longer magnets could, in turn, create a larger region of homogeneity through the bore. Magnets of 130mm length were available from the same retailer leading to the purchase of 20.

These magnets were arranged inside a new acrylic shell, specifically designed to accommodate a 16-magnet Halbach arrangement.

The field was mapped with a gauss probe to determine the field strength at varying depths through the centre of the bore. This was performed for a 4, 8 and 16-magnet

arrangement to determine if the number of magnets in the geometry contributed to overall strength and homogeneity.

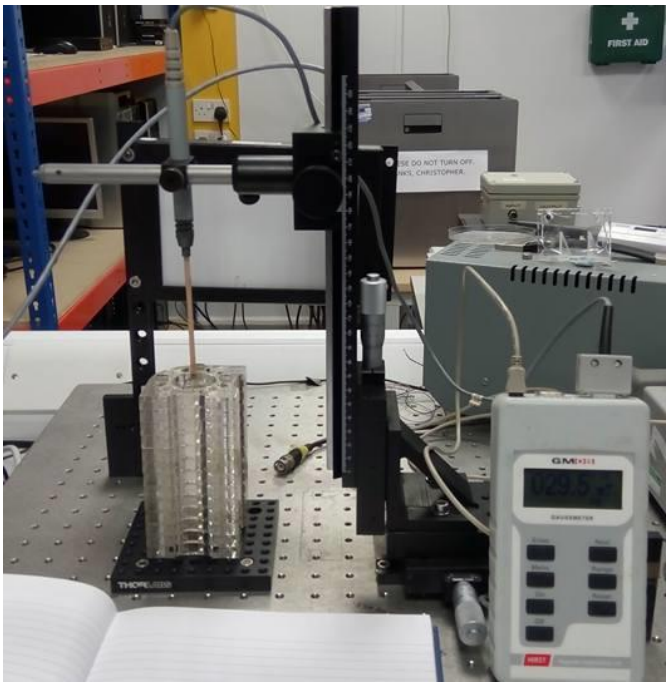

Figure 33: Photograph of the setup used to map the magnetic field of the centre of an NMR sensor. Adjustments can be made simply by rotating the dial on the mount, which lowers the Gauss probe by a controllable amount.

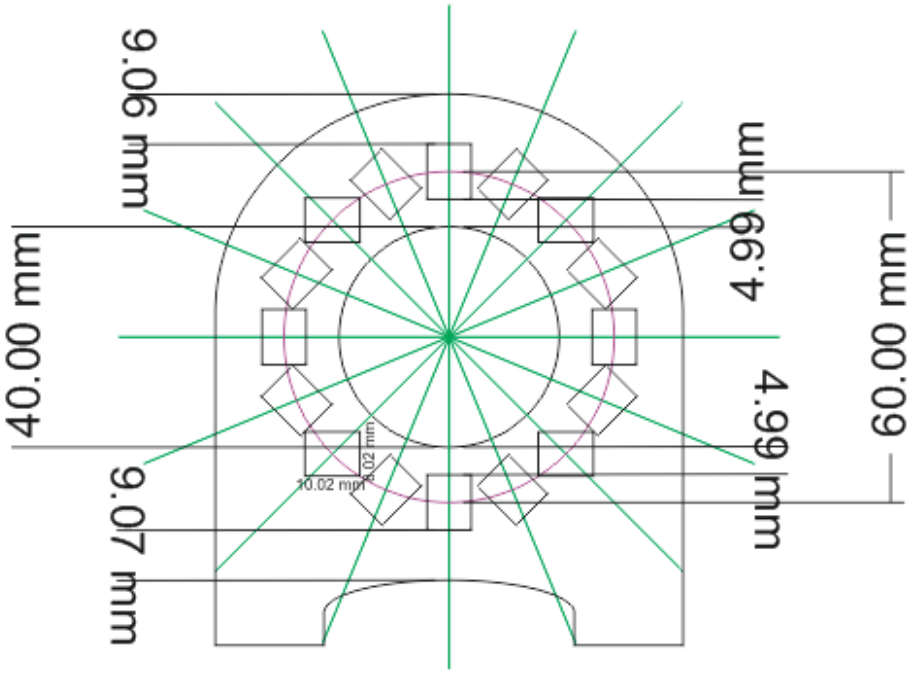

Figure 34: A schematic of the casing constructed to house up to 16 magnets.

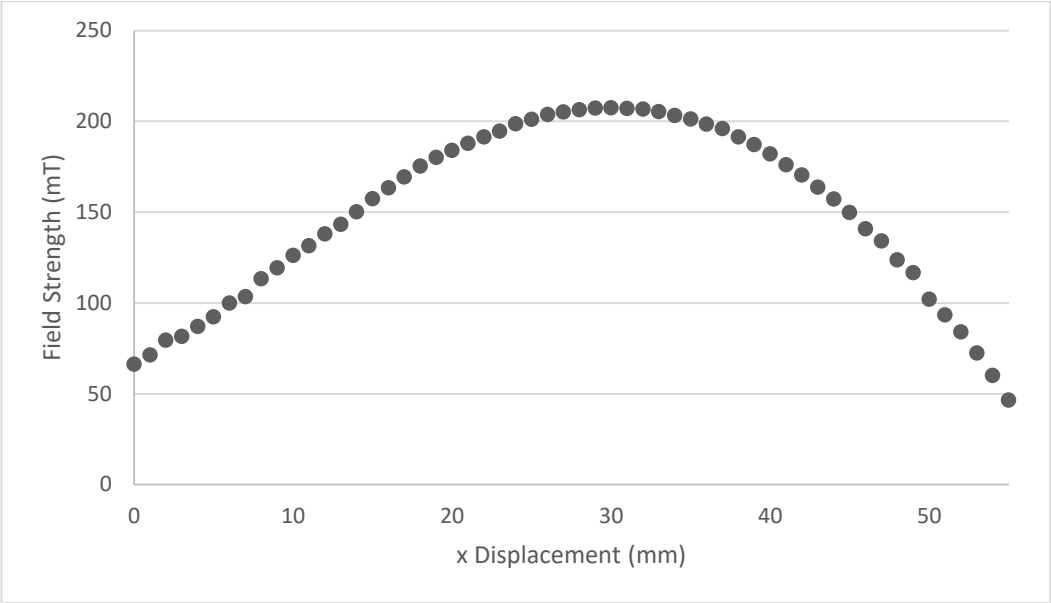

Figure 35: The magnetic field strength through the bore of the 8-magnet NMR sensor using magnets of 42mm length.

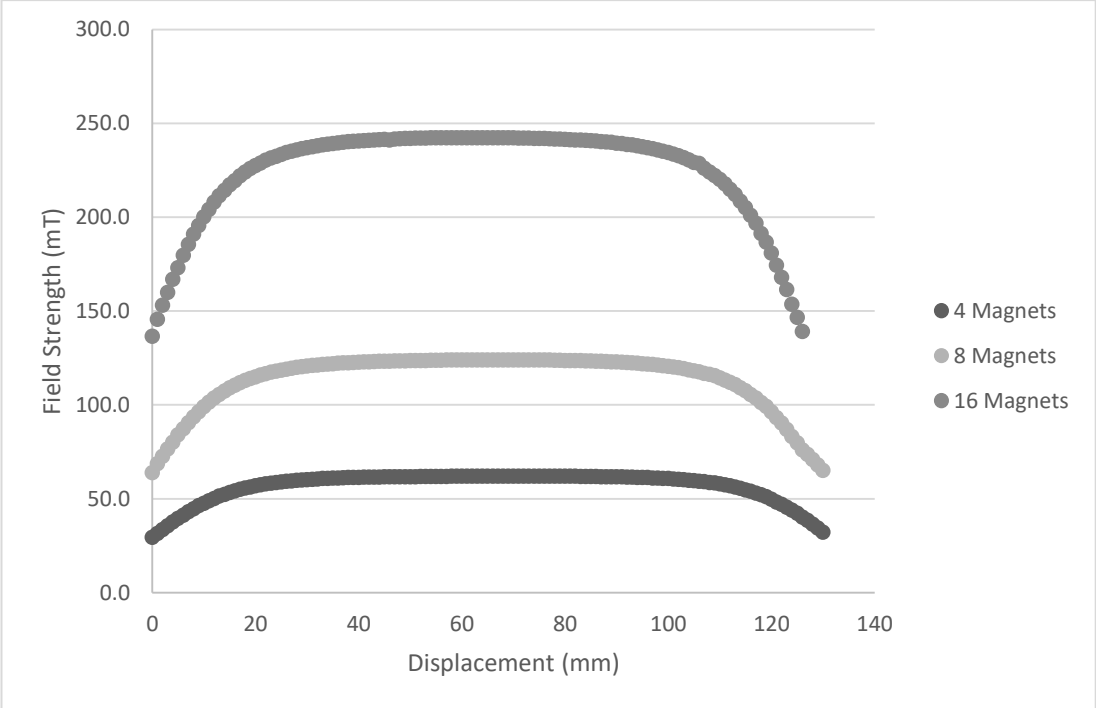

Figure 36: The magnetic field strength through the bore of the 16-magnet NMR sensor using magnets of 130mm length. The plot demonstrates the field strength when the sensor is comprised of 4, 8 and 16 magnets.

The homogeneity of the sensor was assessed by measuring the total distance through the centre of the bore in which the magnetic field strength remains the

same to one decimal place due to limitations in the sensitivity of the gauss probe. For 4 magnets, the magnetic field strength remained at a constant 61.9mT for 24mm through the bore. When 8 magnets were used, the magnetic field strength increased to 123.9mT, but only held steady at this value for 16mm through the bore. Finally, when 16 magnets were used, the magnetic field strength almost doubled to 242.3mT, but only remained at this value for 11mm through the bore. An increase of the number of magnets present in the design increases the strength of the field, but also decreases its homogenous region. Utilising this information it is possible to balance the requirements of field strength and sensitivity with the homogeneity of the field based on the relative size of the sample being investigated.

2.4. Limits of Detection

To automate the process of detecting MNP, a suitable fluid must be investigated. To create a bigger contrast between the blank and reference samples, the T_2^{eff} value of this fluid needs to be suitably long. Ideally, the decay should be mono-exponential to allow for easier processing and the fluid must be proton rich, to allow for a measurable signal at small volumes

2.4.1. Fluid Optimisation for T_2 Analysis

The optimum detection fluid was determined by collecting data from several different candidates including various cooking oils, water and silicone oils. A CPMG sequence with the following parameters was used to collect the echo trains: Echo Time=400µs; Number of echoes=4096; Number of averages=128; Pulse length=11.7µs, Repetition time=2s. The collected echoes were transformed using a Lawson and Hanson non-negative least squares (NNLS) analysis within the Prospa software, producing a relaxation spectrum which provides the relative weighting of each relaxation component. For example, a mono-exponential T_2^{eff} decay will produce a single peak centred at its T_2^{eff} value, whilst a bi-exponential will have two peaks one centred on each of the components' T_2^{eff} values with the heights representing their relative magnitudes.

Diffusion measurements of the test fluids were determined using an NMR-MoUSE® (Magritek, Wellington, New Zealand) in conjunction with an alternative spectrometer (Apollo LF, Tecmag, US). These measurements were made to ensure a fluid with high diffusive properties was selected, as molecules with a higher degree of movement are more likely to come into close proximity of immobilised MNP, enhancing the relaxation effect.

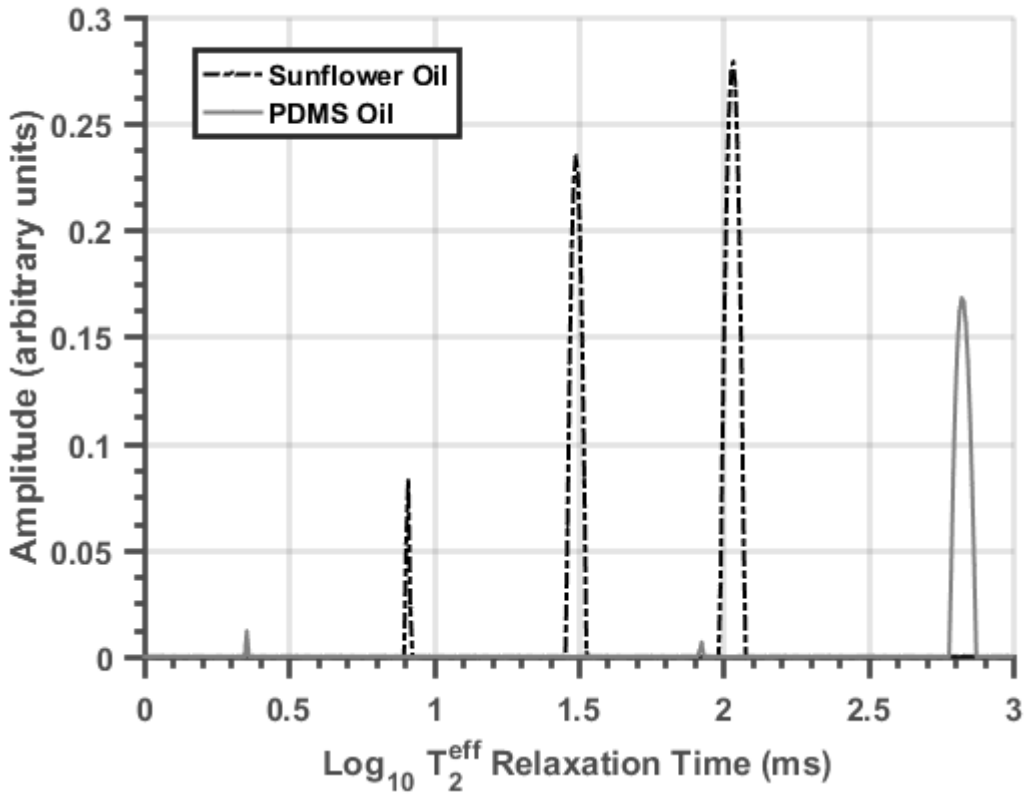

Figure 37: A relaxation spectrum of sunflower oil and PDMS produced by an NNLS transformation of respective echo train plots.

A relaxation spectrum for 10cSt polydimethylsiloxane (PDMS) oil and sunflower oil demonstrates the different T_2^{eff} components. The PDMS oil shows one dominant and two negligible peaks, whereas the sunflower oil has three significant relaxation components.

Due to its mono-exponential T_2^{eff} relaxation time, PDMS was selected as the ideal imaging fluid in this category.

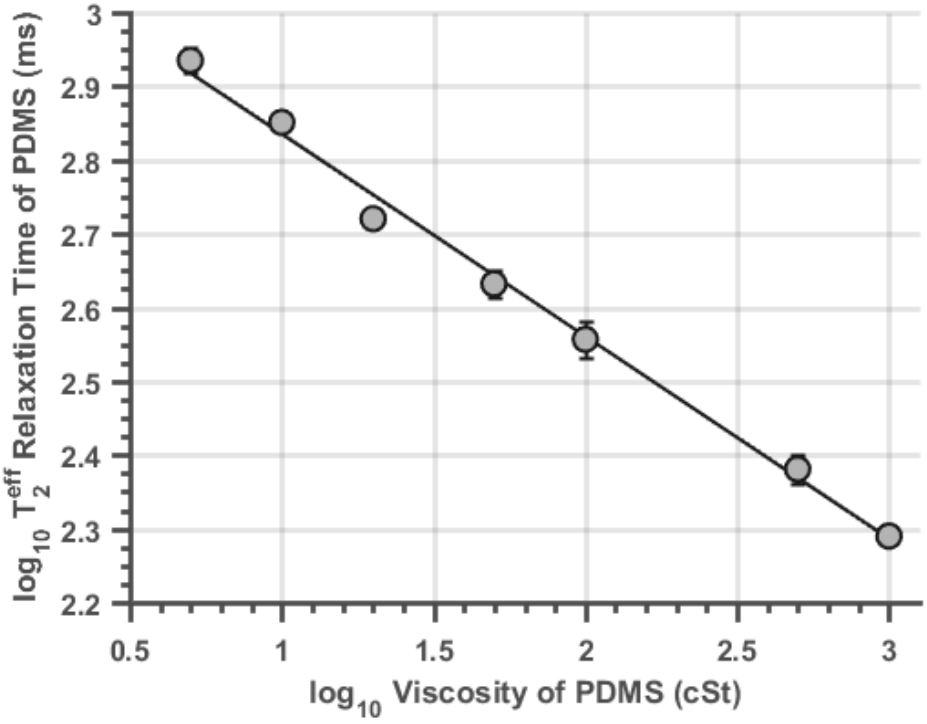

Figure 38: The linear relationship between the logarithmic T2eff relaxation time and the viscosity of PDMS.

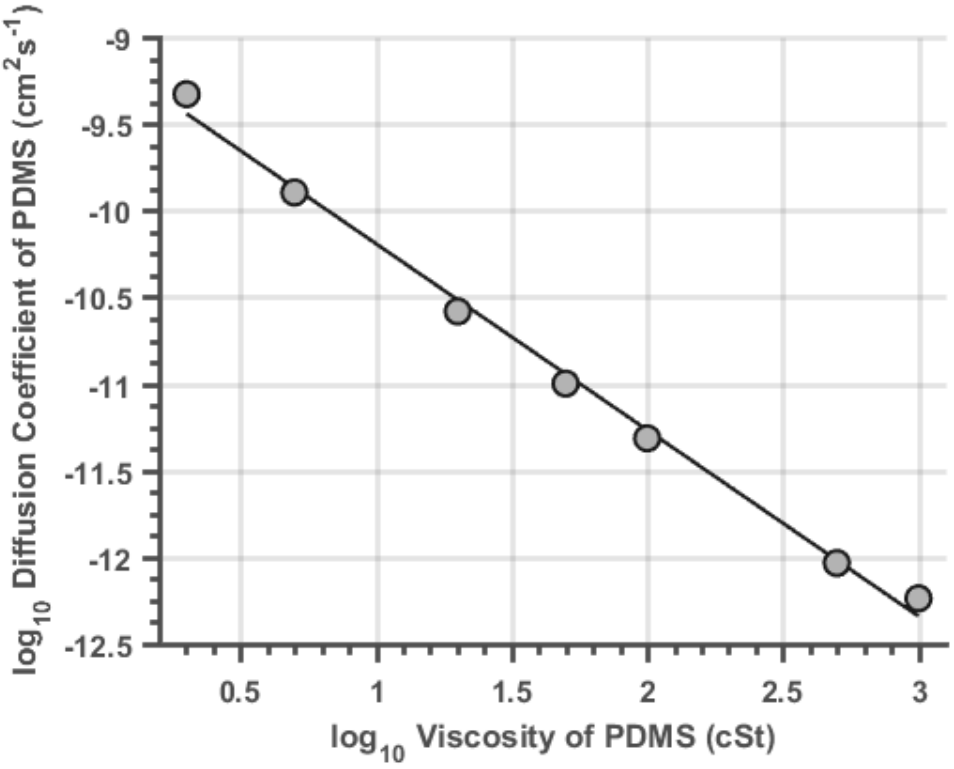

Figure 39: The linear relationship between the logarithmic diffusion coefficient and viscosity of PDMS.

From the data gathered from the NMR-MoUSE, a direct correlation was found between both diffusion coefficient and T_2^{eff} values with the oil's viscosity. Higher viscosity PDMS demonstrated a much lower diffusion, and a lower T_2^{eff} relaxation time. T_2^{eff} changes due to the presence of magnetic perturbations will become larger with higher values of self-diffusion coefficient making high viscosity PDMS a suboptimal choice as the imaging fluid.
10cSt PDMS was selected as the optimal viscosity of the imaging fluid due to its high self-diffusion coefficient.

2.4.2. Investigation of Sensor Sensitivity

Different physical thicknesses of the 10cSt PDMS oil layer were investigated to find the thinnest layer that would provide a sufficiently reproducible T_2^{eff} value. The thinner the layer of fluid covering the immobilised MNP, the closer the molecules are to the particles, enhancing the relaxation effect. Acrylic (PMMA) test sticks were cut with a commercial Laser Cutter (M-300, 40W, Universal Laser Systems, T_x, US) from a 6mm thick sheet of extruded acrylic. A 4mm deep indentation was etched into the sticks so that the imaging fluid could be contained. These sticks were then placed within the sensor and assessed.

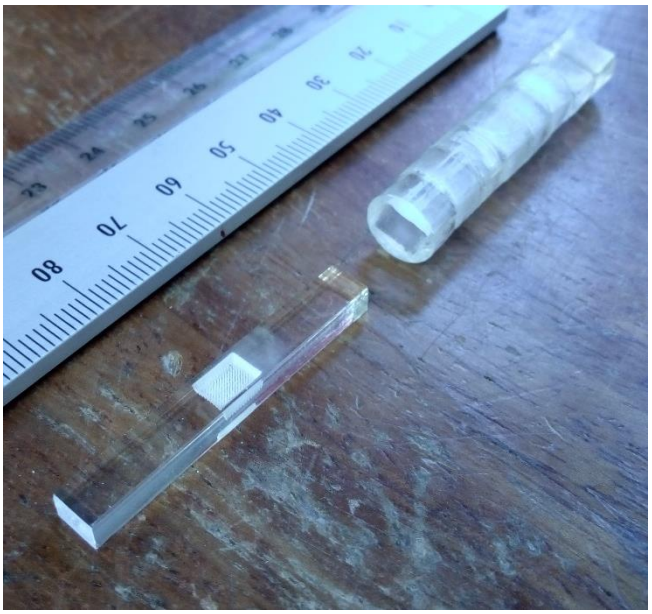

Figure 40: A photograph of the test stick with the rastered indentation besides the holder used to centralise the sample.

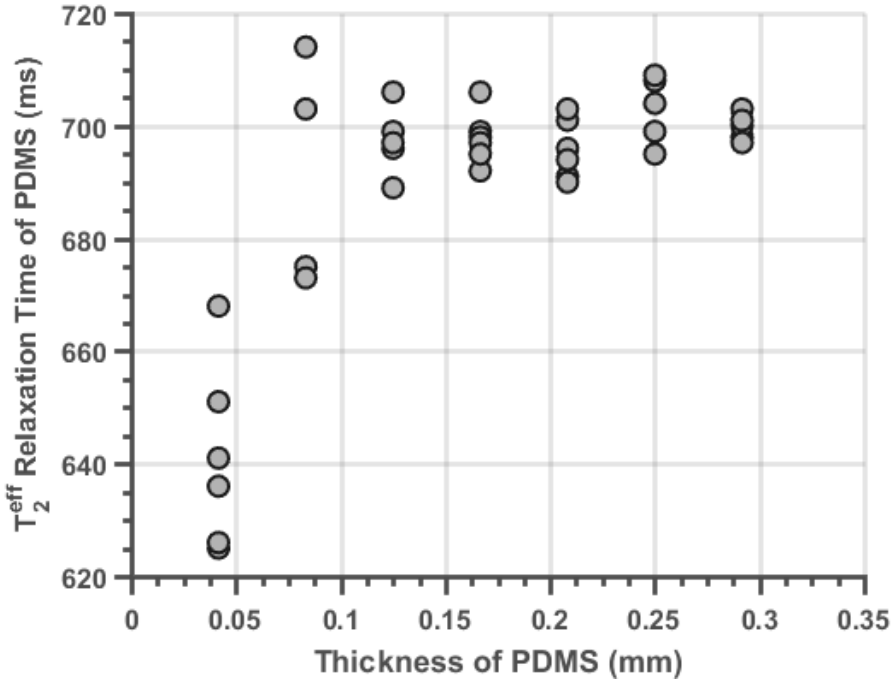

Figure 41: The recorded T_2^{eff} relaxation time of PDMS against thickness.

Values below 125µm showed significant increase in scatter of the data due to poor filling factor of the coil as well as a reduction of the measured T_2^{eff} which is an undesirable trend. When the PDMS was at a thickness of 75µm, there was a standard deviation of 19ms, compared to 5ms when a thickness of 125µm was used. Therefore 125µm, corresponding to a volume of 3µL of PDMS, was selected as the minimum value that could be accurately detected within this system.

2.5. Nanoparticle Assays

With a working sensor and an ideal fluid identified, the nanoparticle assay could be designed. As discussed previously, biotin and avidin interactions have been demonstrated to work when attempting to surface immobilise an iron nanoparticle to a surface. As biotin coated polystyrene well plates (Pierce™ Biotin Coated Plates, Fisher, UK) and avidin coated, fluorescently labelled superparamagnetic iron oxide (BNF-starch-redF 100nm, Micromod Partikeltechnologie GmbH, Germany) were commercially available, this combination of reagents was used to assess the detection strategy.

2.5.1. Techniques for Controlling SPIO Binding – Laser Rastering

A controlled fraction of the surface of each of biotin well plates were laser engraved to remove specific quantities of the surface Biotin. These were washed in a solution of phosphate-buffered saline (PBS) (Sigma Aldrich, US) and air dried. The Avidin coated MNPs were purchased in a suspension of PBS to a concentration of 0.5% w/v which provided an appropriate concentration for binding. 20µL of this solution was placed onto the biotin coated plate and incubated at room temperature for 30 minutes before washing again in the solution of PBS to remove excess, unbound MNPs. The well plates were then air dried for 8 hours.

2.5.2. Bound SPIO Confocal Microscopy

Using a confocal microscope (Leica SP5, Leica Microsystems GmbH, Germany), bright field and fluorescence images were obtained for each of the wells to confirm the presence of immobilised MNP

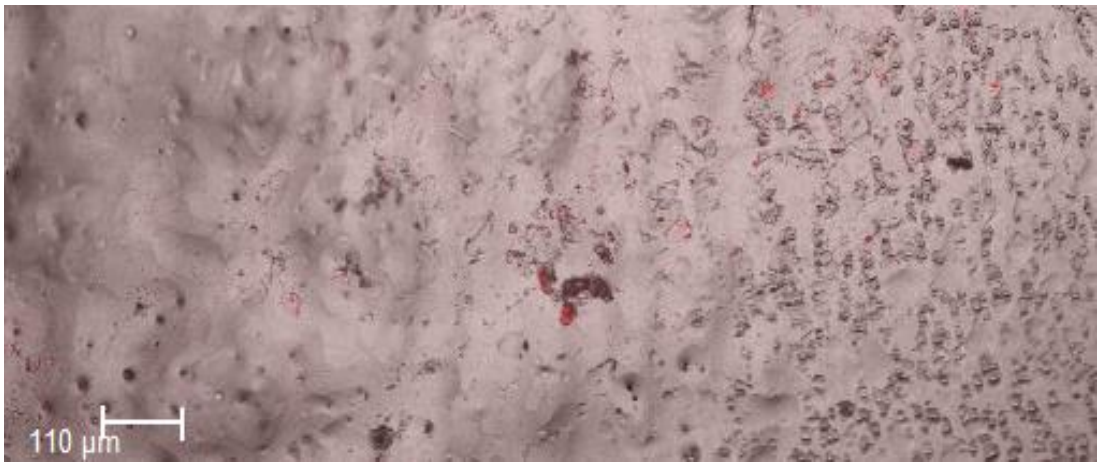

Figure 42: Confocal fluorescence image demonstrating higher binding concentration on non-rastered (right) region. With a large amount of surface biotin removed in the laser ablated region (left), there is a much smaller concentration of bound MNP seen as black spots in the confocal image.

In the rastered regions, a majority of the surface ligand has been ablated, removing the binding sites for the avidin coated nanoparticles to bind. The result is a massive reduction, but not entire prevention, of immobilised MNP in the rastered section.

In the un-rastered regions where the surface ligand has been untouched, the avidin coated MNP conglomerate in clusters.

To estimate the percentage of surface immobilisation, the confocal image was loaded into the graphical analysis software ImageJ. There, the image was converted to 8-bit greyscale and the contrast was enhanced by 1% to remove as much of the shadowing as possible and highlight the immobilised MNP. Upon applying the contrast enhancement, a black/white threshold algorithm was performed on the image. Any pixel assigned a pixel value of 126 and under was assigned a value of 0, converting it to white. Any pixel assigned a pixel value of 127 and over was assigned a value of 256 converting it to black. The thresholded image is demonstrated below.

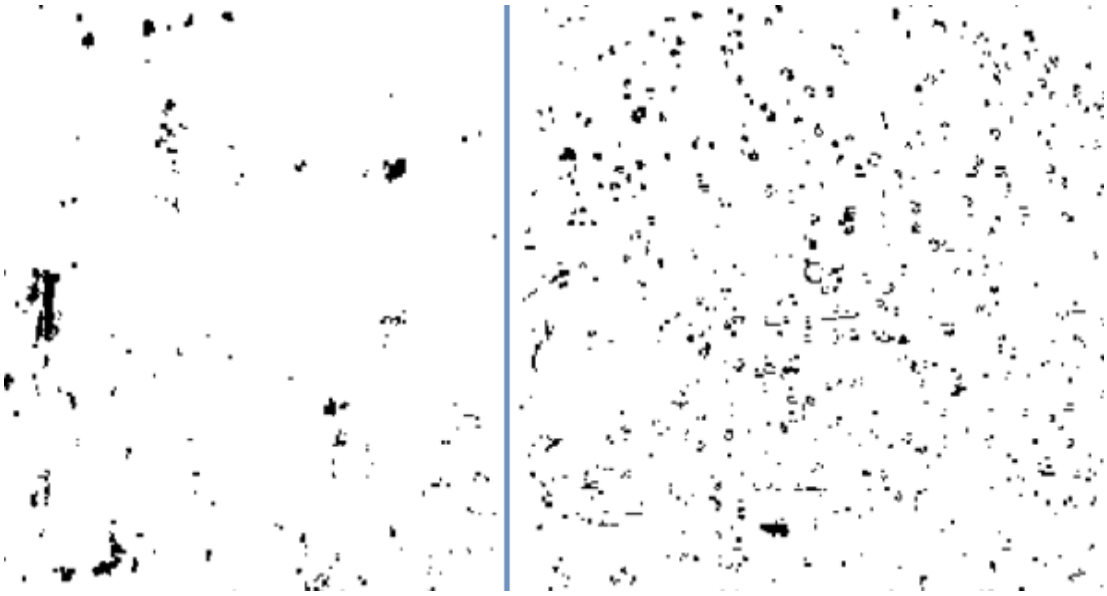

Figure 43: Binding bright-field image after a 1% contrast enhancement and a threshold was applied. The line drawn demonstrates the region in which the distinction was made between the rastered (left) region and the non-rastered (right) region.

Random regions of the rastered and non-rastered sections were selected with ImageJ's rectangle tool, where a histogram was plotted to compare the number of white pixels (no binding) to the number of black pixels (binding).

MNP coverage was calculated to be 26±2% for the non-rastered section and 2.8±0.9% for the rastered region, demonstrating that although the rastering technique is not 100% effective, there is still an 89% reduction in surface coverage of bound MNP.

Magnetic Guidance is a technique utilised by numerous authors(Duguet et al., 2006; Indira, 2010; Lee et al., 2015; Senyei et al., 1978) when using magnetic nanoparticles in biomedical applications. Using a magnet, nanoparticles are directed to binding sites through the use of magnetic fields. This strategy was used to investigate if the surface coverage could be improved.

Streptavidin coated nanoparticles were placed in solution into biotin coated well plates. The well plate was positioned on top of a 0.5T NdFeB permanent magnet and incubated for 30 minutes at room temperature before washing excess particles out with a PBS wash. A secondary control well was also designed using the same method but placing it away from the magnet.

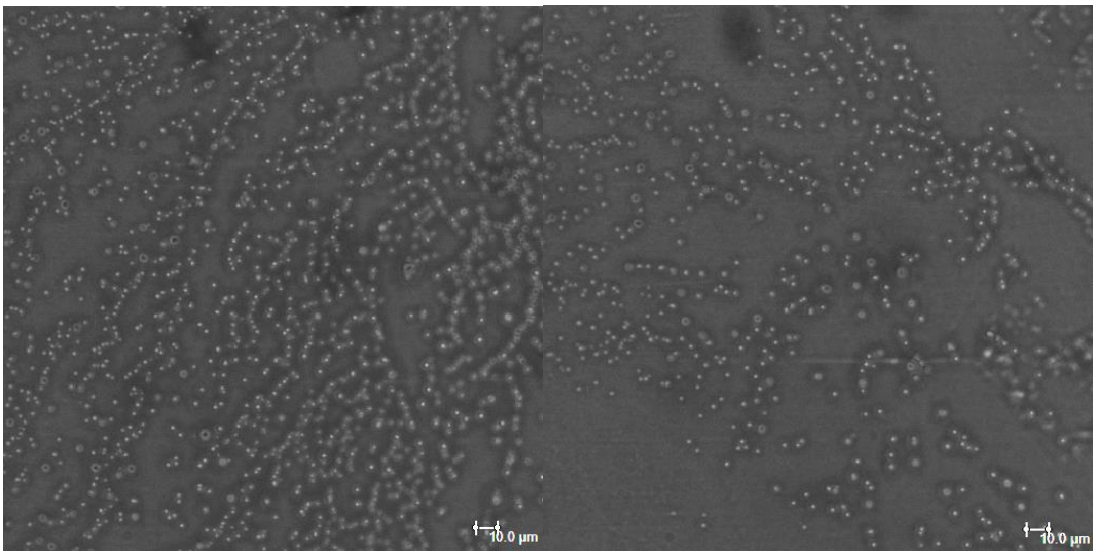

Figure 44: Confocal bright-field images of two well plates utilising (right) the magnetic guidance technique and (left) the control. There is a noticeable reduction in the number of bound particles when using the guidance technique as well as noticeable "dead spots" were no circles can be seen.

For the purposes of the well plate design, the magnetic guidance technique appeared to reduce the surface coverage of the nanoparticles. Upon using ImageJ to threshold the image to estimate the surface coverage it was calculated that the magnetic guidance technique corresponded to coverage of 21±2%, 5% lower than the original method in which no magnet was used. Upon investigating microscopy images, it appears that the particles were attracted to specific regions, leaving areas

of the well plate virtually clear of any bound particles. A hypothesis is that the particles were following magnetic field lines.

Moving forward, the guidance technique will not be used for this specific binding strategy.

2.5.3. Assay Designs

The laser cutter was used to cut rectangular (4x6mm) sheets out of the biotin coated well plates which would fit inside the indentation etched into the test sticks used in the previous Limits of Detection study (2.4). To limit the amount of PDMS required to submerge the MNP, and to account for the surface roughness due to laser rastering in the base of the test stick well, the etched MNP coated plates were placed upside-down into the holder.

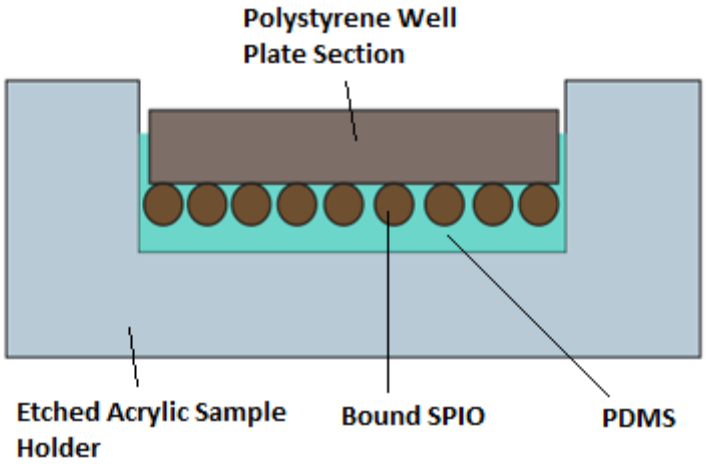

Figure 45: Basic schematic of how the cut well plate with surface bound MNP sits inside the acrylic test stick.

A number of samples were prepared from etched biotin plates that had different amounts of the surface biotin ablated through the rastering process. The MNP solution was applied to these etched plates to enable binding of the nanoparticles providing samples with differing amounts of bound MNP.

6µL of PDMS was added to the wells to complete the assay design of an etched plate with bound MNP, surrounded with a thin layer of PDMS and contained within

a shell that would allow it to be placed into the sensitive region of the magnetic sensor.

2.5.4. Nanoparticle Selection

Iron oxide particles were available in 2.8µm and 1.05µm as streptavidin coated Dynabeads (Thermofischer, Waltham, MA, USA). These particles were purchased to perform an experiment to observe the effect of nanoparticle size on T_1 and T_2^{eff} relaxation time. Using thetechical data sheet provided by the supplier, the density of the Micromod nanoparticles used earlier was found to be $1.4gcm^{-3}$ with an iron concentration of $2.4mgml^{-1}$. No information on density or iron concentration was supplied for the Dynabeads.

20µL of each nano/micro particle solution was pipetted onto biotin plates and incubated at room temperature for 30 minutes before using a PBS wash to remove excess, unbound particles. The plates were fashioned into the assay discussed in the previous section before being placed inside the NMR sensor to measure T_1 and T_2^{eff} relaxation time though inversion recovery and CPMG sequences respectively.

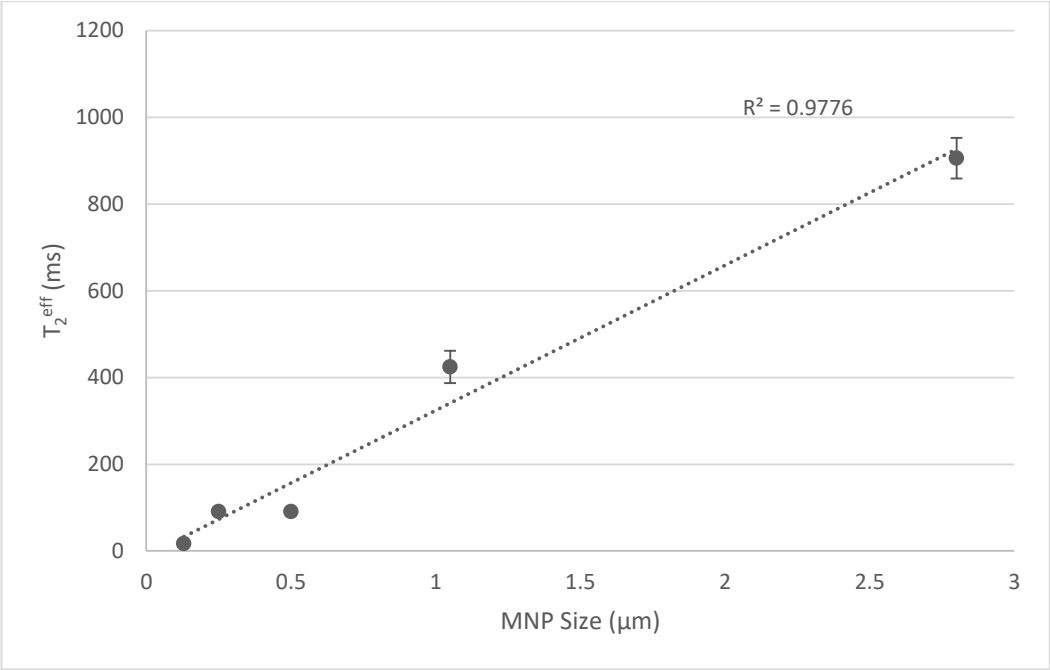

Figure 46: The effect of MNP size on the T_2^{eff} relaxation time. The smaller micromod particles all have the same iron concentration and density presenting the idea that smaller particles lead to a higher contrast. The iron concentration and density of the two larger Dynabeads is unknown so density could be a contributing factor to the overserved T_2^{eff} change.

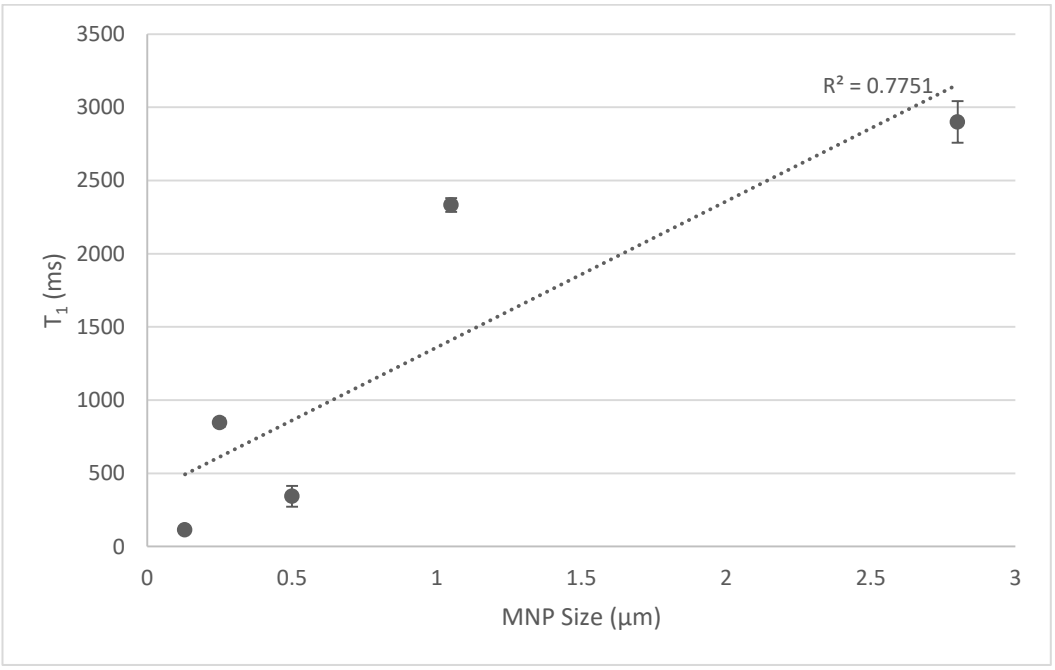

Figure 47: T_1 relaxation time as a function of MNP size. Like before, the smaller particles lead to a higher contrast, reducing the T_1 relaxation time of nearby protons. However, the correlation between T_1 contrast and MNP size is less reliable than the correlation between MNP size and T_2^{eff} contrast.

It was discovered that the smaller particles had a much greater effect on reducing T_1 and T_2^{eff} relaxation times over their larger counterparts. The effect on T_2^{eff} is much more reliable with very little deviation from the linear fit assigned although on the other hand, the effect on T_1 is much less reliable.

2.6. T_2 Magnetic Resonance Disruption (T_2-MaRDi)

With many of the system optimisations and necessary reagents selected, it was time to use the equipment and reagents to perform a series of experiments.

2.6.1. Measuring T_2 Effects

Using the laser rastering technique, regions of a biotin well plate were ablated to reduce the surface area of available biotin binding sites. An increase in the amount of surface biotin ablated leads to a smaller area in which the MNP can bind. The sample sticks of varying MNP coverage were placed inside the magnetic sensor where a CPMG sequence was executed using the following parameters: Echo Time = 400µs; Number of Echoes = 4096; Number of Averages = 128; Pulse Length = 11.7µs, Repetition Time = 2s.

A monoexponential fit was assigned to the integral value of the signal for each echo to provide a measurement for T_2^{eff}.

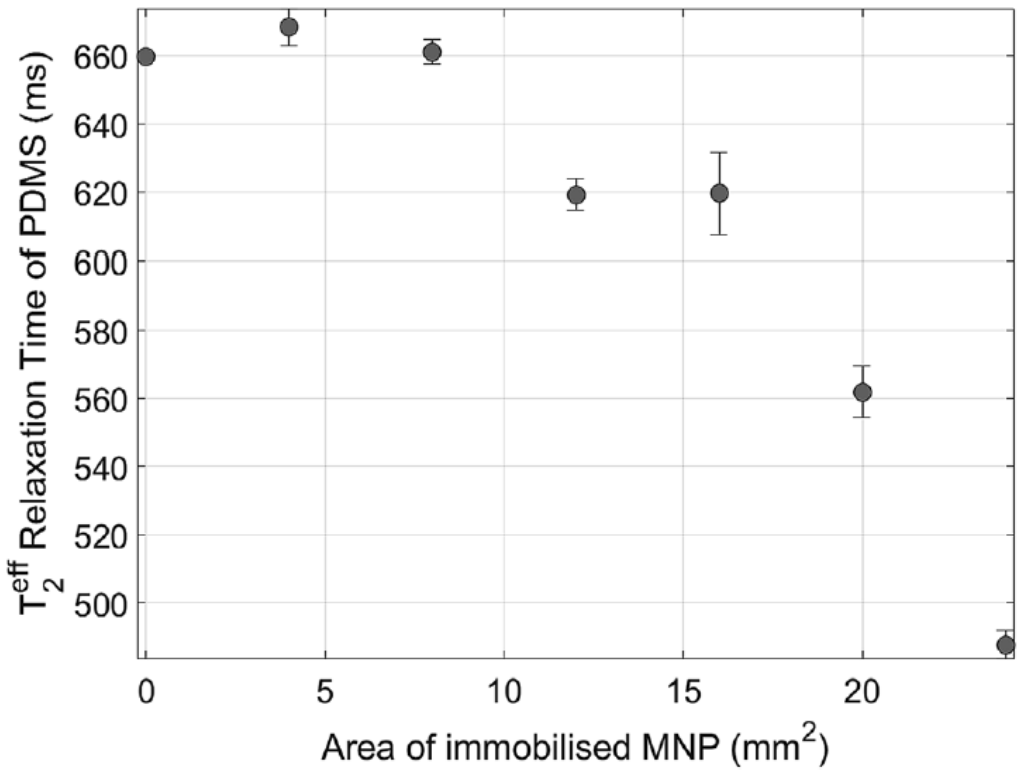

Figure 48: As more of the surface biotin is ablated from the well plates there is a reduction of the amount of available binding sites and therefore a decrease in the amount of paramagnetic material present. Larger amounts of paramagnetic material lead to an increased rate of dephasing for nearby protons and a reduction in the sample's T_2^{eff} relaxation time.

As the area of immobilised MNP increases, there is a non-linear reduction in the T_2^{eff}. From this, it is shown that there is little effect on T_2^{eff} for a coverage of less than 7% which highlights a minimum threshold for a reduction in relaxation time.

2.6.2. Measuring Echo Integral Effects

The sample sticks of varying MNP coverage were again placed inside the magnetic sensor where a CPMG sequence was executed using the following parameters: Echo Time = 400µs; Number of Echoes = 4096; Number of Averages = 128; Pulse Length = 11.7µs, Repetition Time = 2s.

Another data set was acquired with the same parameters, but with the number of echoes set to 1. A single echo measurement was chosen to see if this measurement was reliable, as a single echo acquisition would be easier to design electronics for when considering a miniaturised point of care device. 512 averages were used for

the single echo to provide a more reliable measurement due to large variations in the measured echo integral.

The echo sum was integrated for both 1 and 4096 echoes and compared to the area of immobilised MNP on the sample stick.

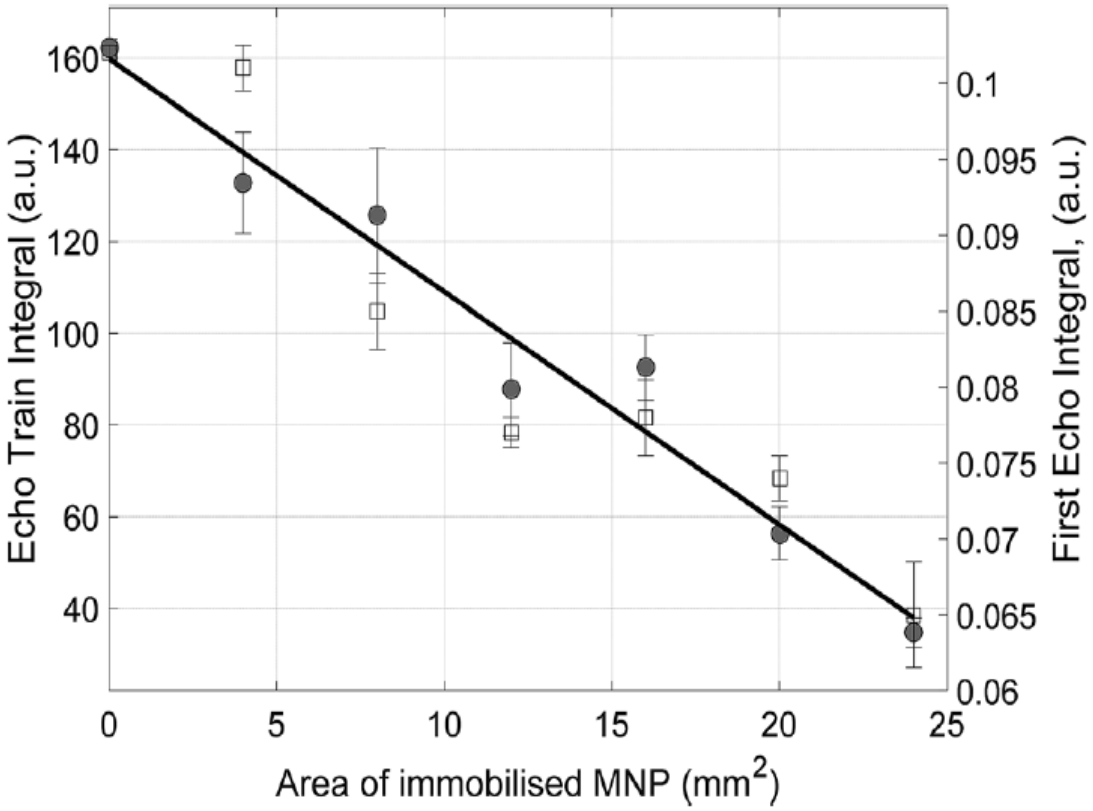

Figure 49: The integral of 4096 echoes (filled circles, left axis) and the integral of the first echo (open squares, right axis) as a function of the area of immobilised MNP. The regression lines of both data sets lie on top of each other for these scales although their parameters are different. The error bars on the first echo integral are smaller as a larger number of averages were taken due to large fluctuations in the measured echo integral.

A linear decrease in the signal amplitude, taken as the integral of 4096 echoes, as a function of the percentage of the surface area covered in MNP is demonstrated. This same trend is also apparent for the integral of the first echo alone, although this is less sensitive and requires more averaging to produce reliable results.

2.7. T_1 Magnetic Resonance Disruption (T_1-MaRDi)

As iron oxide nanoparticles were successful in reliably disrupting the MR signal during T_2^{eff} relaxation time measurements, a few more experiments were performed to see if inversion recovery or saturation recovery sequences could also provide a reliable measurement of magnetic resonance disruption during T_1 relaxation experiments. As iron oxide particles had already been investigated as a T_1 contrast agent with a lower degree of success, it was necessary to look for a different nanoparticle.

2.7.1. Gadolinium in Solution

Iron oxide particles were not providing a desirable trend between nanoparticle size and T_1, so a new contrast agent was sought for measurement of T_1 relaxation times through inversion recovery. Gadolinium was selected due to its prevalent use in MRI. Due to the inaccessibility of functionalised gadolinium, gadolinium salt (DTPA-bis(stearylamide) (gadolinium salt), Sigma Aldrich) was purchased and made up to varying concentrations in a solution of methanol.

These Gd solutions were placed within the sensor and an inversion recovery sequence was performed to measure the T_1 relaxation time at each concentration to investigate any changes.

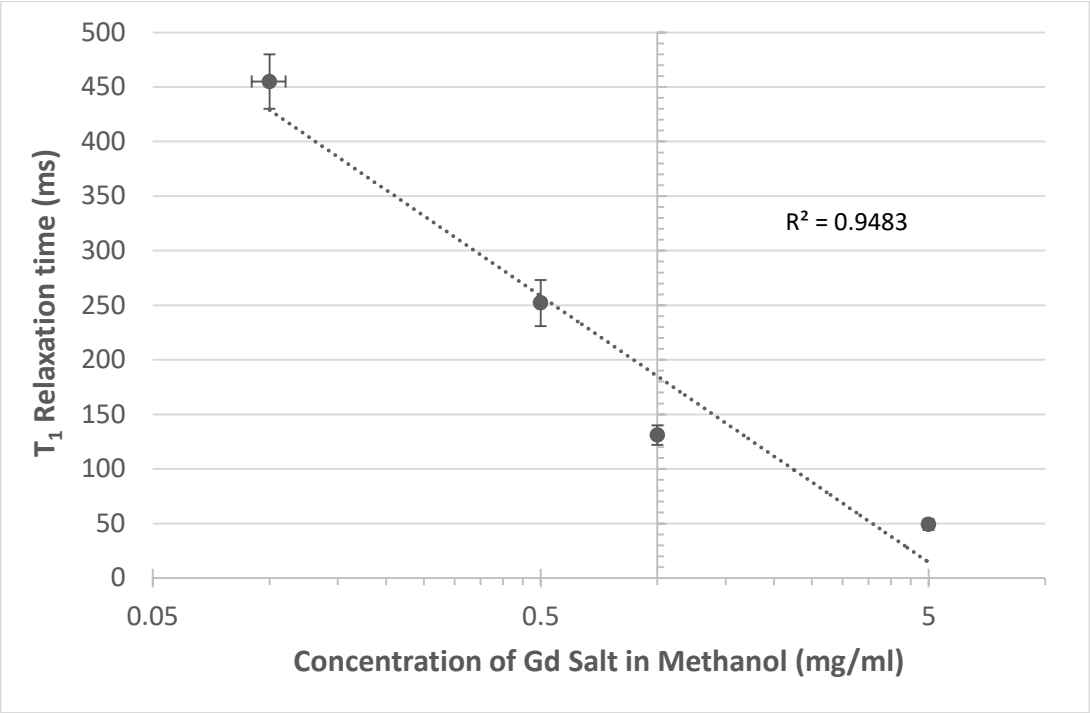

Figure 50: The T_1 relaxation time of differing concentrations of gadolinium salt dissolved in methanol. As the concentration increases, there is a reduction in the spin-lattice relaxation time.

The T_1 relaxation time was shown to decrease logarithmically with respect to the concentration of Gd in methanol with a more reliable fit than demonstrated earlier with iron oxide particles.

2.8. Conclusions

An NMR sensor created from a Halbach magnet arrangement was used for the detection of magnetic nanoparticles bound to a polystyrene surface. A previous study has identified methods of detecting immobilised nanoparticles using MRI, but the necessary size of MRI machines makes them expensive and undesirable to institutions with limited space or finances. As such, this study aimed to replicate this detection method through the use of inexpensive permanent magnets and commercially available electronics with the aim of building a system with the functionality of point of care (PoC) diagnostic system.

A Halbach probe was selected as the optimal geometry due to its high field strength and homogeneity in comparison to other unilateral geometries such as the NMR-

MoUSE. Many of the experiments were performed on a compact 8-magnet Halbach due to its functionality and its small size and relatively low weight making it much more suitable for a portable device over larger Halbach systems built with longer or additional magnets. It was discovered that as more magnets were added to a Halbach geometry, the higher field strength inside the bore came at the expense of a reduction in field homogeneity along the bore.

A number of different strategies were utilised to optimise the system. One of the most impactful changes to the system was the introduction of a copper box to provide RF shielding. Susceptibility matching was also incorporated where the magnetic susceptibility of the material the RF coil was wound around was matched as closely as possible to the susceptibility of the material surrounding the coil. This strategy provided a relatively small improvement to the fitted parameter when analysed in Prospa.

Polydimethylsiloxane (PDMS) oil was selected as an appropriate NMR fluid due to its long T_2^{eff} relaxation time and it was shown that the length of the oil's T_2^{eff} relaxation time decreases with an increase in viscocity. The mono-exponential relaxation parameter is an additional beneficial trait as automatic processing will be much easier when only having to deal with a single exponential co-efficient in calculating relaxation times. It was found that the smallest amount of PDMS that could reliably be measured was 125µL although 250µL provided a good balance between repeatability whilst still being a relatively small quantity of oil.

Magnetic nanoparticles with an avidin coating were immbolised to a small plate of polystyrene coated in biotin through an avidin-biotin (protein-ligand) interaction which was confirmed using confocal microscopy. Magnetic guidance was investigated briefly as a method of improving the binding coverage within the plates, but was found to not be a suitable technique for this specific binding strategy.

The nanoparticle coated polystyrene was placed into small wells rastered into acrylic test sticks where a small layer of oil (6µL – Depth of 250µm) was placed over the nanoparticles. A Carr-Purcel-Meiboom-Gill (CPMG) sequence was executed on the sticks placed inside the detection coil where the presence of magnetic nanoparticles caused a dephasing of the protons in the PDMS oil leading to a

shortening of the oil's T_2^{eff} relaxation time. This was observed for both the integral of 4096 echoes and a single echo. A reduction in echo intensity (amplitude) was also observed which, coupled with the mono-exponential relaxation parameters of PDMS oil, shows additional promise for the requirment of simple electronics to automate the measurement process.

T_1 measurement methods were also investigated but due to the lack of streptavidin coated gadolinium being commercially available it wasn't possible to create a binding strategy similar to experiments performed with iron oxide particles. Long scanning times with inversion recovery sequences also vastly increased the time it took to make a measurement making it an inferior method for rapid diagnosis. Overall, a cost-effective sensor was designed using a simple assay to detect the presence of magnetic nanoparticles.

CHAPTER 3: TRANSIENT EFFECT DETERMINATION OF SPIN-LATTICE (TEDSPIL) RELAXATION TIMES USING CONTINUOUS WAVE NMR

3.1. Introduction and Aims

As detailed in the previous chapter, a large number of commercial low-cost pulsed NMR systems are available, although for many applications these are still considerably more expensive than is feasible for numerous commercial sensor developments. In recent years, there has been a number of ultra-low-cost systems that have been discussed in the literature but unfortunately none of them have reached the stage of development which allows deployment in a commercial setting.

Despite being the original method of NMR experiments, Continuous Wave Nuclear Magnetic Resonance (CW-NMR) has been largely neglected for the last 50 years as the technology at the time provided relatively poor signal and significant effort in setup and tuning. When viewed in contrast to pulsed, Fourier transform experiments, the CW-NMR experiment is much simpler. A typical experiment involves sweeping the polarising field externally applied to the sample through the Larmor condition with a time varying magnetic field or frequency of irradiation, whilst monitoring the amount of RF energy absorbed. Investigating the absorption of the RF energy by the ensemble of magnetic moments provides information about their quantity and environment.

Today, CW-NMR is mostly consigned to undergraduate physics laboratories and is seen by many as a useful teaching aid in understanding magnetic resonance, given its comparative simplicity. Almost all of these experiments still employ oscilloscope detection, despite the prevalence of fast data capture hardware, capable of digitizing even the raw RF signals with minimal cost. In this chapter, a wide array of electronic hardware that has been used to undertake the continuous wave NMR experiment is discussed. The chapter considers how modern electronics are allowing the more basic of the NMR techniques to be used in a quantitative sense, in the hope that more scientists will consider CW-NMR for low-cost automated measurements of material properties.

3.2. Current Literature and Theory

3.2.7. Microcontroller Electronics

A microcontroller is a single Integrated Circuit (IC) that is typically used for a specific application and designed to implement certain tasks (Barrett and Pack, 2005). Sometimes referred to as an embedded controller or microcontroller unit (MCU), microcontrollers are used in products and devices that must be automatically controlled in certain situations. Appliances, power tools, medical devices, automobile engine control systems, and computers are a few examples of where microcontrollers can be used effectively.

The core feature of a microcontroller is that it can gather input, process this information, and output a certain action based on the information gathered. Microcontrollers operate at a relatively low speed of around 1-200 MHz and are often designed to have low power consumption as they are usually embedded inside other devices that can have a greater requirement for electrical power in other areas. In simple terms, a microcontroller can be compared to a small computer because it contains several essential components inside of it which are similar to that of a desktop PC motherboard. The microcontroller consists of a Central Processing Unit (CPU), Random-Access Memory (RAM), Flash Memory, Serial Bus Interface, Input/Output Ports (I/O Ports), and in many cases, an Electrical Erasable Programmable Read-Only Memory (EEPROM).

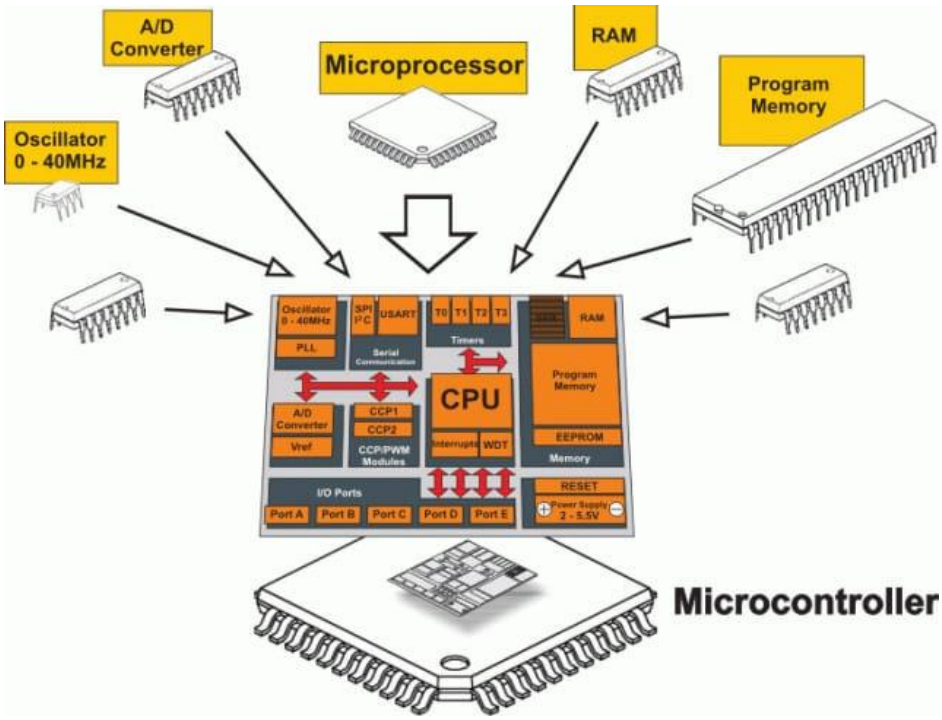

Figure 51: An example diagram of the different components located within a microcontroller system. (EFY Group, 2019)

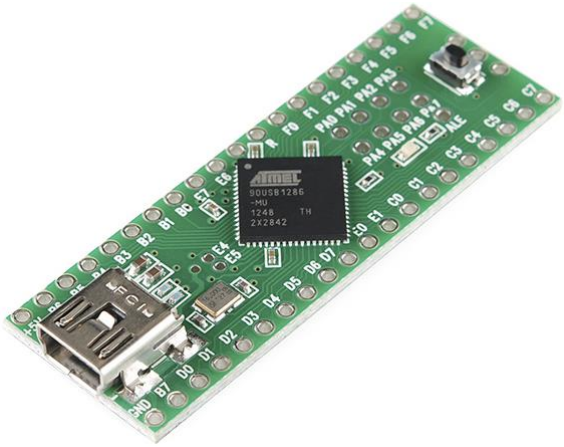

Figure 52: The Teensy-LC is an example of a fully assembled microcontroller unit. Its serial interface port allows programs to be loaded into its on-board program memory. (PJRC, 2019)

The function of each component can be briefly summarised as follows:

The most important component is the CPU which is often shortened to just 'processor'. This component is responsible for controlling each the instructions that it receives. Fundamentally it acts as the brain of the system, processing all the data input it receives, performing the required instructions it receives.

The RAM module is a component that temporarily stores data allowing it to be accessed quickly. It provides quick read-and-write access to the storage device. This differs from most other memories as it takes longer for data to be extracted since the data is not readily available. RAM is effectively like having access to the surface of data which is readily available, although anything that resides deeper will require a different type of memory. RAM improves total system performance because it allows the microcontroller to work with more information at the same time. Unfortunately, as RAM is temporary data, the data stored within it is lost if the microcontroller is ever switched off or reset.

Flash Memory is a type of non-volatile memory which, unlike RAM, retains its data for a certain period, even when the microcontroller loses power or is reset. This is particularly useful as this is where instructions that are uploaded to the microcontroller are stored so that the instructions do not need to be downloaded onto the device every time it is reset. Flash Memory writes to a single sector at a time. The diagram below shows how memory blocks are divided into pages and then into sectors. Writing or programming is performed at the page level and requires pages to be pre-erased. Once pre-erased, writing can be done an entire page at a time or by addressing a sector within a page that is empty.

Erasing is completed at the block level, and blocks wear out over time as memory cells break down after a number of erase cycles. When defective, blocks are considered bad.

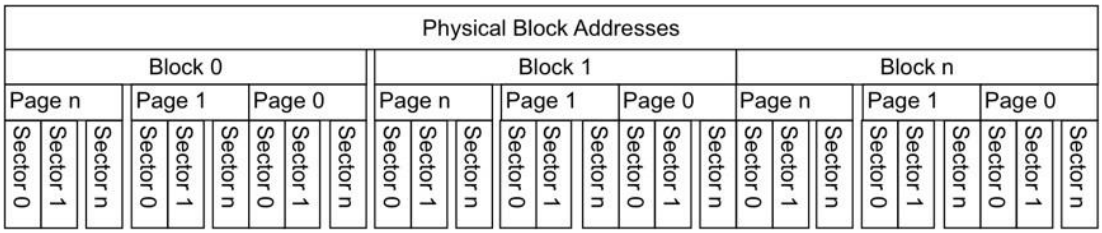

Figure 53: The organisational structure of Flash Memory

EEPROM is similar Flash Memory, except that while Flash Memory re-writes a block, EEPROM can re-write any specific byte at any time. This extends the life of EEPROM compared to Flash Memory but comes at the cost of being more expensive making them more suited to devices where longevity outweighs price.

The Serial Bus Interface is the serial communication in the microcontroller and is responsible for data transfer. Microcontroller components are often soldered onto printed circuit boards (PCB) and these components are connected via a series of signal traces on the board, sending information one bit at a time. For ICs, they use serial bus to transfer data to reduce the number of pins in a package to make them more cost effective.

I/O ports are what the microcontroller uses to connect to real-world applications. There are numerous inputs that the microcontroller can receive this way including temperature and motion sensing. This input is then sent to the CPU which decides what to do with that information. This information then produces a command based on the value of the input where it can be sent to output ports to perform tasks such as a simple blinking LED and even driving a motor.

3.2.8. Industrial Applications of NMR

In the early years of CW-NMR, numerous publications were submitted primarily to a series of food science and oil chemistry journals. The ability to differentiate between states of matter, particularly bound and unbound water, prompted many agricultural, industrial and food-based applications in CW-NMR.

The reasoning for this is due to a phenomenon known as motional narrowing. In an inhomogeneous medium, the magnetic field is variable causing the frequency of nuclear spin rotation to be different dependent on its position within the field which in turn produces a broadening of the linewidth.

However, if the atoms are diffusing around the system, they will sometimes experience a higher magnetic field than average and a lower magnetic field than average at other times. As a consequence, when detecting the resonant rotation frequency, the linewidth is narrower than it would be if the atoms were stationary. Some early examples in food science looked at these signals to evaluate the water content of foodstuffs such as apple and potato (Shaw and Elsken, 1956) and investigate the influence of temperature treatment on solid-liquid ratios of fats (Mertens and deMan, 1972; Oref, 1965).

An industrial example (Ladner and Stacey, 1962) is presented in an experiment where the proton signal in coal is first determined before water is added to the coal sample. After water had been added a sharper resonance peak is seen. Overlaying these two absorption signals it is possible to detect the presence of water inside the coal sample.

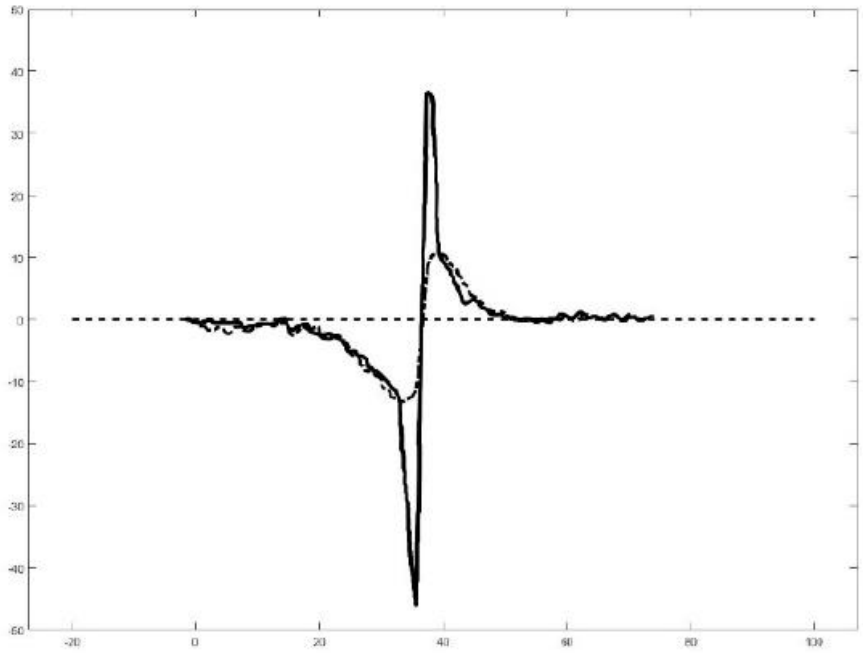

Figure 54: The overlaid absorption signals of dry coal (dashed line) and wetted coal (solid line). (Ladner and Stacey, 1962)

Many other liquid-to-solid ratio investigations followed this experiment. The amplitude of a wide-line peak associated to the profile of the hydrogen signal of fat was used to identify the fat content of chocolate (Oref, 1965), providing a measure that was more reliable than other methods used at the time (Pohle et al., 1965). Dynamic liquid-to-solid ratio experiments were also performed to offer insight into the rehydration of various food items boasting an ability to perform numerous non-destructive tests over a short period of time (Hall et al., 1967).

These experiments provided insight into the use CW-NMR for the evaluation of other dynamic processes. In one particular experiment, the oil content of corn

kernels is assessed using commercial instruments such as the Varian model PA7 analyser with an integrator (Conway, 1971).

Several commercial instruments, such as the Newport Wide-Line Nuclear Magnetic Resonance Analyser or quantity Analyser, were also developed to facilitate industrial measurements for some of these applications and for other material samples, although their use was and is still very limited.

3.3. Magnet Design

Commercial equipment capable of making NMR measurements with a continuous wave sweep is available. A particular kit supplied by LD Didactic GmbH consists of two electromagnets placed over an iron “U” shaped core. The electromagnet polarity is optimised in such a way that the coils mimic the geometry of a horseshoe magnet with a North and South Pole at either arm.

A laminated iron yoke is placed on top, to direct the magnetic flux through a solenoid coil sandwiched between the two yokes, which provides a homogenous and large magnetic field inside the solenoid.

The solenoid is connected to an NMR supply unit which together form the LC components of a marginal oscillator tank circuit. This NMR supply unit is fed into an oscilloscope where changes in the energy within the tank circuit from absorption during Larmor precession can be observed.

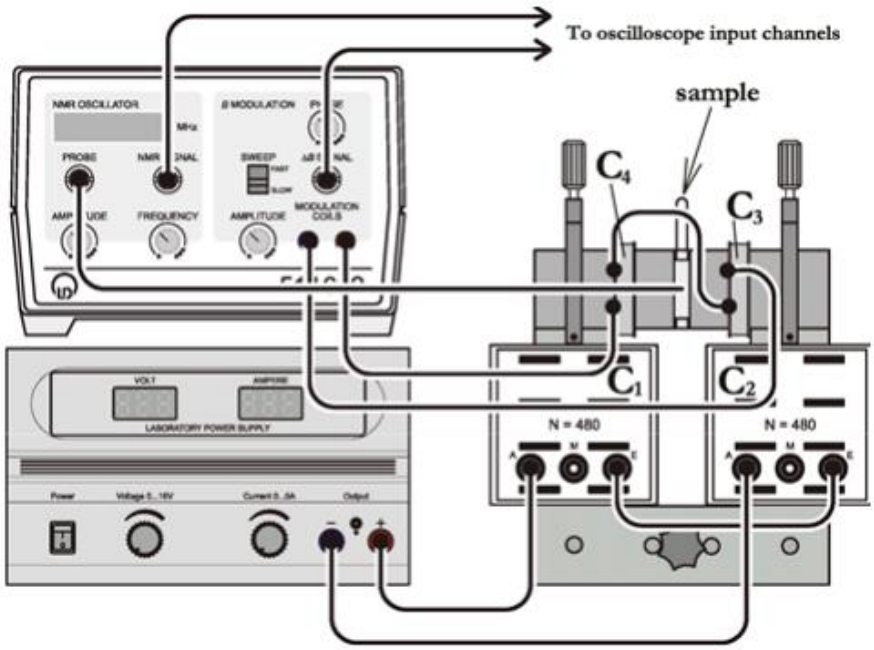

Figure 55: The experimental setup for a Leybold CWNMR device. The marginal oscillator unit houses all the major connections to the electromagnet including the RF circuitry and voltage supply for the sweep coils. The electromagnet is powered by a separate external power supply which can control the magnetic field strength by varying the supplied current. (LD Didactic, 2019)

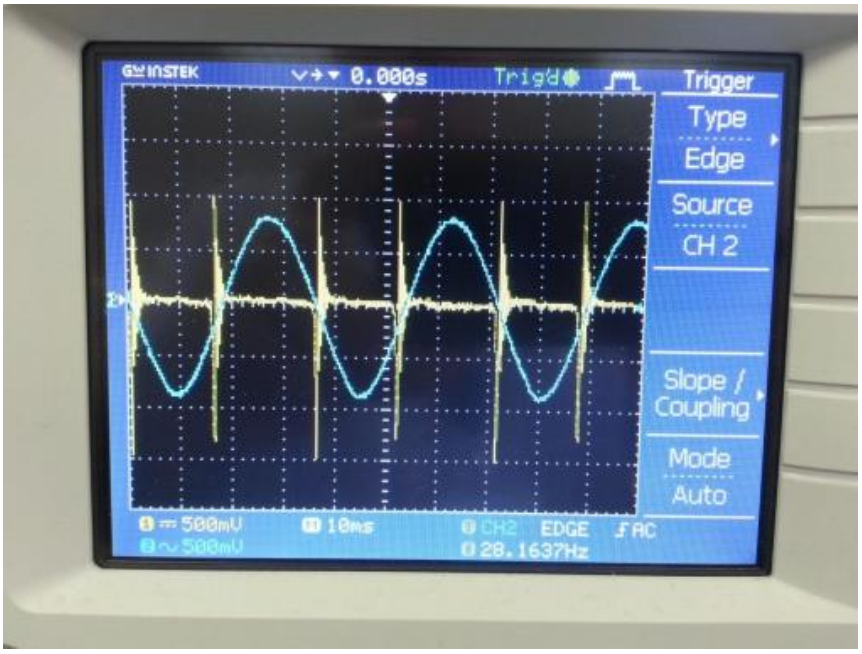

Figure 56: The NMR signal output read by an oscilloscope as a function of sweep voltage (blue) applied. As the sweep coils bring the external field into resonance with the frequency of the RF energy supplied to the coil, precession occurs causing a loss of energy in the tank circuit, which is demonstrated by an absorption curve (yellow).

3.3.1. System Optimisation

The Leybold system was designed to operate between 16.0 and 19.5 MHz by varying the current supplied to the electromagnet coils. The high current required to operate the magnet in that field range, however, causes significant heating of the samples during measurements affecting the value of T_1 and T_2. To overcome this heating, an additional 1 m of coaxial cable was installed between the sample coil and oscillator causing the oscillator to operate at around 12 MHz and requiring only a current of 2.2A to match the NMR frequency dictated by the static electromagnetic field.

This change reduced the temperature of the system from 38°C to 29°C, but as 29°C was still above room temperature, which was the storage temperature, the samples would still a be heated when placed into the probe, making it necessary to leave samples inside the solenoid coil to equilibrate to the surrounding environmental temperature adding additional time to sample measurements. Coupled with the high current draw required to generate a magnetic field strong enough to work at the frequency of the oscillator, this apparatus would be unsuitable for a portable device. As such, the electromagnets were replaced with two 25x25x25mm 0.5T NeFeB magnets (First4magnets, UK). The laminated iron core and solenoid were placed on top, to direct the flux as demonstrated before with the electromagnet setup. The result was a homogenous static field with a field strength corresponding to a Larmor frequency of 20.4MHz.

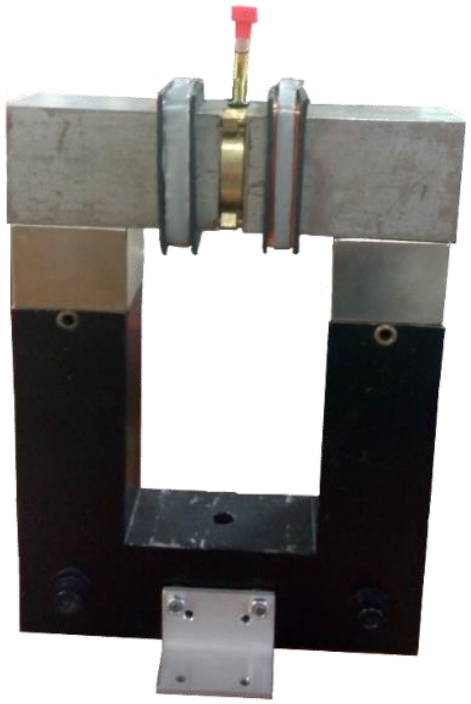

Figure 57: A cropped photograph of the static magnet sensor used in the CWNMR experiments. An NMR sensor from a Leybold experimental kit is mounted on two NdFeB magnets fixed onto an iron U-core.

3.3.2. Effect of Temperature on Magnetic Field Strength

As permanent magnets are subject to changes in magnetic field due to fluctuations in temperature, this is an issue that requires addressing. In a paper by Hughes-Riley et. al. (Hughes-Riley et al., 2016), the temperature dependence of a NdFeB magnet is reported to be 0.3mT/K.

As the voltage to the sweep coils can be modified to alter the range of magnetic modulation field, it must first be known how much the field changes as the voltage is varied.

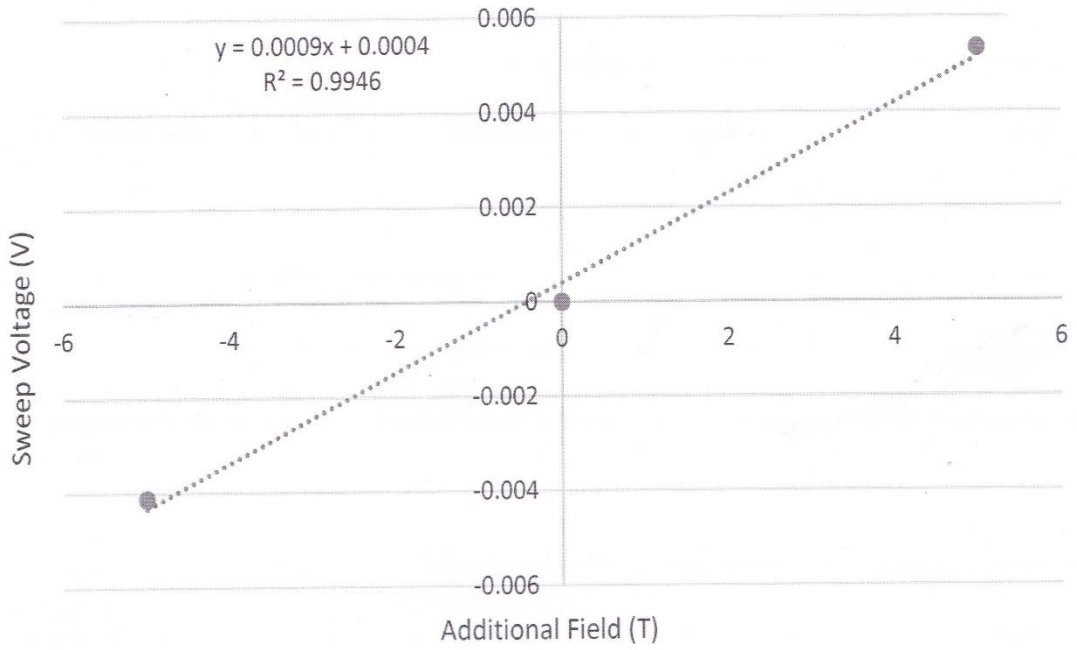

Figure 58: The effect of sweep voltage on the external magnetic field. Each volt applied to the sweep coils modifies the external field by 0.9mT.

As demonstrated above, a ±5V sweep provides ±4.5mT to the static magnetic field. Using the temperature dependence reported, this corresponds to a ±15K range. If the Leybold oscillator is tuned so that the absorption curve is in the middle of the sweep range, this means it would require a change in temperature of ±15K before the Larmor precession was no longer observable on the scope and the electronics would need retuning. This 15K tolerance should be more than enough to compensate for any natural fluctuations in room temperature.

3.4. LABVIEW Instrumentation

To develop a system that is capable of performing measurements similar to Look and Locker's experiments, a system must be designed that modifies the continuous sinusoidal modulation field applied by the Leybold Oscillator. The system must be able to read the data that is displayed on the oscilloscope and be able to identify the peak value in each sweep, so it can be analysed.

3.4.1. LABVIEW VI Design

Whilst the sensor composed of permanent magnets was being assembled, a simultaneous study was performed in choosing appropriate hardware and software to perform tone-burst measurements. Although the sweep coils would normally be powered by the NMR supply unit, the analogue output of a data acquisition card (NI USB-6211, National Instruments, TX, USA) was fed to a power amplifier built from a 2N3055H power transistor and LM358N buffer amplifier providing a gain of five. Data were collected by using the same data acquisition device operating at 500 kS/s integrated with a LabVIEW program to generate appropriate waveforms and collect the resulting NMR signal. The analogue output of the USB-6211 produced a saw-tooth voltage waveform of maximum amplitude 1.25 V and a frequency of 50 Hz in 5-s bursts with a recovery time delay between bursts. The inner workings of the LabView VI's are demonstrated below.

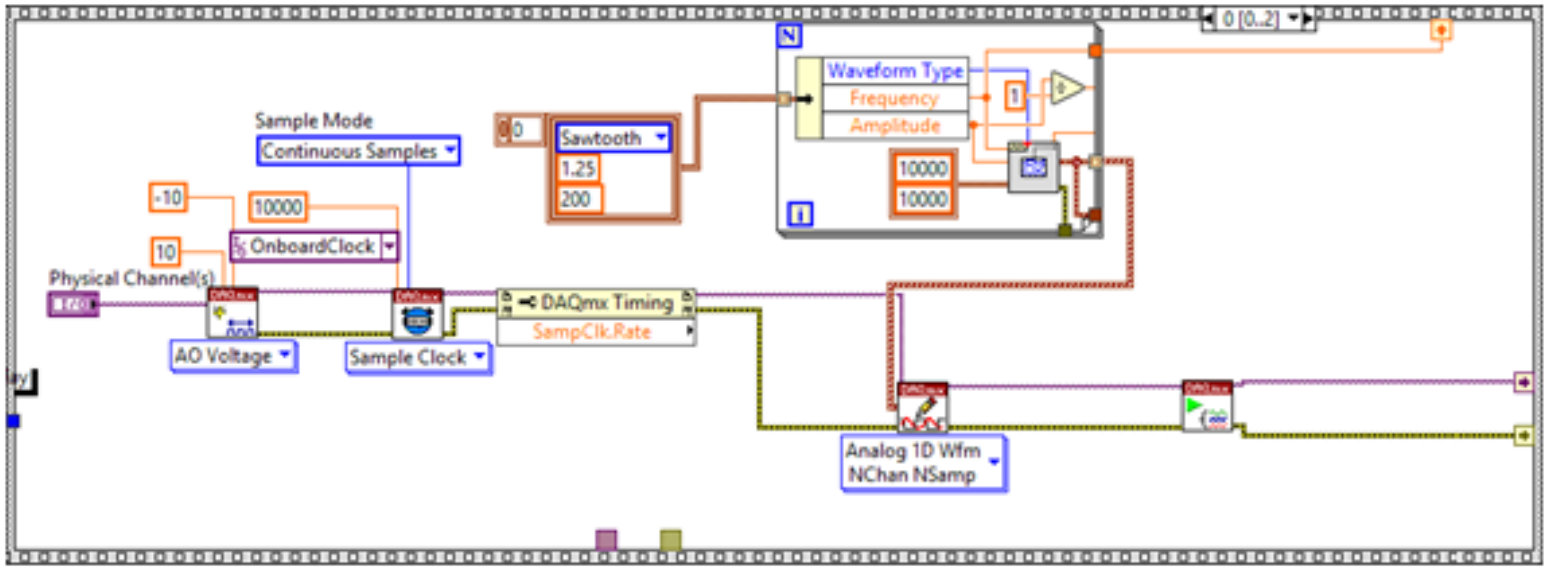

Figure 59: The first page of the LabVIEW VI. This section governs the sweep voltage. Through these settings, the frequency, amplitude and shape of the output waveform can be modified, as well as the sample rate.

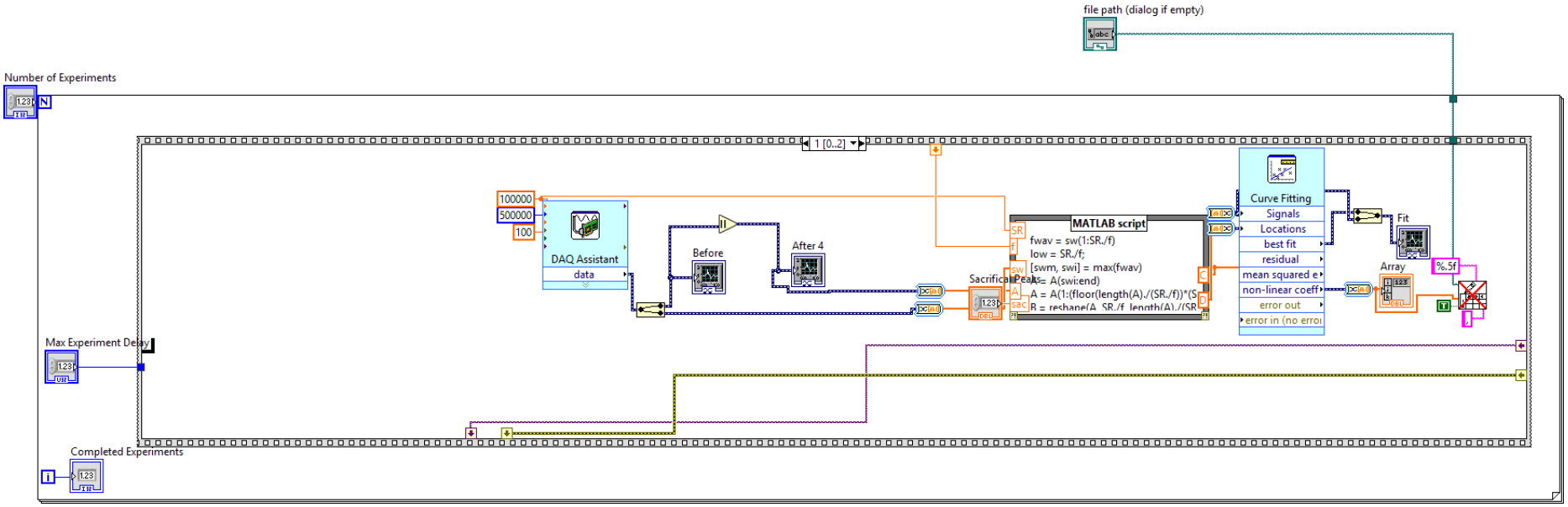

Figure 60: The second page of the LabVIEW VI. This section governs the peak detection for successive measurements and the curve fitting before printing the data to the front panel of the VI.

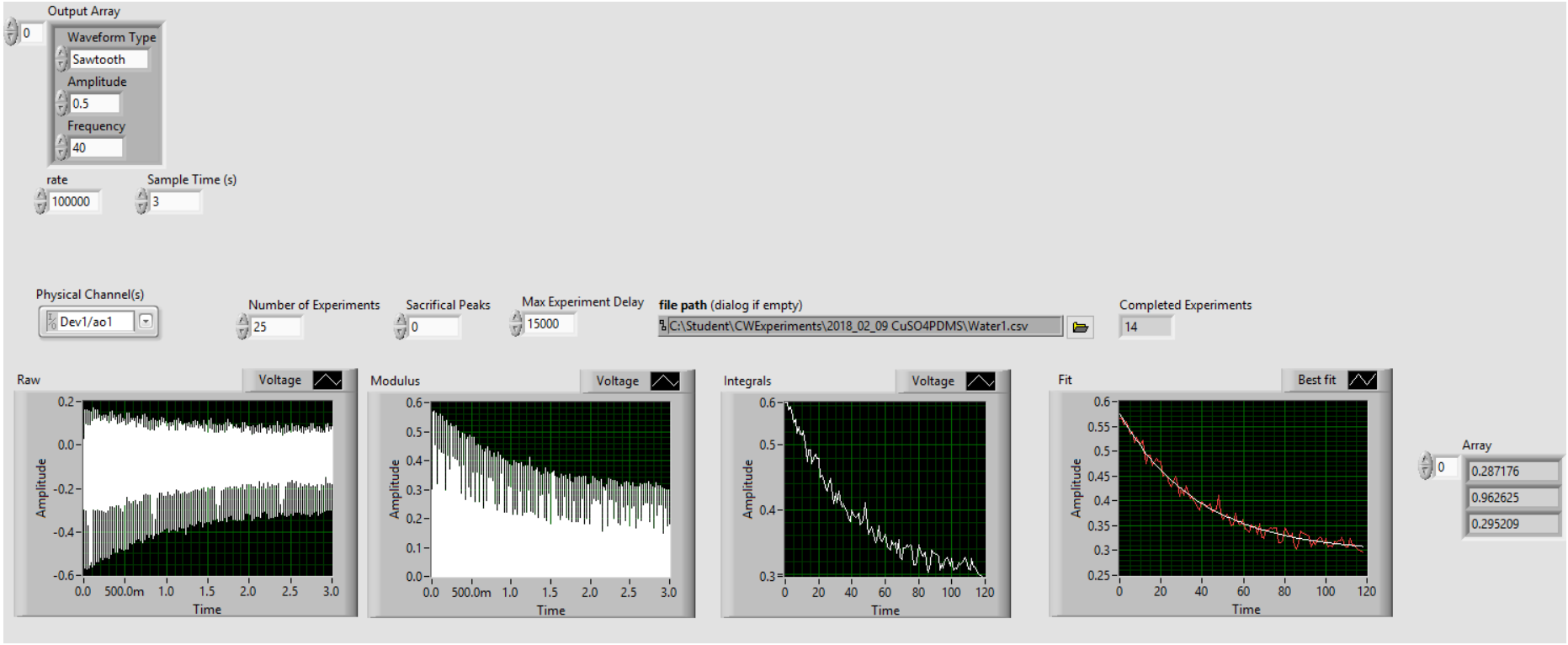

Figure 61: The front panel of the LABVIEW VI. Array values are printed in a table as well as graphical views of each individual stage of data capture, peak plotting and exponential fit plotting.

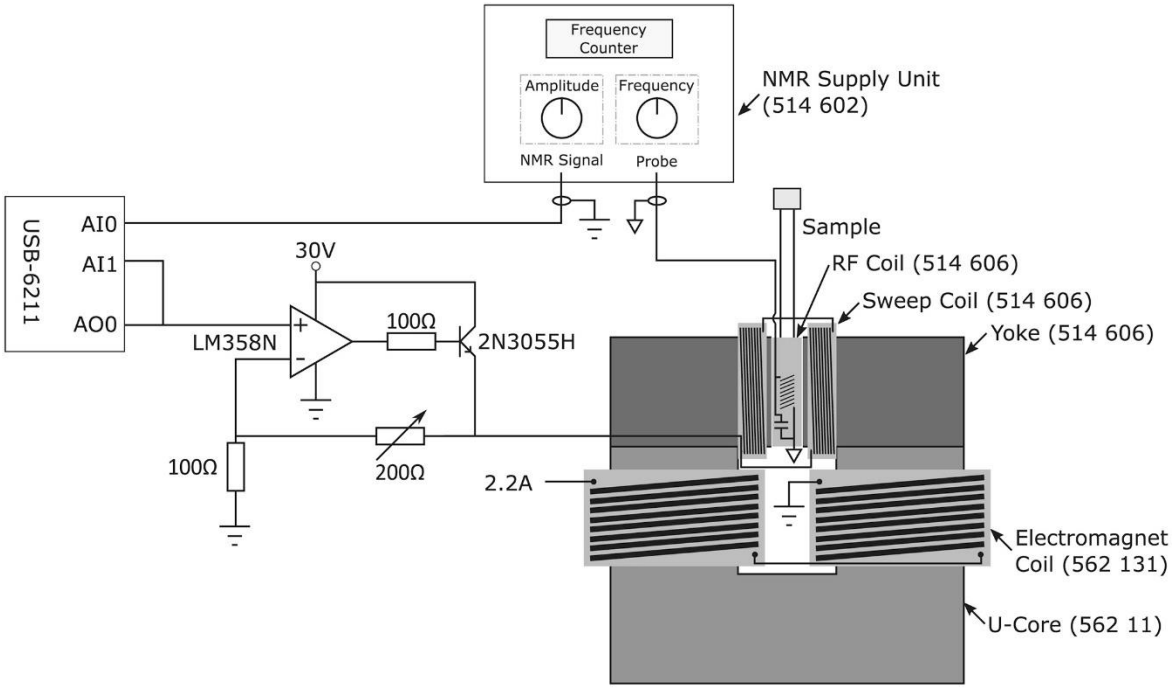

Figure 62: The modified CWNMR experiment. Instead of powering the sweep coils with the NMR supply unit, the analogue output (AO0) of the National Instruments Card (USB-6211) is fed to a power amplifier built from a 2N3055H power transistor and LM358N buffer. This provides a greater control over the waveforms that can be fed into the sweep coils as the NMR supply unit can only provide sinusoidal waveforms.

3.4.2. LABVIEW Measurements

The NMR signal for a single sweep is demonstrated below, with the main peak followed by the characteristic 'wiggles' and a subsequent smaller peak on the fly-back of the saw-tooth wave applied to the sweep coils. The Labview VI software produces the modulus of the data before finding the maximum value within each sweep. An example of the result of this process is also shown below where a curve fitting routine in performs an exponential fit before writing out the exponential coefficients [amplitude, decay time (T_x) and noise] to a file. Before repeating the experiment, the system must be allowed to re-equilibrate. The time allowed for this to take place is known as the recovery time. The minimum recovery time required to achieve a reliable exponential fit was determined experimentally by measuring a 100µM aqueous copper sulphate solution 50 times for recovery times from 1 to 50s. The standard deviation in the exponential fit was high for the short recovery times but

reduced rapidly as the time was increased. The plateau was found at 15s. To allow for a safe margin of error, 20s was chosen for use in all subsequent measurements.

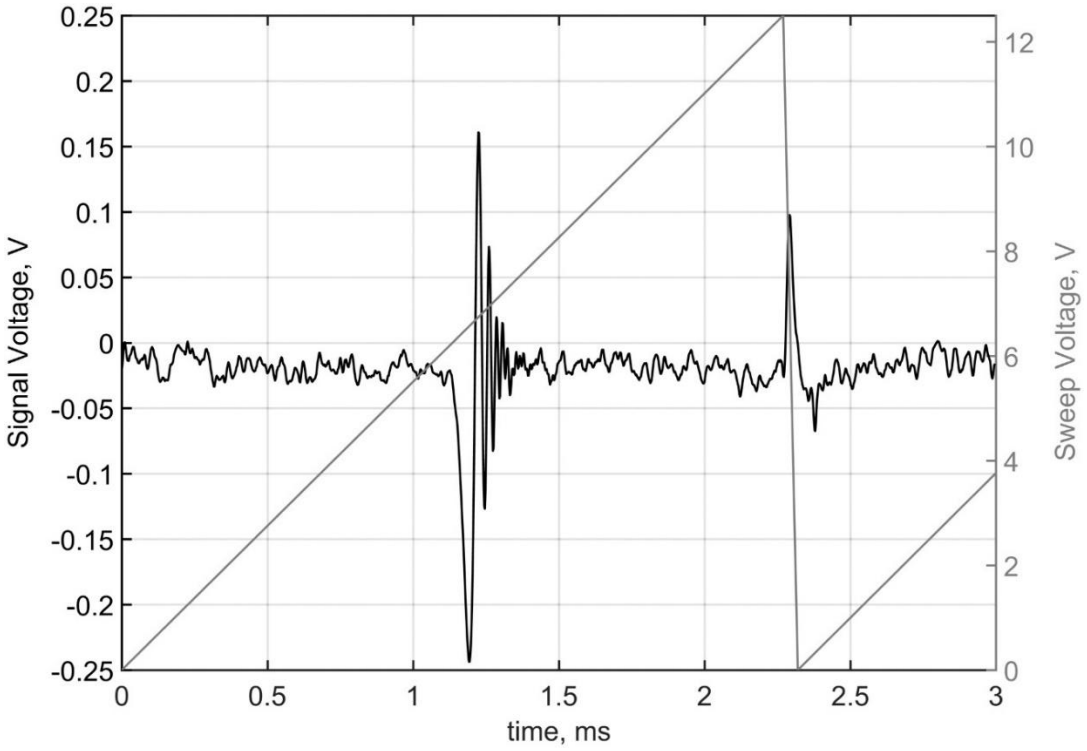

Figure 63: The NMR output signal (Left axis, Black) for a single sweep of the saw-tooth waveform (Right axis, Grey) applied to the sweep coils. An additional smaller peak is also seen as a result of the fly-back.

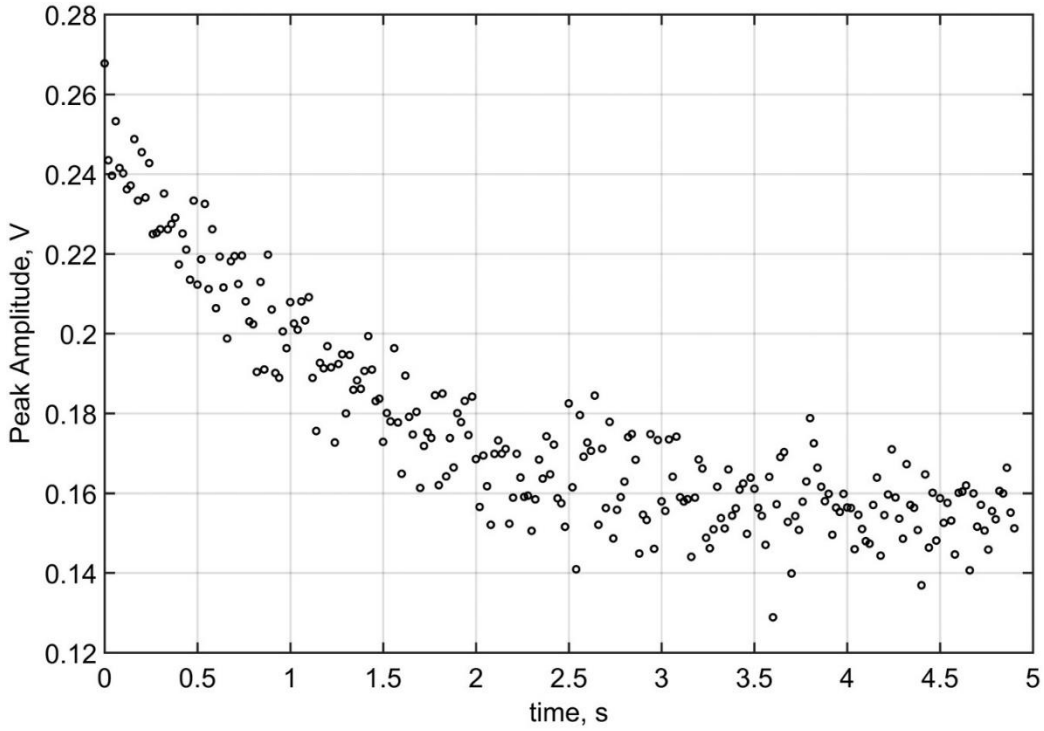

Figure 64: The peak amplitude of the NMR signal for each sweep of the saw-tooth shown for a five second burst. The LabVIEW VI software creates an exponential fit to the data to provide the characteristic time referred to as T_x.

The samples used consisted of a range of polydimethylsiloxane oils of different viscosities, from 2 to 30,000cSt, and a variety of different concentrations of copper sulphate solutions, ranging from 5 to 750 µM, giving T_1 values in the range of 0.5 to 2 s. The T_1 values were measured on the same electromagnet setup and RF coil, with additional tuning and matching capacitors, using a pulsed NMR spectrometer (Kea^2, Magritek, NZ) running an inversion recovery pulse sequence with Carr–Purcell–Meiboom–Gill echo detection. Below, the T_1 relaxation time as measured by the pulsed system plotted against the exponential fit decay time from the CW-MR data is demonstrated.

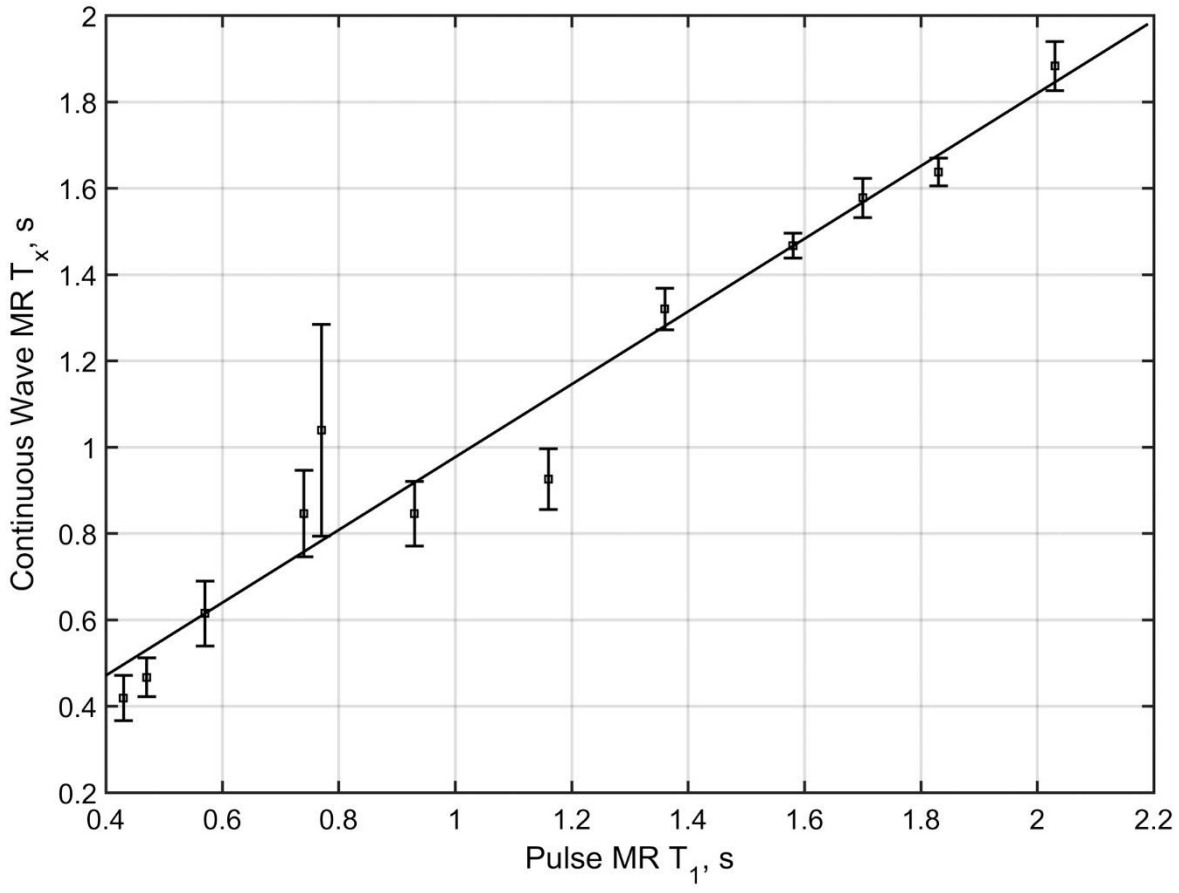

Figure 65: The value of T_x plotted against the value of T_1 determined through pulsed NMR.

While some scatter can be seen, there is a clear linear correlation between the two. It should be noted that the T_x value we determine is not the same as the value of T_1 in seconds. There are several parameters which change the gradient of this relationship including the amplitude setting of the oscillator. In these experiments, a central 'sweet spot' was used, where all the samples presented a sustained oscillation without changing the amplitude setting. As the relationship between T_1 and T_x is linear, unknown measurements are easily collapsed to a gradient of 1 by using two reference samples (one high and one low T_1 values) to provide the calibration factor.

3.5. Microcontroller Instrumentation

LABVIEW has been demonstrated to be a useful piece of software for automating a lot of the controls and processes involved in performing CW-NMR experiments. Unfortunately, the software still requires the use of a desktop/laptop computer which has a considerable power draw making it much less desirable in portable applications. As discussed previously,

there are a number of microcontrollers available that are viable for a number of different activities. Most importantly, the Teensy 3.5/3.6 microcontrollers contain built-in analogue and digital converters which are invaluable for signal generation and recording (PJRC, 2019). These microcontrollers will be investigated for use in a system to automate the TEDSpiL experiment, providing a system that will have a considerably smaller footprint and power draw in the aim of developing a portable system.

3.5.1. Design of Microcontroller System

A digital to analogue converter on a teensy 3.5 microcontroller was used to generate a ramp voltage which was amplified, using a power amplifier built from a 2N3055H power transistor and LM 358N buffer amplifier (providing a gain of five), before driving the sweep coils. The ramp was started using a push button attached to a digital input (pin 12) on the Teensy 3.5 microcontroller and a digital output (pin 11) was used to trigger a Teensy 3.6 to make measurements of the marginal oscillator output after it had been amplified by a simple inverting op-amp (MCP6002) with 1kΩ input resistor and 10 kΩ feedback resistor giving a gain of -10.

The Teensy 3.6 is a 32-bit 180 MHz ARM Cortex-M4 processor with floating point unit, 256 kbytes of RAM and 1024 kbytes of flash memory including an on-board μSD card holder and under US$30. It contains two ADCs with a usable resolution of 13 bits.

For maximum speed, data is saved into an array in memory and the maximum array size for 16bit sample data is around 64000 data points. This is not enough to capture the whole of the data for 60 sweeps at 40Hz and a lower sample rate may not clearly identify the peak value. To overcome this limitation, a Teensy 3.5 was used to provide a trigger pulse to the Teensy 3.6 part way up the ramp sweep so that only the points around the peak were captured to an array in memory. This was finalised by coding a straightforward loop to find the maximum value within that data to give the peak value which was stored in a separate array of peak values. It should be noted that the Teensy 3.6, unlike the 3.5, is not 5V tolerant so the amplifier is supplied with only 3V from two 1.5V batteries and both the Teensy 3.5 and 3.6 are supplied with 4.5V from three 1.5 volt batteries. In this circuit, both amplifier and Teensy shared batteries and the amplifier supply was ‘tapped’ off, using only two of the three batteries.

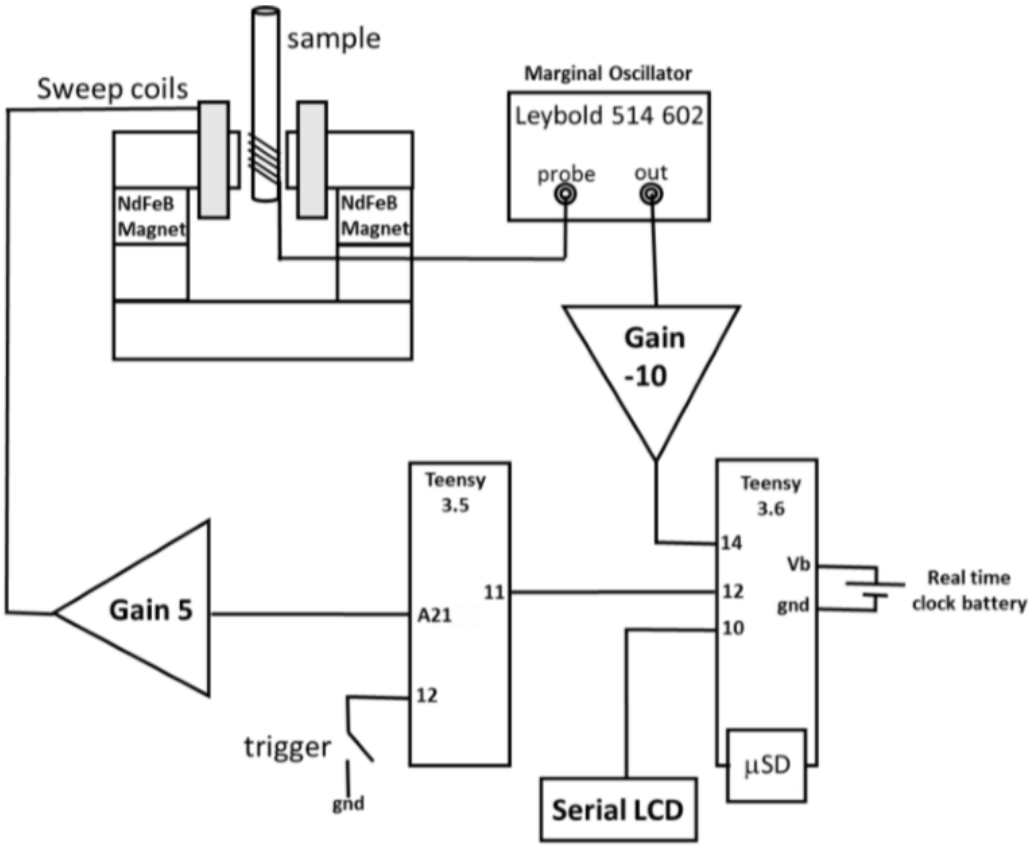

Figure 66: Schematic diagram of the experimental arrangement. Power (4.5V to Vin) and ground (Ground to GND and Analog GND) have been omitted from the diagram. An inverting op-amp is used to provide the gain of -10.

3.5.2. Software Development of Teensy 3.6

To begin with, open source software was acquired (Stoffregen, 2019). Much of the material for the Teensy has been developed open source by Paul Stoffregen and his team at pjrc.com however there is an implementation library for the ADC created by Pedro Villanueva which allows the full power of the ADC to be utilized (Villanueva, 2019). This code was used as the starting point in which to develop the software for use with the CW-NMR setup and is identifiable as “Teensy 3.6 starting code” in Appendix A.

The basic functionality of the code allows the Teensy 3.6 microcontroller to wait in an idle state until trigger by a high voltage received at one of the pins. Upon receiving this external signal, the ADC is utilised to read the voltage supplied to it over time and save this data to an array. This process is repeated for multiple sweeps of the modulation field before calculating the peak value from each sweep and printing them to a file in the on-board SD

card and also printing them to serial. A small delay is placed into the loop to ensure the spins have time to reset to thermal equilibrium away from the resonant value of the magnetic field.

To calculate the value of T_x, the saved data file must be opened in a spreadsheet, such as Excel, and plotted graphically so that an appropriate fit may be assigned to it. Plotting an exponential fit to the data and extracting the gradient value from the equation $y=\exp(mx)+c$, provided a value for T_x.

An example flowchart of the processes performed by the Teensy microcontroller system is shown below.

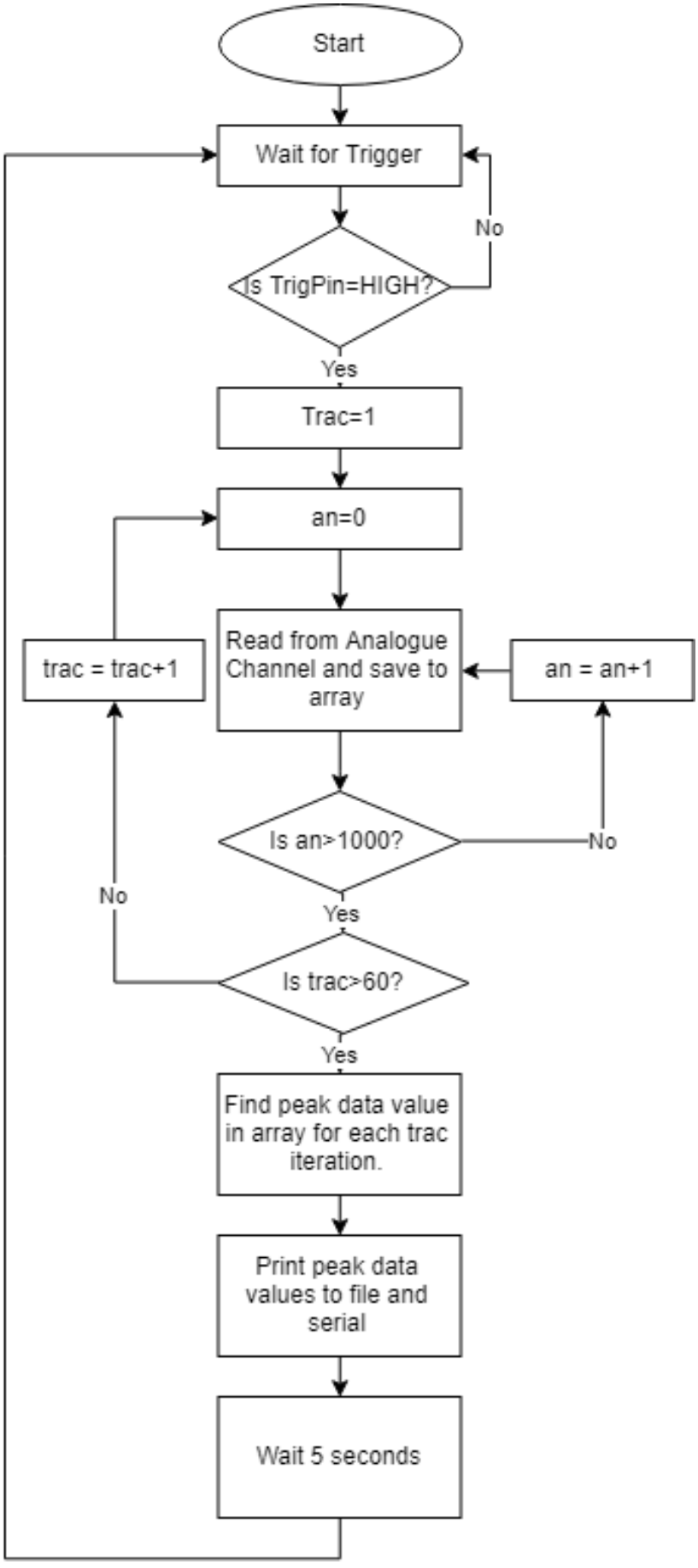
Start
Wait for Trigger
Is TrigPin=HIGH?
No
Yes
Trac=1
an=0
Read from Analogue Channel and save to array
trac = trac+1
an = an+1
Is an>1000?
No
Yes
No
Is trac>60?
Yes
Find peak data value in array for each trac iteration.
Print peak data values to file and serial
Wait 5 seconds

To begin, a brief investigation into the ADC settings was performed. There are two settings that can be modified which are “setConversionSpeed” and “setSamplingSpeed” which change the speed of the analogue to digital conversion and the sample rate respectively. These speeds could be set to ‘low’, ‘med’, ‘high’ and ‘high16’ and the combination of the two settings provide an overall sample speed as demonstrated in the table below.

bits	Sample mode	Conversion mode	speed
8	low	low	100kS/s
8	high	high	300kS/s
16	low	low	80kS/s
16	low	med	140kS/s
16	low	high16	140kS/s
16	med	high16	150kS/s
16	high	high16	160kS/s

A 10 kHz sine wave was fed into the Teensy microcontroller at pin 14 and the voltage values read were printed via serial. The settings were changed for a range of combinations of the 4 speeds, until a reliable sample was observed through setting both setConversionSpeed and setSamplingSpeed to ‘high’.

The next step in developing the code was to investigate the repeatability of the measurements. If the readings were not consistent, the value of T_x reported would be subject to too high an error which would compromise the reliability of any readings.

A sample of water was placed into the CW-NMR sensor and readings of peak amplitude over time was taken on 10 separate occasions, over the course of 10 minutes ensuring measurement parameters were unchanged.

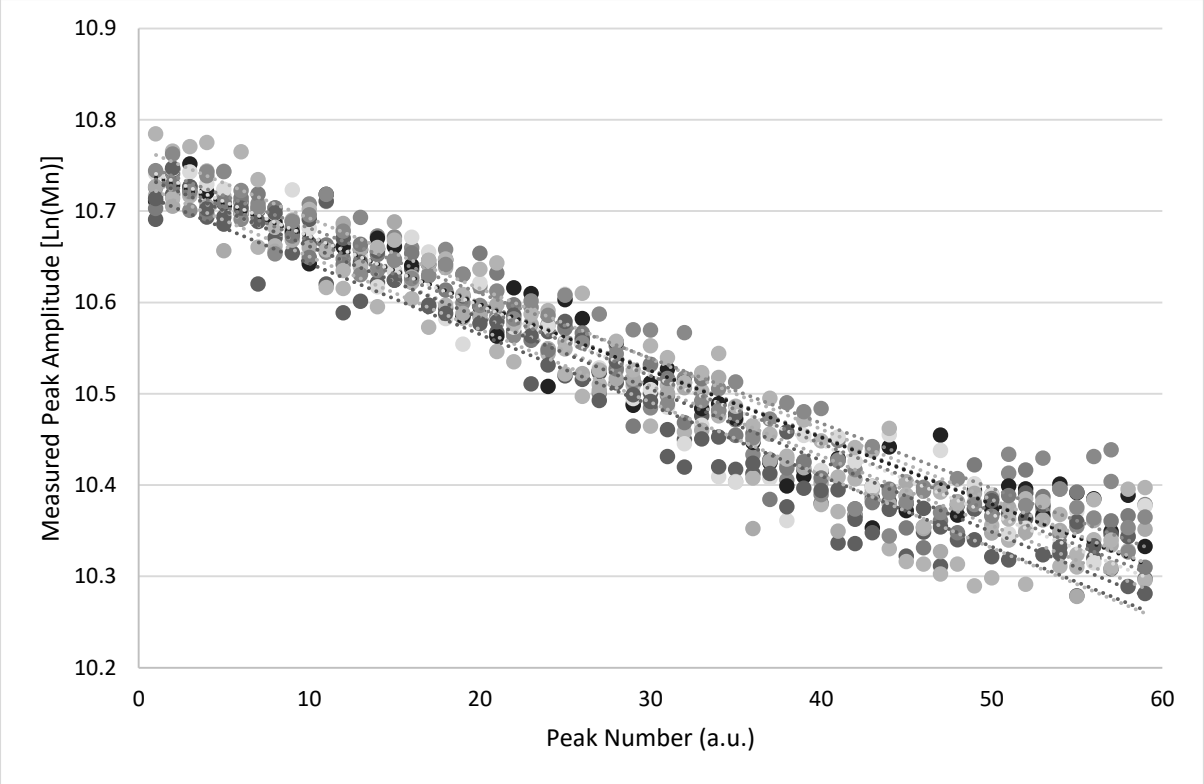

Figure 67: The reliability of multiple measurements using the teensy microcontroller system. As seen, there is a very small variance in successive experiments and the gradient of each fit is consistent to within 4%.

The result of this quick investigation provides an average reading for the T_x of water to be 76±3, corresponding to only a 4% variance in the measurements. This small variation was taken to prove the repeatability of multiple measurements performed in short, 2 second time frames.

The effect on acquisition time was also investigated. As on-board memory is limited, storing large arrays of data can limit the functionality of the system for performing additional processes. Adjusting the value of 'trac' in the getData() loop, provides control over the amount of time the ADC is recording and storing recorded values. A sample of water was placed in the CW-NMR setup and a series of modifications were made to control the acquisition time. Repeat measurements were made and a value of T_x was calculated for each experiment allowing successive readings of T_x to be compared to each other and check for reliability in the measurements.

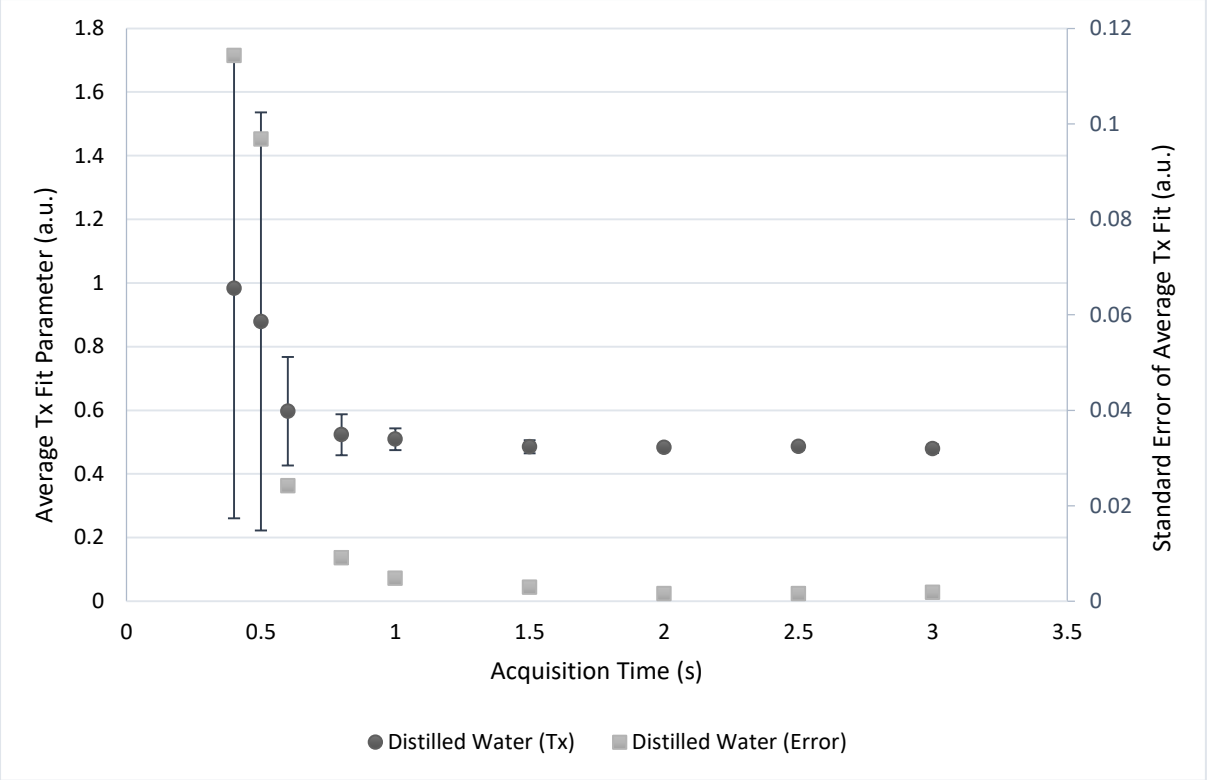

Figure 68: A comparison of the reliability of a T_x fit on a sample of water for different acquisition times. Under one second, there is a considerable standard error associated with repeat measurements. Above one second, the reduction in standard error becomes negligible, not warranting the use of additional RAM.

When the acquisition time was too low (<1s), there is a huge discrepancy in successive measurements. Above one second, the error associated with repeat measurements is drastically reduced. It was decided that a 1s acquisition time provided the best balance between reliable result and minimising the amount of memory required for these processes. The requirement for external graphical software to calculate T_x was an unnecessary addition to the measurement electronics as the mathematical operations could be performed on the microcontrollers. A simple linear regression algorithm was written into the code to calculate the T_x where the value could be printed via serial.

To calculate the exponential decay factor of curve, the peak values were logged and transferred to a new array called “locker”. A series of mathematical calculations are performed on the array of logged data values in order to produce a value for the gradient and intercept for a line of best fit drawn to the data set. The values produced from the

linear regression algorithm were compared to those calculated using graphical software and were found to be the same.

While the microcontroller was only printing to serial and saving to data files, the requirement of a PC was still prevalent. To remove this from the functionality of the device an LCD screen was purchased for the data to be displayed on.

In order to present the data on the LCD a few lines of extra code had to be written into the Teensy 3.6. Firstly, the serial port requires identification and initialisation. Using the SoftwareSerial command, pin 10 on the teensy was assigned the name “mySerial” allowing mySerial.begin to start up the port.

Using mySerial.write(), the cursor can be moved, and text strings can be sent to the LCD to be displayed on the screen.

Finally, this was modified slightly to ensure that the readings of T_x provided were reliable and not a result of noise.

The purpose of this code is to perform a quick check that the successive peak values are progressively smaller than each other. A reliable TEDSpiL measurement follows an exponential curve in which the value of peak value consistently decreases. If a sample is not present, then the signal measured is the result of background noise and will not fulfil the condition instead printing “no TEDSpil” instead of giving a value. This also provides some protection against unpredictable spikes in voltage that may be read by the ADC.

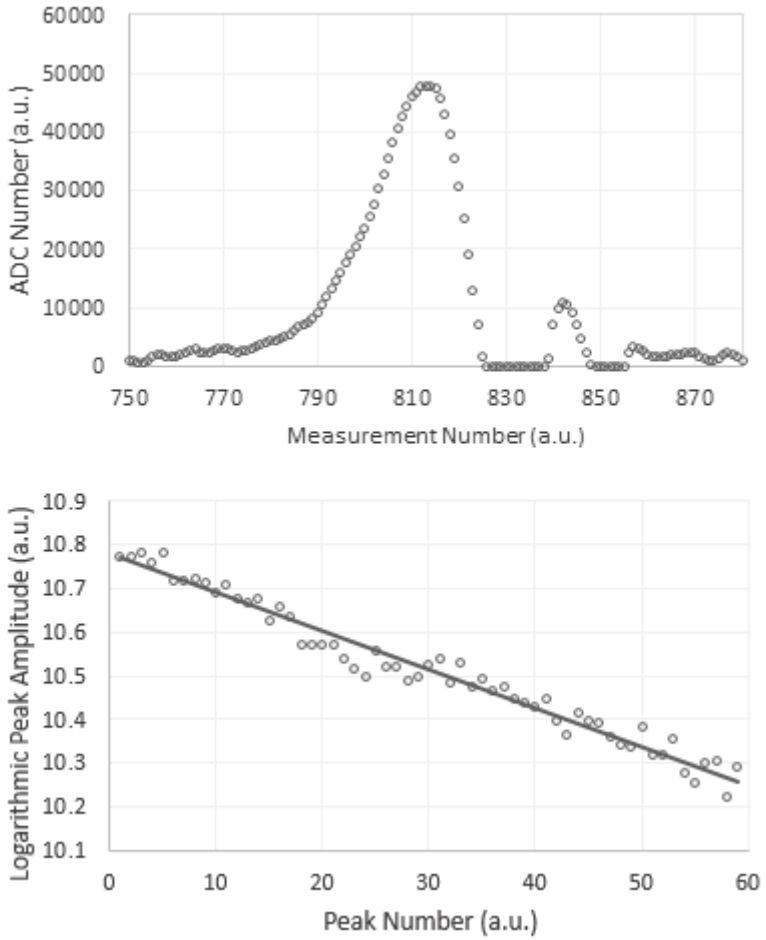

Figure 69: (above) The ADC values returned from the Teensy 3.6 for a linear sweep through resonance. (bottom) An example of the logarithmic peak values of water returned from the peak value array with a least squares fit. The gradient of the linear fit provides the numerical value to the parameter T_x.

3.5.3. Software Development of Teensy 3.5

A Teensy 3.5 was incorporated into the design to handle both the ramp voltage to the sweep coils and to send the trigger pulse to the Teensy 3.6. The code for this is identifiable in Appendix A as “Teensy 3.5 Code”. A few basic experiments were performed to assist in understanding the nature of how the internal delay affected the sweep rate and where the trigger was located in the sweep cycle.

Using an oscilloscope, the voltage was measured at pin 11 and analogue pin 21 as the value of ‘n’ was changed when the output was set to high.

Increasing the time that the output was high in the loop increases the amount of time the teensy 3.5 was sending a trigger to the 3.6 to start data acquisition. Similarly, changing the

starting value of n, changes the location within the sweep that the data acquisition of the 3.6 will begin.

Within the loop are two delays which can be modified to change the sweep rate. A smaller delay will lead to the loop being complete faster, leading to a faster sweep rate. Conversely, increasing the delay will slow the sweep rate, but increasing it too much will lead to a more step-like nature to the ramp voltage

3.6. Further Microcontroller TEDSpiL

As a working microcontroller system that could perform the same processes as the LABVIEW VI was fully operational, it was time to perform a series of experiments to observe if this new system and its value for T_x was still capable of providing a measure for T_1 relaxation times in a series of different samples.

3.6.1. Suspended Gadolinium

Gadolinium salt (DTPA-bis(stearylamide) (gadolinium salt), Sigma Aldrich) was mixed with lab grade methanol to varying concentrations and placed into standard NMR tubes. These samples were placed into the CW-NMR setup connected to the microcontroller system where TEDSpiL experiments were performed to measure T_x.

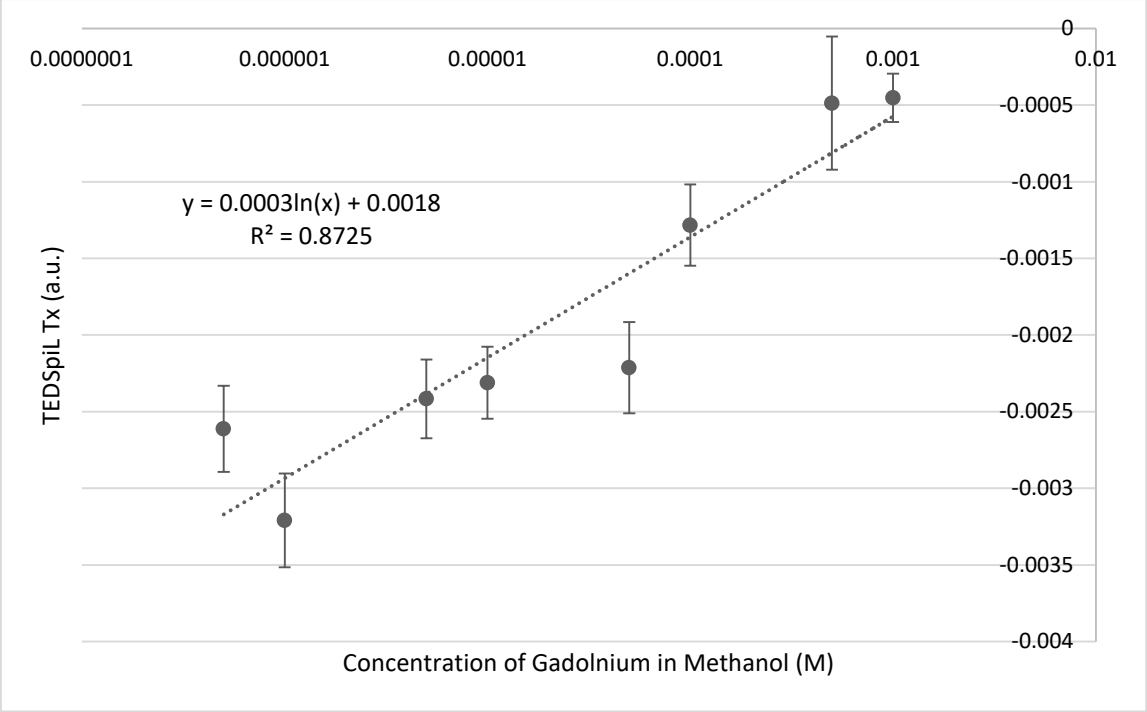

Figure 70: Continuous wave T_x parameter as function of the concentration of gadolinium dissolved in methanol. An increase of gadolinium leads to a reduction in the measured T_x.

As discussed in the previous chapter, an increase in the concentration of gadolinium leads to a reduction in the T_1 of surrounding protons. A similar trend is seen in the value of T_x when using the microcontroller system.

3.6.2. Relaxation Effects from $CuSO_4$

As $CuSO_4$ was used extensively for TEDSpiL when making measurements with the LABVIEW system, it was also investigated in the microcontroller system. Solutions of $CuSO_4$ were prepared through mixing copper sulphate powder with distilled water. This time, T_x was measured with the microcontroller system before switching the system out for a KEA^2 spectrometer and with interconnecting tuning/matching circuitry to perform inversion recovery sequences within Prospa, allowing a measurement of T_1. The pulsed T_1 time was compared to the CW T_x time graphically to check for a similar trend to that experienced with the LABVIEW experiments.

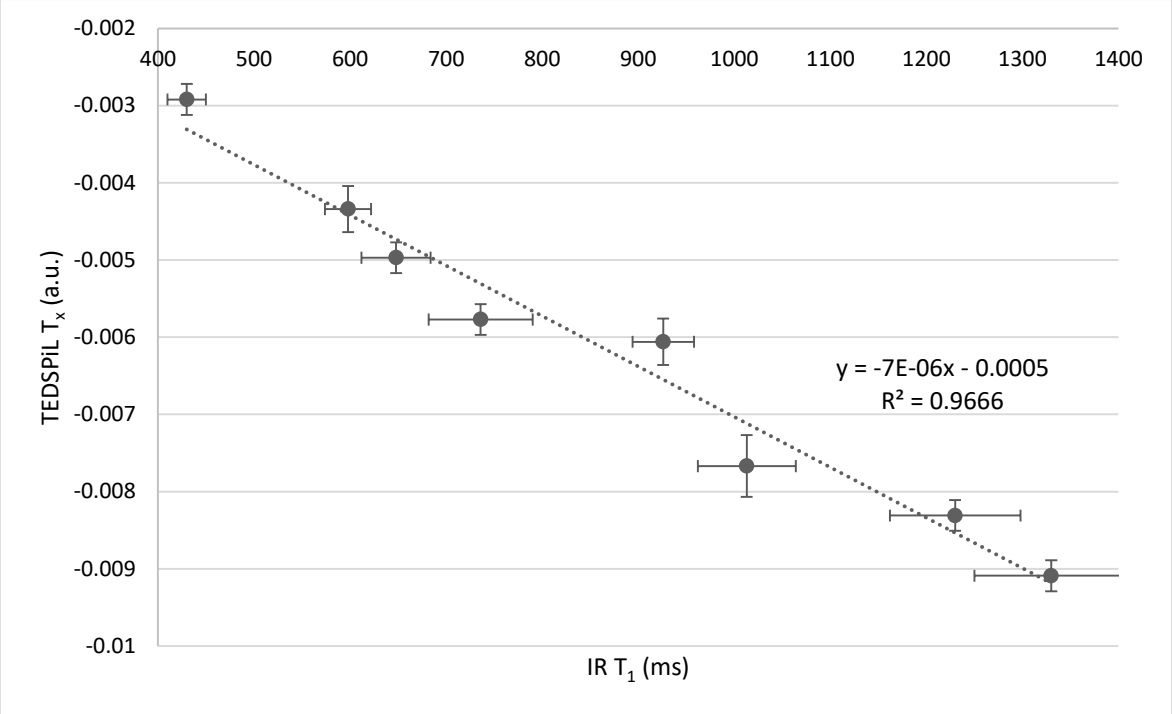

Figure 71: Continuous wave T_x parameter as function of the concentration of CuSO4 dissolved in water. An increase of $CuSO_4$ leads to a reduction in the measured T_x.

An increase in the concentration of the $CuSO_4$ leads to a reduction in the T_1 relaxation time, but also in the measured T_x. The fit appears to be accurate, demonstrating the ability for the microcontroller system to rapidly detect changes in T_1. It is also important to note that each T_x measurement was performed in 5 seconds, which is stark in comparison to the inversion recovery requiring upwards of 6 minutes to provide enough data points to plot a reliable enough fit to derive T_1 from.

3.7. CW-MaRDi

The TEDSpiL technique has been shown to be capable of measuring T_1 values for a range of different fluids. Originally performed with LABVIEW and desktop PC, a microcontroller system complete with LCD screen and self-contained power source has been developed to provide a portable device capable of performing T_x measurements that can be used to measure T_1 using a few calibration sources of known T_1. As all of these techniques have been performed using liquids of varying viscosities or paramagnetic material in solution, it was decided that a revisit to earlier immobilisation methods was required to see if it was possible to incorporate this new design into the assay designs constructed in chapter 2.

3.7.1. SPIO Assay Designs for CW

Due to the geometry of the permanent magnet designed for the microcontroller, the following setup was designed. Avidin coated MNP was bound to biotin coated well plates in the same manner as performed in earlier experiments. These MNP immobilised plates were cut to an appropriate shape, filed down to thin them and affixed to a thin wooden stick so that they could be inserted into a small volume of PDMS. As these plates reach the PDMS, it is displaced to create a thin layer of NMR capable fluid surrounding the MNP. This was placed within the RF coil and measurements of T_x, T_1 and T_2^{eff} were made on the MNP coated plates and also a control consisting of similar affixed plates without bound MNP. T_x measurements were made using the microcontroller system, while the T_1 and T_2^{eff} measurements were made by disconnecting the magnet and RF coil, and connecting it to a KEA^2 spectrometer with interconnecting tuning/matching circuitry and performing an inversion recovery and CPMG sequence respectively.

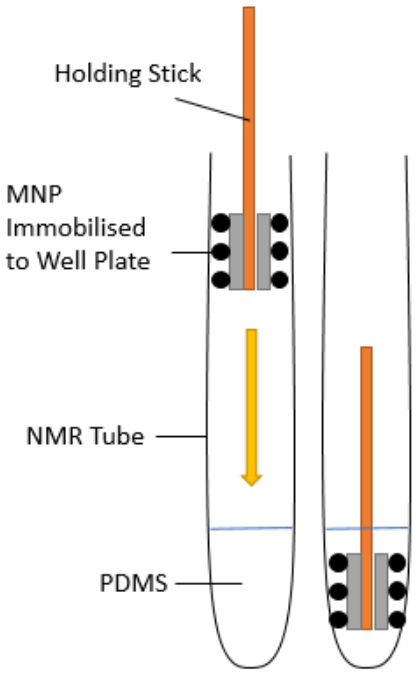

Figure 72: A diagram of an experiment utilising MNP immobilised to a well plate, fixed to supporting structure before being inserted into an NMR tube filled with a small amount of PDMS.

The T_x values reported for the control in this setup was -0.008±0.001 whereas when the MNP coated plates were used, the T_x changed to only -0.006±0.001. The T_1 time for the control was reported as 1070±40ms compared to the presence of MNP which lowered the T_1 time only marginally to 910±80ms. T_2 of the control was reported as 620±10ms compared to the MNP loaded plates lowering the T_2 time to 590±10ms.

As these changes are very small, it was assumed that the amount of MNP in comparison to the amount of PDMS was too small to be providing noticeable changes in relaxation times. This issue was overcome with a new setup in which 1ml of 10mg/ml 100nm Iron Oxide nanoparticles was applied to cotton paper and left it dry. The paper absorbs the nanoparticle solution into itself providing a binding method, albeit with a much lower binding affinity as there are no protein-ligand bonds present in this technique. The cotton paper soaked with MNP was added to an NMR tube and filled with water. The position of the tube inside the NMR coil was modified to provide a region in which there was paper soaked with MNP surrounded by water and another region where there was only paper surrounded by water to act as a control.

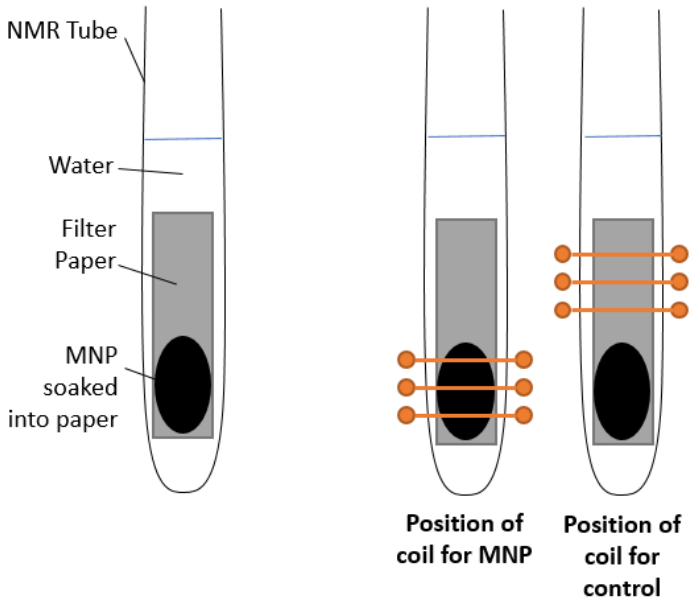

Figure 73: A diagram of an experiment utilising MNP solution absorbed into filter paper, placed into an NMR tube filled with a large volume of PDMS oil. The tube was positioned using two separate methods where the RF coil was placed around the MNP for the experimental measure and then to a section of MNP-free filter paper to act as a control.

Due to an increased quantity of MNP absorbed into the paper, a much larger change in values was reported:

	T_x (Microcontroller)	**T_1 (IR)**	**T_2^{eff} (CPMG)**
Water + Paper (Control)	-0.0153±0.0005	3230±60ms	2230±20ms
Water, Paper + MNP	-0.0101±0.0004	3080±90ms	1890±60ms

A 33.99% reduction in T_x is measured in the presence of MNP over the control, which is a considerable change in comparison to the 4.64% reduction in T_1 and 15.24% reduction in T_2^{eff}.

3.8. Industrial Application Trials

As measurements with the microcontroller system had mostly been consigned to calibration samples, a practical application on the commercial viability of the system was required. As discussed earlier in the chapter, food science is an area where NMR has been employed, utilising both pulsed and CW methods. One specific foodstuff was selected in dehydrated milk powder. The dehydration of milk is important in not only improving shelf-life but in preventing microbial growth within the product which can lead to spoiling and health issues when consumed. The golden standard of analysing water content in food is Karl-Fischer titration although this can be challenging to automate, labour intensive and has a significant cost investment in equipment. As water contains a large amount of hydrogen, magnetic resonance should be a useful tool in the analysis of moisture content.

3.8.1. Milk Powder Preparation

To measure the effect of milk powder concentration on measured T_x, 0.1% fat skimmed milk powder (Sainsbury's, UK) was mixed with distilled water to prepare test samples at six different concentrations (5%, 10%, 15%, 20%, 25% and 30% w/v). These samples were loaded into NMR tubes before being placed into the CW sensor.

In order to measure the effect of water absorption/adsorption from the surrounding environment, known as the hygroscopicity, in milk powder on T_x, 5g samples of 0.1% fat

skimmed milk powder were loaded into lid-less petri dishes and placed into a Thermotron 3200 (Thermotron, MI, USA) benchtop environment chamber. To work out the ideal parameters for the environment chamber, samples were placed inside at 75%, 85% and 95% relative humidity, all at 20°C. Upon completion of this investigation, the environmental parameters were kept at 20°C and 85% relative humidity for further experiments.
A 20g sample of milk powder was stored in the environment chamber for 90 minutes to ensure a large uptake of moisture. Milk powder solutions were then made at varying concentrations (20%, 25%, 30%, 35% & 40% w/v) with both the wet powder and a dry control powder. The T_x of each concentration was compared for the wet and dry powder solutions to decide on the appropriate concentration to be used for future experiments.
2g of the wetted powder was mixed with 5ml of distilled water and moved to an ultrasound bath to sonicate the mixture for 40 minutes to ensure it had been reasonably degassed after mixing. This was performed as oxygen is known to be paramagnetic which could interfere with taking NMR measurements. The water in the ultrasound bath was replaced with fresh room temperature water every 10 minutes to prevent heating of the sample. These degassed samples were then loaded into NMR tubes before placing them into the CW sensor

3.8.2. TEDSpil: Determining Milk Powder Hydration

Longitudinal relaxation times were measured using a selection of the previously mentioned hydrated milk powders. Selecting the solutions made from powders exposed to the environment chamber for 0, 10, 20, 40, 60 and 90 minutes.
Higher concentrations of milk powder in distilled water leads to an increase in viscosity due to the abundance of lactose, proteins and fats which is known to decrease spin-lattice relaxation times (Colsenet et al., 2005; Todt et al., 2006).
Shown below is the effect of humidity in the environment chamber on the NMR signal of the milk powder. A higher relative humidity corresponds to a faster uptake in atmospheric moisture as well as increasing the maximum amount of retained moisture, where 85% relative humidity presents a good balance between maximum retained moisture and the rate of uptake.

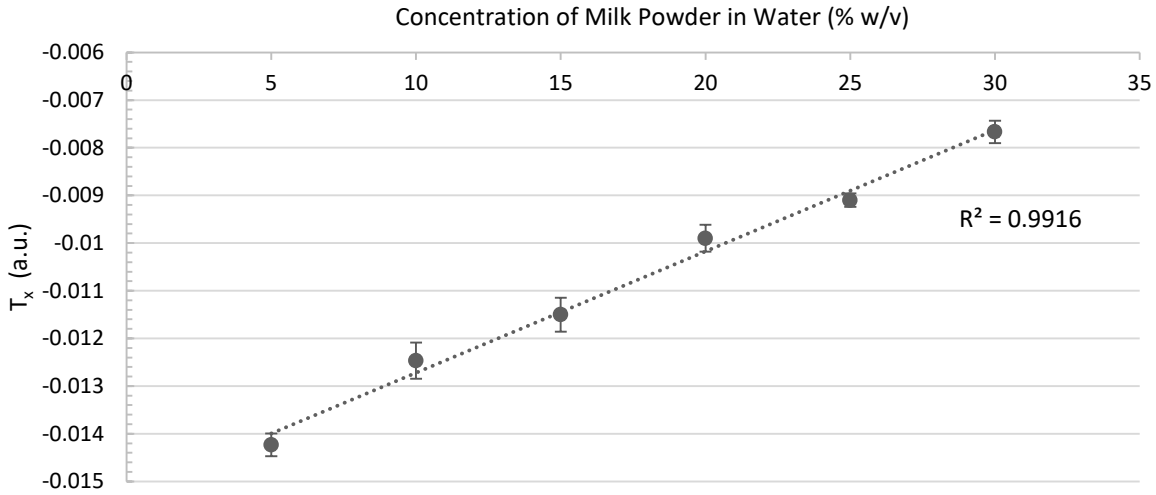

Figure 74: CWNMR T_x values against the concentration of skimmed milk powder solutions.

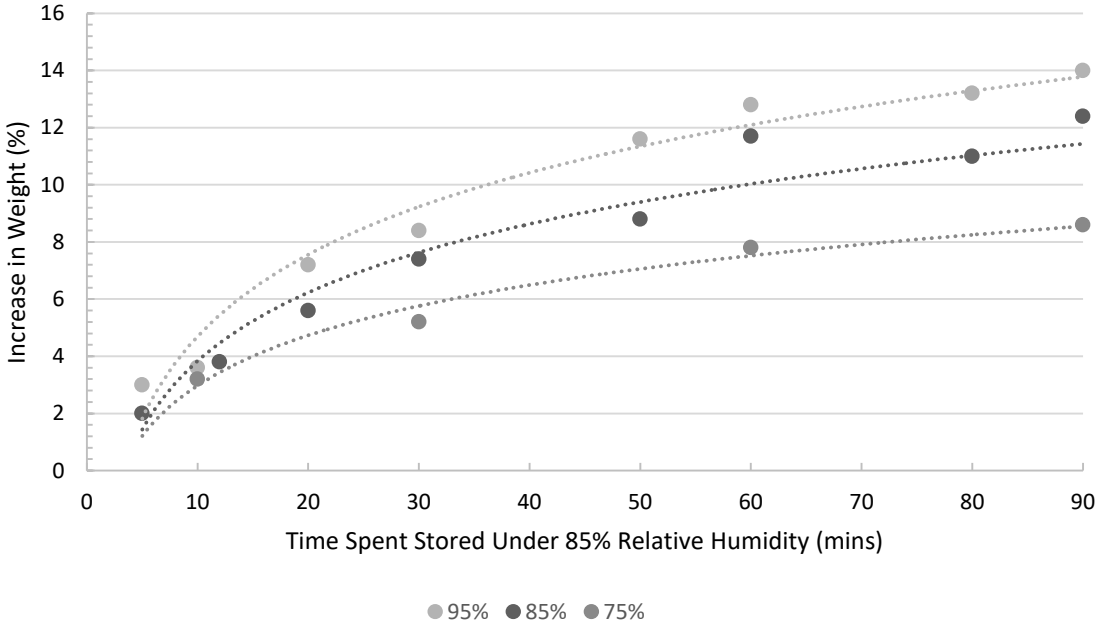

Figure 75: The increase of weight of a 2g sample of milk powder after it has been subjected to an environment chamber of varying humidity and time due to moisture uptake.

The comparison between dry and wet powder for different concentrations of milk powder solution is shown below. For concentrations under 40% w/v, the difference in T_x between the wet and dry samples is marginal, but at 40% w/v the difference between wet and dry

becomes significant. For this reason, 40% w/v solutions were used as the standard concentration for all future experiments.

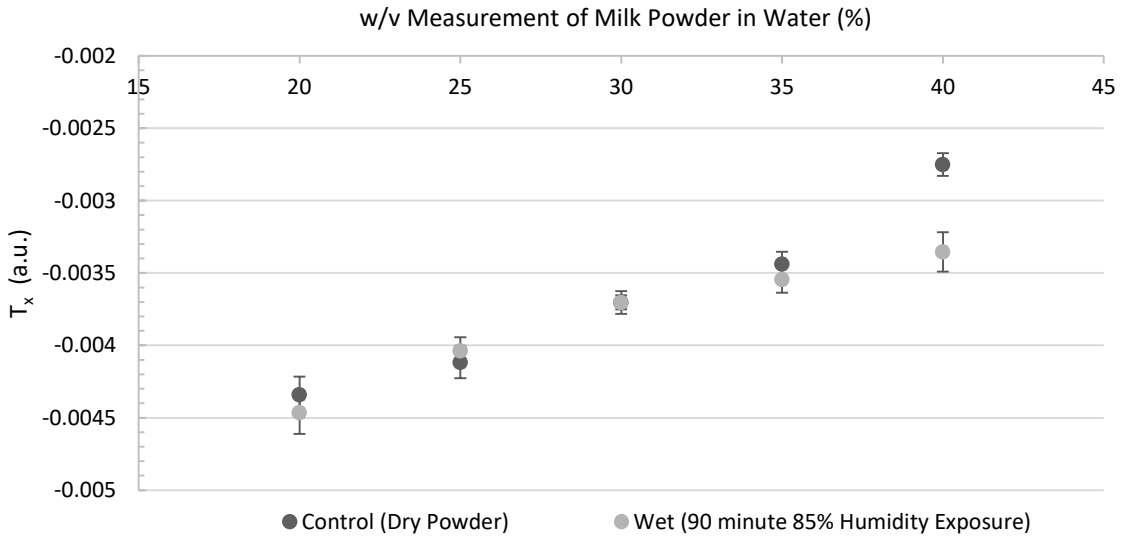

Figure 76: T_x measurements of wet and dry milk powder made up into varying w/v solutions. At 40% w/v, there is a noticeable change in the measured T_x.

The effect of sonication is demonstrated below. After mixing the skimmed milk powder with distilled water the solution becomes aerated presenting a change in the T_x due to the presence of paramagnetic oxygen. Sonicating the sample helps remove trapped air in the milk mixture assisting the reliability of T_x measurements. 40 minutes of sonication was enough to remove enough air in the sample so that repeated measurements fell in the same error range as measurements made at larger sonication times.

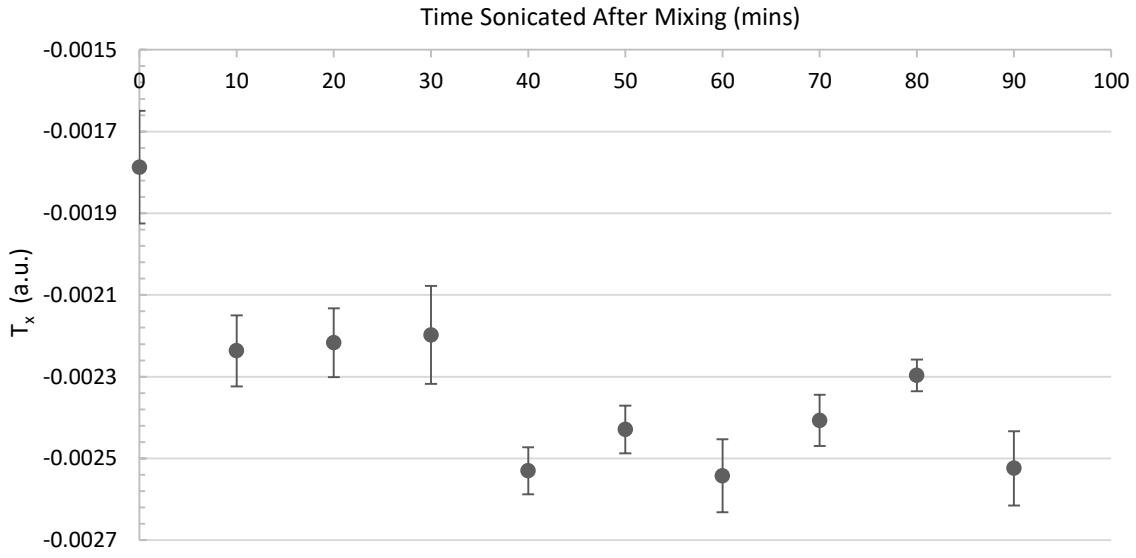

Figure 77: The effect of sonication on prepared milk solutions. A considerable drop in T_x is found after ten seconds, but after this time further sonication attempts provide negligible changes.

The major focus of this investigation is presented further on. When wetter powders are made up into a 40% w/v concentration solution, the measured T_x decreases. This is due to less milk powder attributing to the 2g weight, with some of it being water. As such, the true concentration will be lower than that which is measured. Through this concept it is possible to create a calibration set of known moisture levels in milk powders and use it to measure the amount of water in an unknown sample to ensure it has been successfully and appropriately dehydrated.

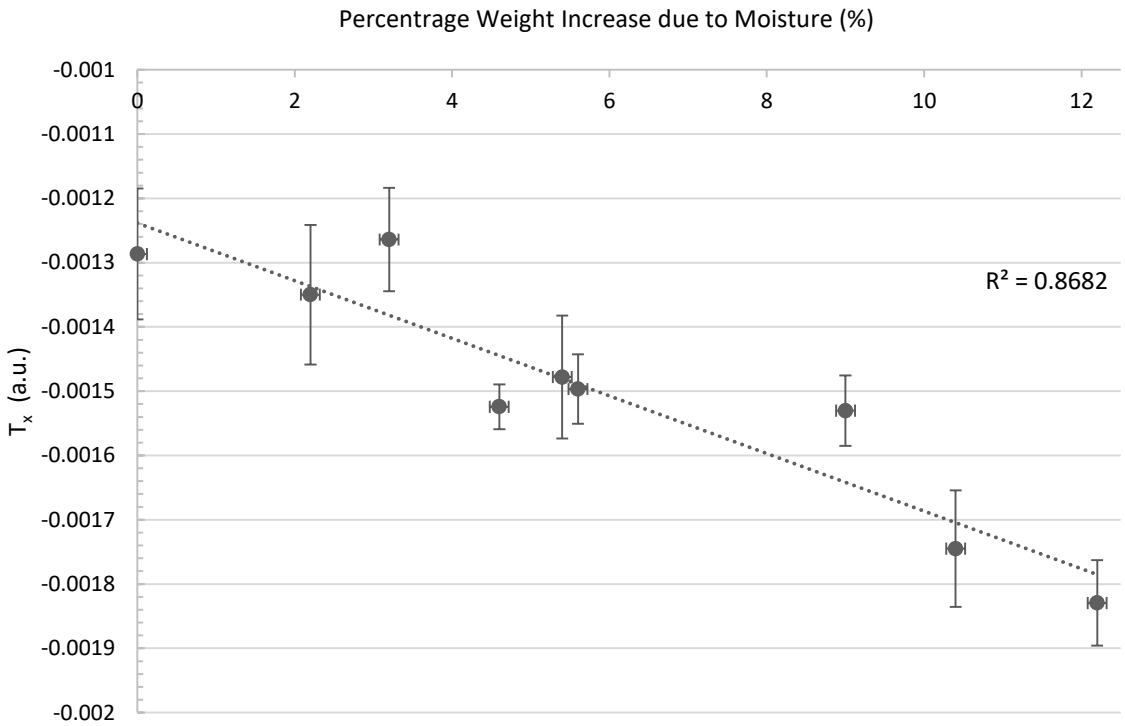

Figure 78: CWNMR T_x values against percentage moisture of milk powder made to 40% w/v solutions.

3.9. Conclusions

Through a modification of Lock and Locker's tone-burst experiments, a new technique coined "TEDSpiL" has been developed through observing the transient effect in CW-NMR through the use of a marginal oscillator. A permanent magnet design based on the commercial electromagnets supplied as part of LD Diactic's CW-NMR teaching apparatus was utilised along with high speed, National Instruments data capture card driven with LABVIEW operating software. It was shown that such a system can provide a determination of the spin-lattice relaxation times when a measurement commences with two known calibration samples.

Through the use of cost-effective microcontrollers, the data acquisition card was replaced with a Teensy 3.6 and Teensy 3.5. As the operating code could be stored inside the FLASH memory located on the device this eliminated the requirement for a desktop computer/laptop to operate the device. The uploaded code was put through a number of revisions to ensure optimal data capture with the limited RAM available to such a small device.

The electronics, commonly referred to as the console, for low field pulsed NMR systems typically cost more than $20k as they are designed to be wide band and highly programmable spectrometers. The process of making T_1 measurements with such a pulsed system usually use saturation or inversion recovery sequences that will typically take many minutes to give a single T_1 value. Whilst the T_x value is not a direct equivalent for T_1, there are applications where such a method may provide a cost-effective measurement technique.

CW-NMR has been demonstrated to distinguish between the moisture levels of skimmed milk powder when it is rehydrated to a 40% w/v solution. The sensor and electronics used in this investigation are orders of magnitude cheaper than the industry standard of using Karl Fischer to measure the moisture level of the milk powder, proving a cost-effective analytical method that is easy and intuitive to use.

The sensitivity of CW-NMR has also been compared to traditional pulsed techniques showing that it can more easily distinguish between smaller changes in T_1.

REFERENCES

Alhogail, S., Suaifan, G.A.R.Y., Zourob, M., 2016. Rapid colorimetric sensing platform for the detection of Listeria monocytogenes foodborne pathogen. Biosens. Bioelectron. https://doi.org/10.1016/j.bios.2016.07.043

Andrew, E.R., 1969. Nuclear Magnetic Resonance, Cambridge Monographs on Physics. Cambridge University Press.

Bannas, P., Graumann, O., Balcerak, P., Peldschus, K., Kaul, M.G., Hohenberg, H., Haag, F., Adam, G., Ittrich, H., Koch-Nolte, F., 2010. Quantitative magnetic resonance imaging of enzyme activity on the cell surface: In vitro and in vivo monitoring of ADP-ribosyltransferase 2 on T cells. Mol. Imaging. https://doi.org/10.2310/7290.2010.00017

Barrett, S.F., Pack, D.J., 2005. Microcontrollers fundamentals for engineers and scientists. Synth. Lect. Digit. Circuits Syst. https://doi.org/10.2200/S00025ED1V01Y200605DCS001

Bilir, S.P., Ferrufino, C.P., Pfaller, M.A., Munakata, J., 2015. The economic impact of rapid Candida species identification by T2Candida among high-risk patients. Future Microbiol. https://doi.org/10.2217/fmb.15.29

Blamey, J.W., Smith, W.I.B., 1950. Nuclear resonance and magnetic field changes of 1 in 106. Nature. https://doi.org/10.1038/1651015a0

Bloch, F., Hansen, W.W., Packard, M., 1946. The nuclear induction experiment. Phys. Rev. https://doi.org/10.1103/PhysRev.70.474

Bloembergen, N., Purcell, E.M., Pound, R. V., 1948. Relaxation effects in nuclear magnetic resonance absorption. Phys. Rev. https://doi.org/10.1103/PhysRev.73.679

Blümich, B., 2005. Essential NMR: For scientists and engineers, Essential NMR: For Scientists and Engineers. https://doi.org/10.1007/b138660

Blümich, B., Casanova, F., Appelt, S., 2009. NMR at low magnetic fields. Chem. Phys. Lett. https://doi.org/10.1016/j.cplett.2009.06.096

Blümich, B., Perlo, J., Casanova, F., 2008. Mobile single-sided NMR. Prog. Nucl. Magn. Reson. Spectrosc. https://doi.org/10.1016/j.pnmrs.2007.10.002

Bridot, J.L., Faure, A.C., Laurent, S., Rivière, C., Billotey, C., Hiba, B., Janier, M., Josserand, V., Coll, J.L., Elst, L. Vander, Muller, R., Roux, S., Perriat, P., Tillement, O., 2007. Hybrid gadolinium oxide nanoparticles: Multimodal contrast agents for in vivo imaging. J. Am. Chem. Soc. https://doi.org/10.1021/ja068356j

Brigger, I., Dubernet, C., Couvreur, P., 2012. Nanoparticles in cancer therapy and diagnosis. Adv. Drug Deliv. Rev. https://doi.org/10.1016/j.addr.2012.09.006

Bydder, G.M., Young, I.R., 1985. Mr imaging: Clinical use of the inversion recovery sequence. J. Comput. Assist. Tomogr. https://doi.org/10.1097/00004728-198507010-00002 Carr, H.Y., Purcell, E.M., 1954. Effects of diffusion on free precession in nuclear magnetic resonance experiments. Phys. Rev. https://doi.org/10.1103/PhysRev.94.630

Caravan, P., Ellison, J.J., McMurry, T.J., Lauffer, R.B., 1999. Gadolinium(III) chelates as MRI contrast agents: Structure, dynamics, and applications. Chem. Rev. https://doi.org/10.1021/cr980440x

Carr, H.Y., Purcell, E.M., 1954. Effects of diffusion on free precession in nuclear magnetic resonance experiments. Phys. Rev. https://doi.org/10.1103/PhysRev.94.630

Cherubini, A., Bifone, A., 2003. Hyperpolarised xenon in biology. Prog. Nucl. Magn. Reson. Spectrosc. https://doi.org/10.1016/S0079-6565(02)00052-3

Christofer Adding, L., Bannenberg, G.L., Gustafsson, L.E., 2001. Basic experimental studies and clinical aspects of gadolinium salts and chelates. Cardiovasc. Drug Rev.

Clarke, C., 2019. Free Induction Decay [WWW Document]. URL https://www.radiologycafe.com/radiology-trainees/frcr-physics-notes/t1-and-t2-signal (accessed 9.3.19).

Collins, R.L., 1957. Automatic bridge balance for nuclear spin resonance spectrometer. Rev. Sci. Instrum. https://doi.org/10.1063/1.1715920

Colsenet, R., Mariette, F., Cambert, M., 2005. NMR relaxation and water self-diffusion studies in whey protein solutions and gels. J. Agric. Food Chem. https://doi.org/10.1021/jf050162k

Conway, T.F., 1971. A wide line NMR R-F saturation method to measure fat in moist samples of defatted corn germ. J. Am. Oil Chem. Soc. https://doi.org/10.1007/BF02635685

Cuker, A., Husseinzadeh, H., Lebedeva, T., Marturano, J.E., Massefski, W., Lowery, T.J., Lambert, M.P., Abrams, C.S., Weisel, J.W., Cines, D.B., 2016. Rapid evaluation of platelet function with T2 magnetic resonance. Am. J. Clin. Pathol. https://doi.org/10.1093/AJCP/AQW189

Danieli, E., Mauler, J., Perlo, J., Blümich, B., Casanova, F., 2009. Mobile sensor for high resolution NMR spectroscopy and imaging. J. Magn. Reson. https://doi.org/10.1016/j.jmr.2009.01.022

Danieli, E., Perlo, J., Blümich, B., Casanova, F., 2010. Small magnets for portable NMR spectrometers. Angew. Chemie - Int. Ed. https://doi.org/10.1002/anie.201000221

De Frates, K., Markiewicz, T., Gallo, P., Rack, A., Weyhmiller, A., Jarmusik, B., Hu, X., 2018. Protein polymer-based nanoparticles: Fabrication and medical applications. Int. J. Mol. Sci. https://doi.org/10.3390/ijms19061717

De Leõn-Rodríguez, L.M., Martins, A.F., Pinho, M.C., Rofsky, N.M., Sherry, A.D., 2015. Basic MR relaxation mechanisms and contrast agent design. J. Magn. Reson. Imaging. https://doi.org/10.1002/jmri.24787

De Smet, F., Moreau, Y., Engelen, K., Timmerman, D., Vergote, I., De Moor, B., 2004. Balancing false positives and false negatives for the detection of differential expression in malignancies. Br. J. Cancer. https://doi.org/10.1038/sj.bjc.6602140

Domingo-Roca, R., Jackson, J.C., Windmill, J.F.C., 2018. 3D-printing polymer-based permanent magnets. Mater. Des. https://doi.org/10.1016/j.matdes.2018.05.005

Donnally, B., Sanders, T.M., 1960. Simple transistor marginal oscillator for magnetic resonance. Rev. Sci. Instrum. https://doi.org/10.1063/1.1717122

Donnally, B.L., Bernal G, E., 1963. Some Experiments on Nuclear Magnetic Resonance. Am. J. Phys. https://doi.org/10.1119/1.1969081

Drain, L.E., 1949. A direct method of measuring nuclear spin-lattice relaxation times. Proc. Phys. Soc. Sect. A. https://doi.org/10.1088/0370-1298/62/5/306

Du Vigneaud, V., Hofmann, K., Melville, D.B., Rachele, J.R., 1941. THE PREPARATION OF FREE CRYSTALLINE BIOTIN. J. Biol. Chem.

Duguet, E., Vasseur, S., Mornet, S., Devoisselle, J.M., 2006. Magnetic nanoparticles and their applications in medicine. Nanomedicine. https://doi.org/10.2217/17435889.1.2.157

EFY Group, 2019. Microcontroller Basics [WWW Document]. URL https://electronicsforu.com/resources/pic-microcontroller-tutorial-for-beginners (accessed 9.4.19).

Eidmann, G., Savelsberg, R., Blümler, P., Blümich, B., 1996. The NMR MOUSE, a mobile universal surface explorer. J. Magn. Reson. - Ser. A. https://doi.org/10.1006/jmra.1996.0185

Elster, A., n.d. Superconducting Magnets [WWW Document]. URL http://mriquestions.com/superconductive-design.html (accessed 9.2.19).

Energy, U.S.D. of, 2011. Critical Materials Strategy [WWW Document]. URL https://www.energy.gov/sites/prod/files/DOE_CMS2011_FINAL_Full.pdf (accessed 8.30.19).

Ernst, R.R., Bodenhausen, G., Wokaun, A., Redfield, A.G., 1989. Principles of Nuclear Magnetic Resonance in One and Two Dimensions Phys. Today. https://doi.org/10.1063/1.2811094

Faulkner, E.A., Holman, A., 1967. An improved circuit for nuclear magnetic resonance detection. J. Sci. Instrum. https://doi.org/10.1088/0950-7671/44/5/418

Firth, L.D., 1982. Relaxation time measurement by continuous-wave NMR. Eur. J. Phys. https://doi.org/10.1088/0143-0807/3/1/003

Furlong, D.N., 1997. Quartz crystal microbalance study of DNA immobilization and hybridization for nucleic acid sensor development. Anal. Chem.

Green, N.M., 1975. Advances in Protein Chemistry Volume 29. Adv. Protein Chem. https://doi.org/10.1016/S0065-3233(08)60411-8

Gruetter, R., Weisdorf, S.A., Rajanayagan, V., Terpstra, M., Merkle, H., Truwit, C.L., Garwood, M., Nyberg, S.L., Uğurbil, K., 1998. Resolution Improvements in in Vivo 1H NMR Spectra with Increased Magnetic Field Strength. J. Magn. Reson. https://doi.org/10.1006/jmre.1998.1542

Haber, A., Blümich, B., Souvorova, D., Del Federico, E., 2011. Ancient Roman wall paintings mapped nondestructively by portable NMR. Anal. Bioanal. Chem. https://doi.org/10.1007/s00216-011-5180-3

Hahn, E.L., 1950. Spin echoes. Phys. Rev. https://doi.org/10.1103/PhysRev.80.580

Halbach, K., 1980. Design of permanent multipole magnets with oriented rare earth cobalt material. Nucl. Instruments Methods. https://doi.org/10.1016/0029-554X(80)90094-4

Hall, A., Mundell, V.J., Blanco-Andujar, C., Bencsik, M., McHale, G., Newton, M.I., Cave, G.W.V., 2010. Towards MRI microarrays. Chem. Commun.

Hall, G.E., Lawrence, J.G., Simpson, R.J., 1967. Nuclear magnetic resonance as a method for continuously monitoring rehydration [11]. Nature. https://doi.org/10.1038/216474a0

Haun, J.B., Castro, C.M., Wang, R., Peterson, V.M., Marinelli, B.S., Lee, H., Weissleder, R., 2011. Micro-NMR for rapid molecular analysis of human tumor samples. Sci. Transl. Med. https://doi.org/10.1126/scitranslmed.3002048

Hennig, J., Nauerth, A., Friedburg, H., 1986. RARE imaging: A fast imaging method for clinical MR. Magn. Reson. Med. https://doi.org/10.1002/mrm.1910030602

Herrmann, I.K., Urner, M., Koehler, F.M., Hasler, M., Roth-Z'graggen, B., Grass, R.N., Ziegler, U., Beck-Schimmer, B., Stark, W.J., 2010. Blood purification using functionalized

core/shell nanomagnets. Small. https://doi.org/10.1002/smll.201000438

Hong Nguyen, M., Clancy, C.J., William Pasculle, A., Pappas, P.G., Alangaden, G., Pankey, G.A., Schmitt, B.H., Rasool, A., Weinstein, M.P., Widen, R., Hernandez, D.R., Wolk, D.M., Walsh, T.J., Perfect, J.R., Wilson, M.N., Mylonakis, E., 2019. Performance of the T2bacteria panel for diagnosing bloodstream infections. Ann. Intern. Med. https://doi.org/10.7326/M18-2772

Huang, S.H., Juang, R.S., 2011. Biochemical and biomedical applications of multifunctional magnetic nanoparticles: A review. J. Nanoparticle Res. https://doi.org/10.1007/s11051-011-0551-4

Huber, C., Abert, C., Bruckner, F., Groenefeld, M., Muthsam, O., Schuschnigg, S., Sirak, K., Thanhoffer, R., Teliban, I., Vogler, C., Windl, R., Suess, D., 2016. 3D print of polymer bonded rare-earth magnets, and 3D magnetic field scanning with an end-user 3D printer. Appl. Phys. Lett. https://doi.org/10.1063/1.4964856

Hughes-Riley, T., Dye, E.R., Ortega Anderez, D., Hill-Casey, F., Newton, M.I., Morris, R.H., 2016. Temperature dependence of magnetic resonance probes for use as embedded sensors in constructed wetlands. Sensors Actuators, A Phys. https://doi.org/10.1016/j.sna.2016.01.050

Hugon, C., Aguiar, P.M., Aubert, G., Sakellariou, D., 2010. Design, fabrication and evaluation of a low-cost homogeneous portable permanent magnet for NMR and MRI. Comptes Rendus Chim. https://doi.org/10.1016/j.crci.2009.09.009

Indira, T., 2010. Magnetic Nanoparticles: A Review. Int. J. Pharm.

Ittrich, H., Peldschus, K., Raabe, N., Kaul, M., Adam, G., 2013. Superparamagnetic iron oxide nanoparticles in biomedicine: Applications and developments in diagnostics and therapy. RoFo Fortschritte auf dem Gebiet der Rontgenstrahlen und der Bildgeb. Verfahren. https://doi.org/10.1055/s-0033-1335438

Jaćimović, J., Binda, F., Herrmann, L.G., Greuter, F., Genta, J., Calvo, M., Tomše, T., Simon, R.A., 2017. Net Shape 3D Printed NdFeB Permanent Magnet. Adv. Eng. Mater. https://doi.org/10.1002/adem.201700098Hanini, A., Schmitt, A., Kacem, K., Chau, F., Ammar, S., & Gavard, J. (2011). Evaluation of iron oxide nanoparticle biocompatibility. International journal of nanomedicine. https://doi.org/10.2147/IJN.S17574

Jacobsohn, B.A., Wangsness, R.K., 1948. Shapes of nuclear induction signals. Phys. Rev. https://doi.org/10.1103/PhysRev.73.942

Koh, I., Hong, R., Weissleder, R., Josephson, L., 2008. Sensitive NMR sensors detect antibodies to influenza. Angew. Chemie - Int. Ed. https://doi.org/10.1002/anie.200800069

Kozitsina, A., Svalova, T., Malysheva, N., Glazyrina, Y., Matern, A., 2016. A New Enzyme-Free Electrochemical Immunoassay for Escherichia coli Detection using Magnetic Nanoparticles. Anal. Lett. https://doi.org/10.1080/00032719.2015.1072824

Kraulis, P.J., 1991. MOLSCRIPT. A program to produce both detailed and schematic plots of protein structures. J. Appl. Crystallogr.

Ladner, W.R., Stacey, A.E., 1962. Measurement of moisture in a moving coal feed. Br. J. Appl. Phys. https://doi.org/10.1088/0508-3443/13/3/118

Lauffer, R.B., 1987. Paramagnetic Metal Complexes as Water Proton Relaxation Agents for NMR Imaging: Theory and Design. Chem. Rev. https://doi.org/10.1021/cr00081a003

LD Didactic, 2019. Atomic and Nuclear Physics [WWW Document]. URL https://www.ld-didactic.de/literatur/hb/e/p6/p6531_e.pdf (accessed 9.4.19).

Lee, H., Shin, T.H., Cheon, J., Weissleder, R., 2015. Recent Developments in Magnetic Diagnostic Systems. Chem. Rev. https://doi.org/10.1021/cr500698d

Lee, H., Sun, E., Ham, D., Weissleder, R., 2008. Chip-NMR biosensor for detection and molecular analysis of cells. Nat. Med. https://doi.org/10.1038/nm.1711

Libretexts, 2019. Inversion Recovery [WWW Document]. URL https://chem.libretexts.org/Bookshelves/Physical_and_Theoretical_Chemistry_Textbook_Maps/Supplemental_Modules_(Physical_and_Theoretical_Chemistry)/Spectroscopy/Magnetic_Resonance_Spectroscopies/Nuclear_Magnetic_Resonance/NMR%3A_Theory/Relaxation/Spin_Lattice_Relaxation (accessed 9.4.19).

Livnah, O., Bayer, E.A., Wilchek, M., Sussman, J.L., 1993. Three-dimensional structures of avidin and the avidin-biotin complex, in: Proceedings of the National Academy of Sciences of the United States of America. https://doi.org/10.1073/pnas.90.11.5076

Look, D.C., Locker, D.R., 1968. Nuclear spin-lattice relaxation measurements by tone-burst modulation. Phys. Rev. Lett. https://doi.org/10.1103/PhysRevLett.20.987

Look, D.C., Locker, D.R., 1970. Time saving in measurement of NMR and EPR relaxation times. Rev. Sci. Instrum. https://doi.org/10.1063/1.1684482

Lowe, I.J., Norberg, R.E., 1957. Free-induction decays in solids. Phys. Rev. https://doi.org/10.1103/PhysRev.107.46

Lu, A.H., Salabas, E.L., Schüth, F., 2007. Magnetic nanoparticles: Synthesis, protection, functionalization, and application. Angew. Chemie - Int. Ed. https://doi.org/10.1002/anie.200602866

Makarov, B., Ryzhov, V., 2010. Advance of marginal oscillator, in: RuPAC 2010 Contributions to the Proceedings - 22nd Russian Particle Accelerator Conference.

Mansfield, P., 1977. Multi-planar image formation using NMR spin echoes. J. Phys. C Solid State Phys. https://doi.org/10.1088/0022-3719/10/3/004

McDowell, A., Fukushima, E., 2008. Ultracompact NMR: 1H spectroscopy in a subkilogram magnet. Appl. Magn. Reson. https://doi.org/10.1007/s00723-008-0151-3

McDowell, A.F., 2018. Adjustable passive shims for dipole NMR magnets. J. Magn. Reson. https://doi.org/10.1016/j.jmr.2018.09.008

Meiboom, S., Gill, D., 1958. Modified spin-echo method for measuring nuclear relaxation times. Rev. Sci. Instrum. https://doi.org/10.1063/1.1716296

Mertens, W.G., deMan, J.M., 1972. The Influence of Temperature Treatment on Solid-Liquid Ratios of Fats Determined by Wide-Line NMR. Can. Inst. Food Sci. Technol. J. https://doi.org/10.1016/s0315-5463(72)74092-4

Michael Green, N., 1990. Avidin and Streptavidin. Methods Enzymol. https://doi.org/10.1016/0076-6879(90)84259-J

Middleton, H., Black, R.D., Saam, B., Cates, G.D., Cofer, G.P., Guenther, R., Happer, W., Hedlund, L.W., Alan Johnson, G., Juvan, K., Swartz, J., 1995. MR Imaging with Hyperpolarized 3He Gas. Magn. Reson. Med. https://doi.org/10.1002/mrm.1910330219

Möller, H.E., Chen, X.J., Saam, B., Hagspiel, K.D., Johnson, G.A., Altes, T.A., De Lange, E.E., Kauczor, H.U., 2002. MRI of the lungs using hyperpolarized noble gases. Magn. Reson. Med. https://doi.org/10.1002/mrm.10173

Mornet, S., Vasseur, S., Grasset, F., Duguet, E., 2004. Magnetic nanoparticle design for medical diagnosis and therapy. J. Mater. Chem. https://doi.org/10.1039/b402025a

Muñoz, P., Vena, A., Machado, M., Martínez-Jiménez, M.C., Gioia, F., Gómez, E., Origüen, J., Orellana, M.Á., López-Medrano, F., Pérez-Granda, M.J., Aguado, J.M., Fortún, J., Bouza, E., Navarro, R., Sánchez, C., Soriano, C., Pestaña, D., Gonzalez-Romo, F., Merino, P., Fernández-Ruiz, M., Orellana, M.A., 2018. T2MR contributes to the very early diagnosis of complicated candidaemia. A prospective study. J. Antimicrob. Chemother.

https://doi.org/10.1093/jac/dky048

Oref, I., 1965. Fat content and liquid-to-solid ratio of chocolate by wide line nuclear magnetic resonance. J. Am. Oil Chem. Soc. https://doi.org/10.1007/BF02635583

Perlo, J., Casanova, F., Blümich, B., 2004. 3D imaging with a single-sided sensor: An open tomograph. J. Magn. Reson. https://doi.org/10.1016/j.jmr.2003.10.018

Perlo, J., Casanova, F., Blümich, B., 2005. Profiles with microscopic resolution by single-sided NMR. J. Magn. Reson. https://doi.org/10.1016/j.jmr.2005.05.017

Perlo, J., Casanova, F., Blümich, B., 2006. Single-sided sensor for high-resolution NMR spectroscopy. J. Magn. Reson. https://doi.org/10.1016/j.jmr.2006.03.004

PJRC, 2019. Teensy USB Development Board [WWW Document]. URL https://www.pjrc.com/teensy/ (accessed 9.4.19).

Pohle, W.D., Taylor, J.R., Gregory, R.L., 1965. A comparison of nuclear magnetic resonance and dilatometry for estimating solids content of fats and shortenings. J. Am. Oil Chem. Soc. https://doi.org/10.1007/BF02636912

Pouliquen, D., Perdrisot, R., Ermias, A., Akoka, S., Jallet, P., Le Jeune, J.J., 1989. Superparamagnetic iron oxide nanoparticles as a liver MRI contrast agent: Contribution of microencapsulation to improved biodistribution. Magn. Reson. Imaging. https://doi.org/10.1016/0730-725X(89)90530-4

Pound, R. V., Knight, W.D., 1950. A radiofrequency spectrograph and simple magnetic-field meter. Rev. Sci. Instrum. https://doi.org/10.1063/1.1745537

Raich, H., Blümler, P., 2004. Design and construction of a dipolar Halbach array with a homogeneous field from identical bar magnets: NMR mandhalas. Concepts Magn. Reson. Part B Magn. Reson. Eng. https://doi.org/10.1002/cmr.b.20018

Ramdas, L., Coombes, K.R., Baggerly, K., Abruzzo, L., Highsmith, W.E., Krogmann, T., Hamilton, S.R., Zhang, W., 2001. Sources of nonlinearity in cDNA microarray expression measurements. Genome Biol.

Rata, D.G., Casanova, F., Perlo, J., Demco, D.E., Blümich, B., 2006. Self-diffusion measurements by a mobile single-sided NMR sensor with improved magnetic field gradient. J. Magn. Reson. https://doi.org/10.1016/j.jmr.2006.02.015

Reilly, R.F., 2008. Risk for nephrogenic systemic fibrosis with gadoteridol (ProHance) in patients who are on long-term hemodialysis. Clin. J. Am. Soc. Nephrol. https://doi.org/10.2215/CJN.05721207

Robinson, F.N.H., 1959. Nuclear resonance absorption circuit. J. Sci. Instrum. https://doi.org/10.1088/0950-7671/36/12/301

Robinson, F.N.H., 1965. A high field nuclear magnetic resonance probe using transistors. J. Sci. Instrum. https://doi.org/10.1088/0950-7671/42/8/344

Robinson, F.N.H., 1987. The modified van der pol oscillator. IMA J. Appl. Math. (Institute Math. Its Appl. https://doi.org/10.1093/imamat/38.2.135

Robinson, H.R., 1951. Voltage variations of lead-acid accumulators at small discharge rates [3]. J. Sci. Instrum. https://doi.org/10.1088/0950-7671/28/2/112

Sandhu, A., Handa, H., Abe, M., 2010. Synthesis and applications of magnetic nanoparticles for biorecognition and point of care medical diagnostics. Nanotechnology. https://doi.org/10.1088/0957-4484/21/44/442001

Schena, M., Shalon, D., Davis, R.W., Brown, P.O., 1995. Quantitative monitoring of gene expression patterns with a complementary DNA microarray. Science (80-.). https://doi.org/10.1126/science.270.5235.467

Senyei, A., Widder, K., Czerlinski, G., 1978. Magnetic guidance of drug-carrying microspheres. J. Appl. Phys. https://doi.org/10.1063/1.325219

Shafiee, H., Jahangir, M., Inci, F., Wang, S., Willenbrecht, R.B.M., Giguel, F.F., Tsibris, A.M.N., Kuritzkes, D.R., Demirci, U., 2013. Acute on-chip HIV detection through label-free electrical sensing of viral nano-lysate. Small. https://doi.org/10.1002/smll.201202195

Shaw, T.M., Elsken, R.H., 1956. Determination of Water by Nuclear Magnetic Absorption in Potato and Apple Tissue. J. Agric. Food Chem. https://doi.org/10.1021/jf60060a008

Sillerud, L.O., McDowell, A.F., Adolphi, N.L., Serda, R.E., Adams, D.P., Vasile, M.J., Alam, T.M., 2006. 1H NMR Detection of superparamagnetic nanoparticles at 1 T using a microcoil and novel tuning circuit. J. Magn. Reson. https://doi.org/10.1016/j.jmr.2006.04.005

Skewis, L.R., Lebedeva, T., Papkov, V., Thayer, E.C., Massefski, W., Cuker, A., Nagaswami, C., Litvinov, R.I., Kowalska, M.A., Rauova, L., Poncz, M., Weisel, J.W., Lowery, T.J., Cines, D.B., 2014. T2 magnetic resonance: A diagnostic platform for studying integrated hemostasis in whole blood - Proof of concept. Clin. Chem. https://doi.org/10.1373/clinchem.2014.223735

Smith, J.A.S., 1953. Nuclear magnetic resonance absorption. Q. Rev. Chem. Soc. https://doi.org/10.1039/QR9530700279

Stanley, S.M., Dodi, I.A., Evans, C.R., Paston, S.J., Rees, R.C., Percival, C.J., McHale, G., Newton, M.I., 2006. Layer guided-acoustic plate mode biosensors for monitoring MHC-peptide interactions. Analyst. https://doi.org/10.1039/b604812a

Stoffregen, P., 2019. Audio Recorder Example [WWW Document].

Sun, N., Liu, Y., Qin, L., Lee, H., Weissleder, R., Ham, D., 2013. Small NMR biomolecular sensors. Solid. State. Electron. https://doi.org/10.1016/j.sse.2013.02.005

Saha, K., Agasti, S.S., Kim, C., Li, X., Rotello, V.M., 2012. Gold nanoparticles in chemical and biological sensing. Chem. Rev. https://doi.org/10.1021/cr2001178

Sandhu, A., Handa, H., Abe, M., 2010. Synthesis and applications of magnetic nanoparticles for biorecognition and point of care medical diagnostics. Nanotechnology. https://doi.org/10.1088/0957-4484/21/44/442001

Shipway, A.N., Katz, E., Willner, I., 2000. Nanoparticle arrays on surfaces for electronic, optical, and sensor applications. Angew. Chemie (International Ed. English).

Sillerud, L.O., McDowell, A.F., Adolphi, N.L., Serda, R.E., Adams, D.P., Vasile, M.J., Alam, T.M., 2006. 1H NMR Detection of superparamagnetic nanoparticles at 1 T using a microcoil and novel tuning circuit. J. Magn. Reson. https://doi.org/10.1016/j.jmr.2006.04.005

Soltner, H., Blümler, P., 2010. Dipolar Halbach magnet stacks made from identically shaped permanent magnets for magnetic resonance. Concepts Magn. Reson. Part A Bridg. Educ. Res. https://doi.org/10.1002/cmr.a.20165

Sun, N., Liu, Y., Qin, L., Lee, H., Weissleder, R., Ham, D., 2013. Small NMR biomolecular sensors. Solid. State. Electron. https://doi.org/10.1016/j.sse.2013.02.005

Thomson M. 2013. Modern particle physics. Cambridge University Press

Todt, H., Guthausen, G., Burk, W., Schmalbein, D., Kamlowski, A., 2006. Water/moisture and fat analysis by time-domain NMR, in: Food Chemistry. https://doi.org/10.1016/j.foodchem.2005.04.032

Villanueva, P., 2019. Teensy 3.x/LC ADC Implementation [WWW Document].

Wiginton, C.D., Kelly, B., Oto, A., Jesse, M., Aristimuno, P., Ernst, R., Chaljub, G., 2008. Gadolinium-based contrast exposure, nephrogenic systemic fibrosis, and gadolinium detection in tissue. Am. J. Roentgenol. https://doi.org/10.2214/AJR.07.2822

Wignarajah, S., Suaifan, G.A.R.Y., Bizzarro, S., Bikker, F.J., Kaman, W.E., Zourob, M., 2015. Colorimetric Assay for the Detection of Typical Biomarkers for Periodontitis Using a

Magnetic Nanoparticle Biosensor. Anal. Chem. https://doi.org/10.1021/acs.analchem.5b03018

Wilchek, M., Bayer, E.A., Livnah, O., 2006. Essentials of biorecognition: The (strept)avidin-biotin system as a model for protein-protein and protein-ligand interaction. Immunol. Lett. https://doi.org/10.1016/j.imlet.2005.10.022

Willingham, F.P., 1988. Developing improved nuclear magnetic resonance marginal oscillator spectrometers for advanced teaching laboratories.

Wilson, K.J., Vallabhan, C.P.G., 1989. A simple linear magnetic field sweep generator for magnetic resonance experiments. J. Phys. E. https://doi.org/10.1088/0022-3735/22/2/011

Wilson, K.J., Vallabhan, C.P.G., 1990. An improved MOSFET-based Robinson oscillator for NMR detection. Meas. Sci. Technol. https://doi.org/10.1088/0957-0233/1/5/015

Wolf, G.L., Halavaara, J.T., 1996. Basic principles of MR contrast agents. Magn. Reson. Imaging Clin. N. Am.

Yantasee, W., Fryxell, G.E., Porter, G.A., Pattamakomsan, K., Sukwarotwat, V., Chouyyok, W., Koonsiripaiboon, V., Xu, J., Raymond, K.N., 2010. Novel sorbents for removal of gadolinium-based contrast agents in sorbent dialysis and hemoperfusion: preventive approaches to nephrogenic systemic fibrosis. Nanomedicine Nanotechnology, Biol. Med. https://doi.org/10.1016/j.nano.2009.05.002

APPENDIX A: CODE

LabView Code (MATLAB Shell)

```
fwav = sw(1:SR./f);
low = SR./f;
[swm, swi] = max(fwav);
A = A(swi:end);
A = A(1:(floor(length(A)./(SR./f))*(SR./f)));
B = reshape(A, SR./f, length(A)./(SR./f));
sp = floor(low./4);
ep = low-sp;
B = B(:, sac:end);
sw = sw(swi:end);
sw = sw(1:(floor(length(A)./(SR./f))*(SR./f)));
figure(1)
imagesc(B)
[null, tm] = max(B(:,10));
aw = 200;
lm = tm-aw
um = tm + aw
if(lm<0); lm=1; end
if(um>(SR./f)); um=(SR./f); end
P = (max(B(lm:um, :)));
P(1) = P(2);
P = P(sac:end);
D = (1/f)*[1:length(P)];
```

Teensy 3.6 Starting Code

```
#include <TimeLib.h>
#include "ADC.h"
#include <SD.h>

// use of the fast adc routines for Teensy by Pedro Villanueva
ADC *adc = new ADC(); // adc object

void getDataLoop();
void SaveToFile();
const int ledPin = 13;
const int TrigPin = 12;
const int chipSelect = 4;

int sensor[60][1001]; // define array to hold adc values for 60 peaks
int trac;           // peak tracking variable
int PeakVal[60];     // array to hold the maximum of each peak

// Define the variables to read Real Time Clock and create filename
unsigned long intt;     // will hold the UTC time in seconds
```

```
char timbuf[10];       // will hold the 8 character conversion of intt
unsigned int test1;    // will hold the UTC number less the '15' at the start
int an;                // above bodge ok to September 2020
File dataFile;

void setup() {
   //set the input and output pin modes
   pinMode(ledPin, OUTPUT);
   pinMode(TrigPin, INPUT);
   pinMode(TrigPin, INPUT_PULLUP);

   // set the ADC converter resolution and speed setting
   adc->setResolution(16); // set bits of resolution
   adc->setAveraging(4);
   adc->setConversionSpeed(ADC_CONVERSION_SPEED::HIGH_SPEED);
   adc->setSamplingSpeed(ADC_SAMPLING_SPEED::VERY_HIGH_SPEED);

// start the serial monitor
   Serial.begin(9600);
// update time from real time clock
   setSyncProvider(getTeensy3Time);

  // look to see if the SD card is available
   if (!SD.begin(BUILTIN_SDCARD)) {
    for(int lq=0;lq<100;lq++){
     digitalWrite(ledPin, HIGH);   // quick flashing
     delay(50);                    // of LED
     digitalWrite(ledPin, LOW);    // if no SD card
     delay(50);    }               // is inserted
   }
//end of setup
}

 void loop() {
  trac=1;
   do{  Serial.println("in first do waiting for trigger");
       do{}while(digitalRead(TrigPin)==HIGH);
       Serial.println("got trigger");
     getDataLoop();
     Serial.println("got data");
     trac=trac+1;
    }while (trac<60);
    Serial.println("end of first do");
  SaveToFile();
  Serial.println("saved to file");

// wait before allowing next measurement minimum 5*T1
```

```
  delay(5000);

// end of loop back to beginning again
}

void getDataLoop()
{
            for (an = 0; an < 1000; an++)
              sensor[trac][an] = adc->analogRead(0);
             // reads 1000 points across peak number 'trac'
}

void SaveToFile()
{ // note if you remove the card it needs a re-boot to work
  digitalWrite(ledPin, HIGH);   // led on whist file write
  time_t rawtime = now();     //update to instantaneous time
  intt= rawtime;              // assign values to unsigned int
  Serial.println(" intt is ");
  Serial.println(intt);
  test1=intt-1500000000;      // need to have 8 character file name and UTC is 10 characters
                         // the '15' at the front will be the same until mid 2020 so lose it
 sprintf(timbuf,"%u",test1);  // put time in seconds into character array called buffer
 Serial.println(" test1 is");
Serial.println(test1);
Serial.println("timbuf is");
Serial.println(timbuf);
  dataFile = SD.open(timbuf, FILE_WRITE);
Serial.println("file open");
   String dataString = "";
    delay(50);

   for(int a=1; a<60;a++)PeakVal[a]=0;
     if(dataFile)
     {   delay(50);
        Serial.println("in if(dataFile) loop");
        for(trac=1; trac<60; trac++)
          for (an = 0; an < 1000; an++)
           {
             dataString = String(sensor[trac][an]);
             Serial.println(dataString);
             dataFile.println(dataString);
             // work through the array to find the peak in each sweep
             if(PeakVal[trac]<sensor[trac][an])PeakVal[trac]=sensor[trac][an];
           }

     for(trac=1; trac<60; trac++)
     {
```

```
        dataString = String(PeakVal[trac]);
              Serial.println(dataString);
              dataFile.println(dataString);
      }

      }

Serial.println("data written");
  dataFile.close();
  Serial.println("now for the peaks");
   for(int a=1; a<60;a++)
   {
    Serial.println(PeakVal[a]);
    }
Serial.println("file closed");
digitalWrite(ledPin, LOW);   // led off at end of file write
}

// stuff below updates the real time clock
time_t getTeensy3Time()
{
  return Teensy3Clock.get();
}
//  code to process time sync messages from the serial port
char TIME_HEADER[] = "T";
unsigned long processSyncMessage()
{
  unsigned long pctime = 0L;
  const unsigned long DEFAULT_TIME = 1357041600; // Jan 1 2013
  if(Serial.find(TIME_HEADER))
  {
     pctime = Serial.parseInt();
     return pctime;
     if( pctime < DEFAULT_TIME)
     { // check the value is a valid time (greater than Jan 1 2013)
       pctime = 0L; // return 0 to indicate that the time is not valid
     }
  }
  return pctime;
}
```

Teensy 3.6 Final Code

```
#include <TimeLib.h>
#include "ADC.h"
#include <SD.h>
```

```
// use of the fast adc routines for Teensy by Pedro Villanueva modified by Steven Parslow
ADC *adc = new ADC(); // adc object

void getDataLoop();
void SaveToFile();
const int ledPin = 13;
const int TrigPin = 12;
const int chipSelect = 4;
const int peaks = 60; // select number of peaks

int sensor[peaks][1001]; // define array to hold adc values for 'n' peaks
int trac;           // peak tracking variable
int PeakVal[peaks];     // array to hold the maximum of each peak

// Define the variables to read Real Time Clock and create filename
unsigned long intt;     // will hold the UTC time in seconds
char timbuf[10];       // will hold the 8 character conversion of intt
unsigned int test1;     // will hold the UTC number less the '15' at the start
int an;               // above bodge ok to September 2020
File dataFile;

void setup() {
   //set the input and output pin modes
   pinMode(ledPin, OUTPUT);
   pinMode(TrigPin, INPUT);
   pinMode(TrigPin, INPUT_PULLUP);

   // set the ADC converter resolution and speed setting
   adc->setResolution(16); // set bits of resolution
   adc->setAveraging(4);
   adc->setConversionSpeed(ADC_CONVERSION_SPEED::HIGH_SPEED);
   adc->setSamplingSpeed(ADC_SAMPLING_SPEED::VERY_HIGH_SPEED);

// start the serial monitor
   Serial.begin(9600);
// update time from real time clock
   setSyncProvider(getTeensy3Time);

  // look to see if the SD card is available
   if (!SD.begin(BUILTIN_SDCARD)) {
    for(int lq=0;lq<100;lq++){
     digitalWrite(ledPin, HIGH);   // quick flashing
     delay(50);                 // of LED
     digitalWrite(ledPin, LOW);    // if no SD card
     delay(50);     }           // is inserted
   }
```

```
//end of setup
}

 void loop() {
  trac=1;
   do{  Serial.println("in first do waiting for trigger");
       do{}while(digitalRead(TrigPin)==HIGH);
       Serial.println("got trigger");
      getDataLoop();
      Serial.println("got data");
      trac=trac+1;
     }while (trac<peaks);
     Serial.println("end of first do");
  SaveToFile();
  Serial.println("saved to file");
  simpLinReg();

// wait before allowing next measurement minimum 5*T1
  delay(10000);

// end of loop back to beginning again
}

void getDataLoop()
{
            for (an = 0; an < 1000; an++)
              sensor[trac][an] = adc->analogRead(0);
             // reads 1000 points across peak number 'trac'
}

void SaveToFile()
{ // note if you remove the card it needs a re-boot to work
  digitalWrite(ledPin, HIGH);   // led on whist file write
  time_t rawtime = now();     //update to instantaneous time
  intt= rawtime;              // assign values to unsigned int
  Serial.println(" intt is ");
  Serial.println(intt);
  test1=intt-1500000000;      // need to have 8 character file name and UTC is 10 characters
                         // the '15' at the front will be the same until mid 2020 so lose it
 sprintf(timbuf,"%u",test1);  // put time in seconds into character array called buffer
 Serial.println(" test1 is");
Serial.println(test1);
Serial.println("timbuf is");
Serial.println(timbuf);
  dataFile = SD.open(timbuf, FILE_WRITE);
Serial.println("file open");
   String dataString = "";
```

```
   delay(50);

   for(int a=1; a<peaks; a++) PeakVal[a]=0;
    if(dataFile)
    {   delay(50);
        Serial.println("in if(dataFile) loop");
        for(trac=1; trac<peaks; trac++)
          for (an = 0; an < 1000; an++)
           {
             dataString = String(sensor[trac][an]);
             Serial.println(dataString);
             dataFile.println(dataString);
             // work through the array to find the peak in each sweep
             if(PeakVal[trac]<sensor[trac][an])PeakVal[trac]=sensor[trac][an];
           }

     for(trac=1; trac<peaks; trac++)
     {
       dataString = String(PeakVal[trac]);
            Serial.println(dataString);
            dataFile.println(dataString);
     }

     }

Serial.println("data written");
  dataFile.close();
  Serial.println("now for the peaks");
   for(int a=1; a<peaks ;a++)
   {
    Serial.println(PeakVal[a]);
    }
Serial.println("file closed");
digitalWrite(ledPin, LOW);   // led off at end of file write
}


// stuff below updates the real time clock
time_t getTeensy3Time()
{
  return Teensy3Clock.get();
}
//  code to process time sync messages from the serial port
char TIME_HEADER[] = "T";
unsigned long processSyncMessage()
{
  unsigned long pctime = 0L;
```

```
  const unsigned long DEFAULT_TIME = 1357041600; // Jan 1 2013
  if(Serial.find(TIME_HEADER))
  {
    pctime = Serial.parseInt();
    return pctime;
    if( pctime < DEFAULT_TIME)
    { // check the value is a valid time (greater than Jan 1 2013)
      pctime = 0L; // return 0 to indicate that the time is not valid
    }
  }
  return pctime;
}

void simpLinReg()
{
  // initialize variables
  float xbar=0;
  float ybar=0;
  float xybar=0;
  float xsqbar=0;
  float locker[peaks];
  float mn[peaks];
  float lrCoef[2];

  Serial.println("Logged peak values are:");

  // calculations for natural log
   for (int i=0; i<peaks; i++)
  {
    locker[i] = log(PeakVal[i]);
    Serial.println(locker[i],4);
  }

  // create array for x values
  for (int i=0; i<peaks; i++)
  {
   mn[i] = i+1;
  }

  // calculations required for linear regression
   for (int i=1; i<peaks; i++)
  {
   xbar=xbar+mn[i];
   ybar=ybar+locker[i];
   xybar=xybar+mn[i]*locker[i];
   xsqbar=xsqbar+mn[i]*mn[i];
  }
```

```
 xbar=xbar/(peaks-1);
 ybar=ybar/(peaks-1);
 xybar=xybar/(peaks-1);
 xsqbar=xsqbar/(peaks-1);

 // print variables
 Serial.println("xbar, ybar, xybar and xsqbar variables are:");
 Serial.println(xbar);
 Serial.println(ybar);
 Serial.println(xybar);
 Serial.println(xsqbar);

 // simple linear regression algorithm
 lrCoef[0]=(xybar-xbar*ybar)/(xsqbar-xbar*xbar);
 lrCoef[1]=ybar-lrCoef[0]*xbar;

 // print gradient "lrCoef[0]" and intercept "lrCoef[1]"
 Serial.println("Linear fit gradient and intercept is:");
 Serial.println(lrCoef[0],6);
 Serial.println(lrCoef[1],6);}
```

Teensy 3.5 Code

```
const int ledPin = 13;
const int TrigPin = 12;
const int adcTrigPin = 11;
void setup() {
  analogWriteResolution(12);
  pinMode(ledPin, OUTPUT);
  pinMode(TrigPin, INPUT);
  pinMode(adcTrigPin, OUTPUT);
   pinMode(TrigPin, INPUT_PULLUP); //pull up on trigger input
    digitalWrite(adcTrigPin, HIGH);       // low shows generating waves
     digitalWrite(ledPin, HIGH);       // low shows generating waves
}

void loop() {
unsigned int n,m;
  digitalWrite(adcTrigPin, HIGH);       // low shows generating waves
   if (digitalRead(TrigPin))
     {
      digitalWrite(ledPin, HIGH);       // high shows waiting
      analogWrite(A21,0);//reset the DAC to save power
      }
    else {
       digitalWrite(ledPin, LOW);       // low shows generating waves
```

```
  for (m=0; m < 60; m++)
   {
     for (n=0; n < 4090; n++)
    {
      if(n==1000)
       {
         digitalWrite(adcTrigPin, LOW);       // low shows generating waves
       }
       if(n==1005)
       {
         digitalWrite(adcTrigPin, HIGH);       // low shows generating waves
       }
      delayMicroseconds(2);
      analogWrite(A21,n);
      delayMicroseconds(3);
      }
   }
   analogWrite(A21,0);//reset the DAC to save power
  }
}
```

APPENDIX B: PEER-REVIEWED ARTICLES

Analytical Methods

TECHNICAL NOTE

View Article Online
View Journal | View Issue

CrossMark click for updates

Cite this: *Anal. Methods*, 2017, **9**, 1681

A magnetic resonance disruption (MaRDi) technique for the detection of surface immobilised magnetic nanoparticles†

S. T. Parslow, T. Hughes-Riley, M. I. Newton and R. H. Morris*

Received 5th January 2017
Accepted 16th February 2017

DOI: 10.1039/c7ay00039a

rsc.li/methods

There are numerous assays that result in a surface with bound magnetic nanoparticles (MNP) whose number is proportional to the concentration of the analyte of interest. The techniques used to explore such assays are typically complex and costly. Since the presence of such MNP disrupts the pulsed magnetic resonance signal that would normally be detected from a fluid covering the surface, we present a measurement technique to quantify such assays. In this work we identify and characterise a suitable fluid for such measurements, namely 10 cSt viscosity PDMS oil of thickness 250 μm. We demonstrate that the T_2^{eff} relaxation time from the PDMS reduces as the proportion of the surface area covered with MNP increases. Most significant however, is a linear decrease in the signal amplitude from the PDMS as a function of MNP coverage. This is observed both for the integral over 4096 echoes and also in the first echo promising simplified console electronics for rapid measurements.

1. Introduction

An increasing number of assays result in a surface where the number of bound magnetic nanoparticles (MNP) is proportional to the concentration of analyte being measured.[1–5] These include colorimetric, refractive index change and optical reflectance methods for quantifying the number of bound MNP. Despite the fact that such MNP locally disrupt the magnetic field and hence the resulting magnetic resonance (MR) signal that would normally be detected,[6] magnetic resonance would normally be considered too complicated and expensive to offer a viable characterisation technique. MR spectrometers, used in pulsed MR experiments, are usually expensive because they are designed to operate over a wide range of frequencies and use different pulse sequences to give a range of measurement parameters. If a single liquid were to be used and a single parameter measured, this would significantly reduce the cost and complexity of the hardware required. In this work we sought to identify a suitable liquid, determine a suitable thickness of that liquid which would provide the maximum disruption and ease of measurement caused by the surface bound MNP and to identify an appropriate magnetic resonance parameter to measure.

2. Experimental methods

Acrylic test sticks were laser cut with wells etched into the sticks to hold the test liquid approximately 6 mm × 4 mm × 2 mm in length, width and height respectively giving a volume of approximately 50 μL. A probe was constructed using a set permanent magnets arranged in a Halbach geometry[7] which provided a static magnetic field of 507 mT (described in detail in the ESI material†). A CPMG sequence,[8] described and shown schematically in ESI material (S5 and S6† respectively), using the following parameters was applied to the coil using a commercial spectrometer (KEA^2, Magritek, NZ) running their proprietary software (Prospa, Magritek, NZ): echo time = 400 μs; number of echoes = 4096; number of averages = 128; pulse length = 11.7 μs, repetition time = 2 s. The appropriate detection liquid was determined by collecting data from a number of different candidates including various cooking oils, water and silicone oils. The collected echoes were transformed using the Lawson and Hanson non-negative least squares (NNLS) analysis function built into Prospa, producing a relaxation spectrum which provides the relative weighting of each relaxation component. For example, a mono-exponential T_2^{eff} decay will produce a single peak centred at its T_2^{eff} value, whilst a bi-exponential will have two peaks one centred on each of the components' T_2^{eff} values with the heights representing their relative magnitudes. A standard biotin–avidin method was used to immobilize MNPs on to a polystyrene surface that was cut to fit in the acrylic wells (details of immobilization procedure are also included in the ESI†). Prior to immobilization, some of the surfaces were laser engraved to remove different areas of the

School of Science and Technology, Nottingham Trent University, Clifton Lane, Nottingham, NG11 8NS, UK. E-mail: rob.morris@ntu.ac.uk; Tel: +44 (0) 115 8483315

† Electronic supplementary information (ESI) available. See DOI: 10.1039/c7ay00039a

biotin. The MNP used were BNF-starch-redF 100 nm (Micromod Partikeltechnologie GmbH) and the presence of immobilised MNP were confirmed using bright field images from a confocal microscope an example of which is shown in ESI Fig. S4.† The surface area covered by MNP was determined to be 26 ± 2% for the non-engraved biotin surfaces and less than 3% for the engraved surfaces due to non-specific binding.

3. Results and discussion

Both water and PDMS oil demonstrated a dominant (near single) relaxation component whereas cooking oils exhibited multiple relaxation components (see for example sunflower oil in Fig. 1) which is not desirable as the effect of the MNPs will be different for each peak, complicating the analysis. As PDMS was available in a number of different molecular weights (MW), a series of different values were assessed to determine the relationship between the samples T_2^{eff} relaxation value and the oil's MW, expressed in this case as viscosity with increasing MW providing increasing viscosity. It was found that the T_2^{eff} relaxation value increased as viscosity decreased (Fig. 2). As the T_2^{eff} relaxation time is expected to reduce with the presence of the MNP,[6] the 10 cSt viscosity oil provided a sufficiently long starting T_2^{eff} of 700 ms and was of sufficiently low viscosity to flow easily filling the test stick, so was selected as the test liquid.

Different thicknesses of the 10 cSt PDMS oil layer were used to investigate the thinnest layer that would provide a sufficiently reproducible T_2^{eff} measurement, as this would maximise the effect of any surface bound MNP (Fig. 3). Values below 125 μm, corresponding to a volume of 3 μL of PDMS, showed significant increase in scatter of the data due to the limited volume fraction of the coil filled with MR liquid sample (known as the fill factor). Surface roughness of the sample holder required a slightly larger volume than this to provide reliable measurements of

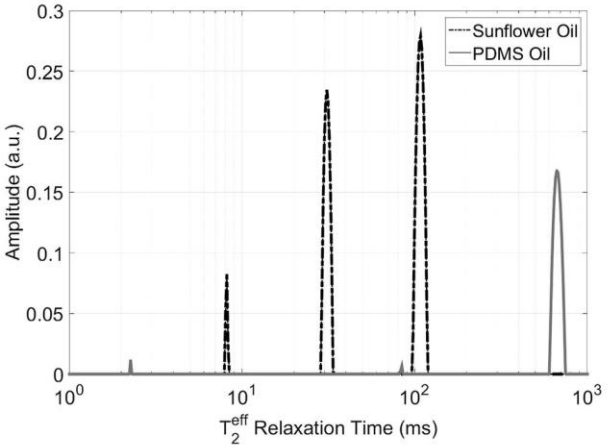

Fig. 1 A relaxation spectrum for 10 cSt PDMS oil and sunflower oil showing the different T_2^{eff} components. The PDMS oil shows one dominant and two negligible peaks, whereas the sunflower oil has three significant relaxation components.

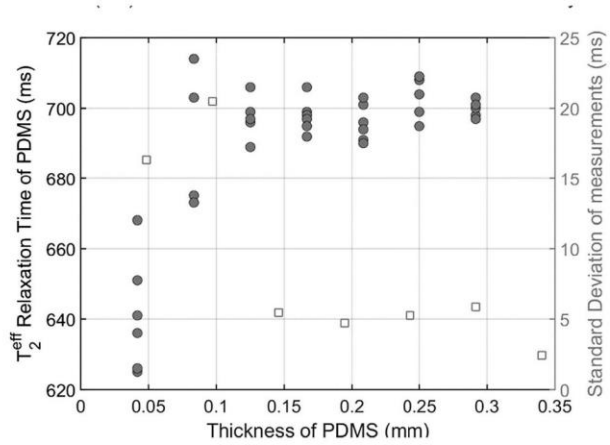

Fig. 3 Repeated measurements of T_2^{eff} (filled circles) and the standard deviation of these measurement (open squares) for different thicknesses of 10 cSt viscosity PDMS oil showing that is the measurements are unreliable below 125 μm thickness.

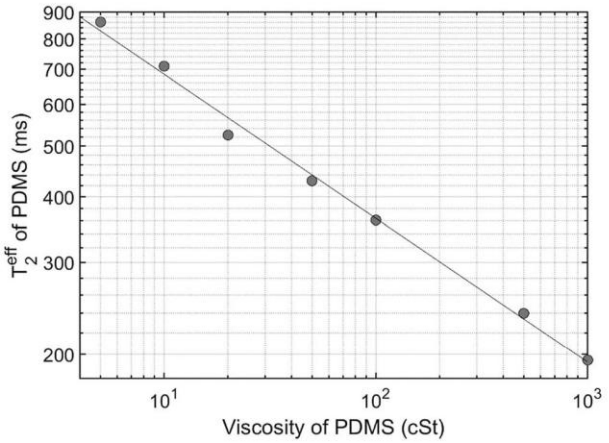

Fig. 2 A logarithmic plot of the T_2^{eff} relaxation time of PDMS oil as a function of viscosity.

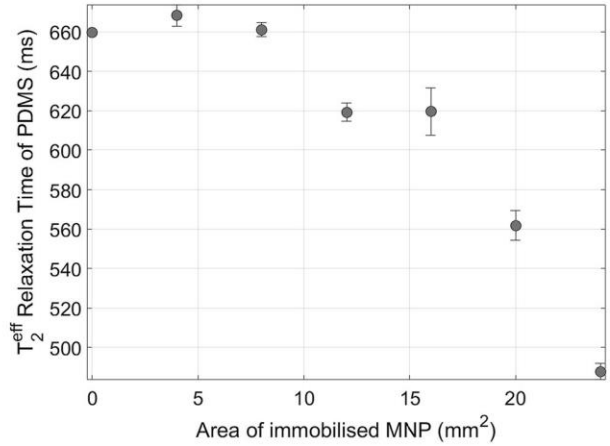

Fig. 4 The T_2^{eff} relaxation time of the 10 cSt viscosity PDMS oil as function of the area of immobilised MNP for a 250 μm thick layer.

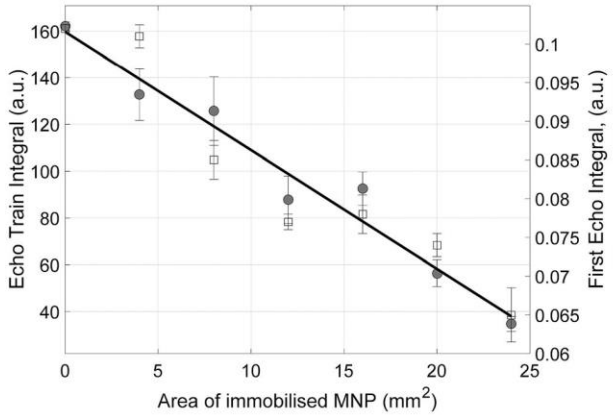

Fig. 5 The integral of 4096 echoes (filled circles, left axis) and the integral of the first echo (open squares, right axis) as a function of the function of the area of immobilised MNP. The regression lines of both data sets lie on top of each other for these scales although their parameters are different.

signal degradation due to the presence of MNP so a thickness of twice the minimum value was used giving a total fluid volume of 6 μL. The sample sticks containing different fractions of MNP coverage were measured to determine the value of T_2^{eff} and also the signal intensity using the integral of the echoes. In Fig. 4 we show the non-linear reduction in T_2^{eff} as a function of the increase in the proportion of the surface area covered with MNP. From this we can see that there is little effect on T_2^{eff} for coverage of less than 7% but above this T_2^{eff} reduces. In Fig. 5, a linear decrease in the signal amplitude, taken as the integral of 4096 echoes, as a function of the percentage of the surface area covered in MNP is shown with a gradient of 5 au mm^{-2}. This same trend was also apparent for the integral first echo alone (often incorrectly referred to as the Hahn echo) also shown in Fig. 5 although it is less sensitive with a gradient of 0.001 au mm^{-2}.

4. Conclusion

We have demonstrated that the number of surface bound MNP is directly proportional to the intensity (integral) of one or more spin echoes. A three 'well' system that provides one reference well containing only oil, one reference well with a known MNP surface coverage and one well with the unknown coverage, most usefully as a function of analyte binding, would allow self-consistent determination of the amount bound. The wells with the oil alone and the known coverage give the possibility of straight line calibration allowing the unknown coverage to be determined independently of environmental parameters for example, this would remove problems associated with long term temperature drift in the permanent magnets which may affect the signal. The ability to determine the binding fraction from the integral of one or more echoes, with the increasing publication of simplified spectrometer designs,[9,10] makes magnetic resonance a viable technique for determining the quantity of surface bound MNP.

Acknowledgements

STP gratefully acknowledges Nottingham Trent University for funding under the Vice Chancellors Bursary Award.

References

1 C. Esseghaier, G. A. R. Y. Suaifan, A. Ng and M. Zourob, *J. Biomed. Nanotechnol.*, 2014, **10**, 1123.
2 X. Hun, Y. Xu and X. Luo, *Microchim. Acta*, 2015, **182**, 1669.
3 G. A. R. Y. Suaifan, C. Esseghaier, A. Ng and M. Zourob, *Analyst*, 2013, **138**, 3735.
4 C. Esseghaier, A. Ng and M. Zourob, *Biosens. Bioelectron.*, 2013, **41**, 335.
5 S. Wignarajah, G. A. R. Y. Suaifan, S. Bizzarro, F. J. Bikker, W. E. Kaman and M. Zourob, *Anal. Chem.*, 2015, **87**, 12161.
6 A. Hall, V. J. Mundell, C. Blanco-Andujar, M. Bencsik, G. McHale, G. M. I. Newton and G. W. V. Cave, *Chem. Commun.*, 2010, **46**, 2420.
7 K. Halbach, *Nucl. Instrum. Methods*, 1980, **169**, 1.
8 S. Meiboom and D. Gill, *Rev. Sci. Instrum.*, 1958, **29**, 688.
9 N. Sun, Y. Liu, L. Qin, H. Lee, R. Weissleder and D. Ham, *Solid-State Electron.*, 2013, **84**, 13.
10 H.-Y. Chen, Y. Kim, P. Nath and C. Hilty, *J. Magn. Reson.*, 2015, **255**, 100.

MRC

Published online in Wiley Online Library: 24 April 2017

(wileyonlinelibrary.com) DOI 10.1002/mrc.4594

Transient effect determination of spin–lattice (TEDSpiL) relaxation times using continuous wave NMR

Introduction

The phenomenon of nuclear magnetic resonance (NMR) was first demonstrated as continuous wave (CW)-NMR[1–7], which become unpopular due to the advantages offered by pulsed NMR. Conceptually more simple, but more challenging to reliably determine relaxation parameters from, for half a century CW-NMR has virtually been consigned to the undergraduate laboratory and magnetometers. In a typical CW-NMR system, a sample is placed in a coil in a static magnetic field. The coil forms part of an oscillator circuit, and sweep coils are used to vary the static field by a small amount. As the swept magnetic field corresponds to the Larmor frequency, the amplitude of the oscillator output rapidly falls, providing a shape and signature characteristic of the NMR spin–spin relaxation time T_2. CW-NMR has not been a particularly active topic of research for more than 50 years due to the advantages of pulsed NMR for measuring relaxation times. Some interest in the electronic development, in particular the development of oscillator circuits,[8–10] has taken place, and CW-NMR is used as the basis of sensitive magnetometers.[11–13] CW-NMR has also enjoyed some success as an imaging tool for use on samples with very short T_2 relaxation times.[14,15] Commercial CW-NMR systems can be readily purchased although these are primarily used as teaching tools. In a 1981 article,[16] Firth describes a technique to directly observe the spin–lattice relaxation time T_1 by using a CW-NMR system following recovery from saturation. In our work, we have observed, using high-speed data capture, that simply moving from static field only, to static field plus sweep coils, in a commercial CW-NMR system resulted in a similar settling time related to the spin–lattice relaxation time. We corroborate our measurements against pulsed magnetic resonance by using the same magnet and coil and provide a means by which the CW system, with the aid of two calibration samples, can be used to determine the spin–lattice relaxation times of unknown samples.

Experimental

A commercial CW-NMR setup from LD Didactic GmbH (Hürth Germany, www.ld-didactic.de) (Fig. 1) was used for all experiments [consisting of NMR supply unit (514 602); NMR probe (514 606) including sample coil, sweep coils, and yoke; U-core (562 11); and two electromagnet coils (562 131)]. The system was designed to operate between 16.0 and 19.5 MHz by varying the current supplied to the electromagnet coils. The high current required to operate the magnet in that field range, however, caused significant heating of the samples during measurements affecting the value of T_1. This was overcome by using an additional 1 m of coaxial cable between sample coil and oscillator causing the oscillator to operate at around 12 MHz and requiring only 2.2 A to generate the static magnetic field of the correct magnitude. Although the sweep coils would normally be powered by the NMR supply unit, the analogue output of a data acquisition card (NI USB-6211, National Instruments, TX, USA) was fed to a power amplifier built from a 2N3055H power transistor and LM358N buffer amplifier providing a gain of five. Data were collected by using the same data acquisition device operating at 500 kS/s integrated with a Labview (http://www.ni.com/labview) program to generate appropriate waveforms and collect the resulting NMR signal. The analogue output of the USB-6211 produced a saw-tooth voltage waveform of maximum amplitude 1.25 V and a frequency of 50 Hz in 5-s bursts with a recovery time delay between bursts. All data were collected without changing the amplitude setting on the NMR unit or the current supplied to the static magnetic field coils. The samples used consisted of a range of polydimethylsiloxane oils of different viscosities, from 2 to 30 000 cS, and different concentrations of copper sulfate solutions, from 5 to 750 μM, giving T_1 values in the range of 0.5 to 2 s. The T_1 values were measured on the same electromagnet (with the same current) and RF coil, with additional tuning and matching capacitors, using a pulsed NMR spectrometer (Kea^2, Magritek, NZ) running a stock inversion recovery pulse sequence with Carr–Purcell–Meiboom–Gill echo detection.

Results and Discussion

Figure 2 shows the NMR signal for a single sweep with the main peak followed by the characteristic 'wiggles' and a subsequent smaller peak on the fly-back of the saw-tooth wave applied to the sweep coils, which is shown in grey. A Labview VI produces the modulus of the data before finding the maximum value within each sweep. An example of the result of this process is shown in Fig. 3. The curve fitting routine in Labview then performs an exponential fit before writing out the exponential coefficients [amplitude, decay time (T_x) and noise] to a file. Before repeating the experiment, the system must be allowed to re-equilibrate. The time allowed for this to take place is known as the recovery time. The minimum recovery time required was determined experimentally by measuring a100 μM aqueous copper sulfate solution 50 times for recovery times from 1 to 50 s (data not shown). The standard deviation in the exponential fit was high for the short recovery times but reduced rapidly as the time was increased. The plateau was found at 15 s. To allow for a safe margin of error, 20 s was chosen for

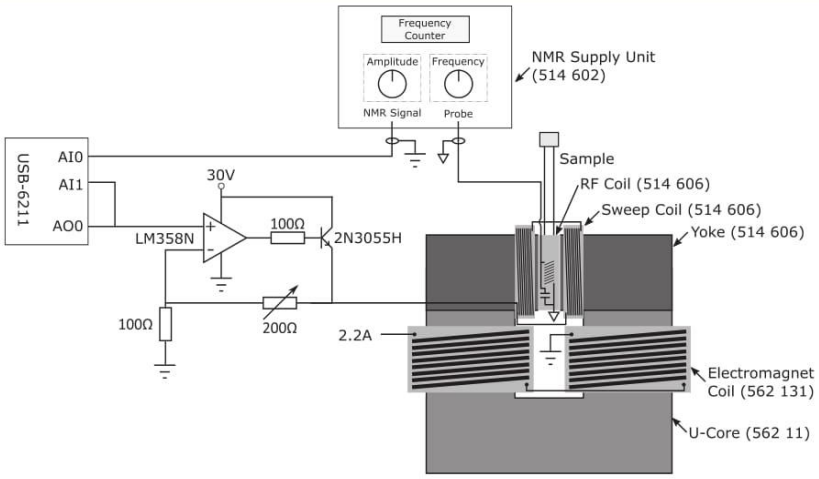

Figure 1. The modified commercial continuous wave equipment.

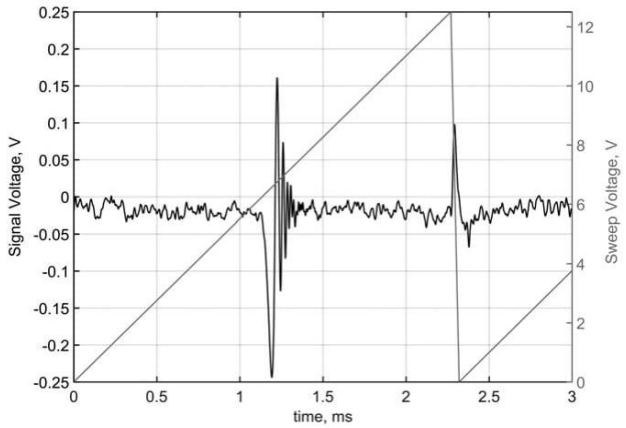

Figure 2. The NMR output signal (Left axis, Black) for a single sweep of the saw-tooth waveform (Right axis, Grey) applied to the sweep coils also showing a smaller peak as a result of the fly-back.

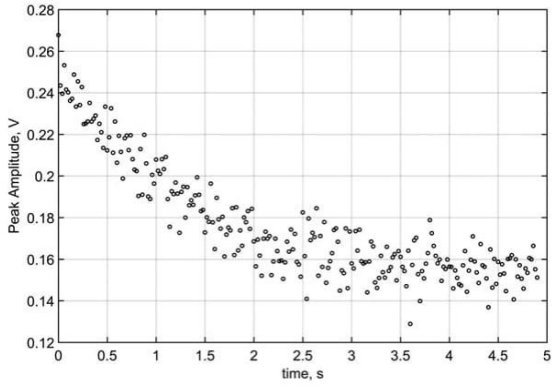

Figure 3. The peak amplitude of the NMR signal for each sweep of the saw-tooth shown for a five second burst. The Labview program fits an exponential to these data to give a characteristic time referred to here as Tx.

use in all subsequent measurements. Figure 4 shows the T_1 relaxation time as measured by the pulsed system plotted against the exponential fit decay time from the CW-MR data. While some

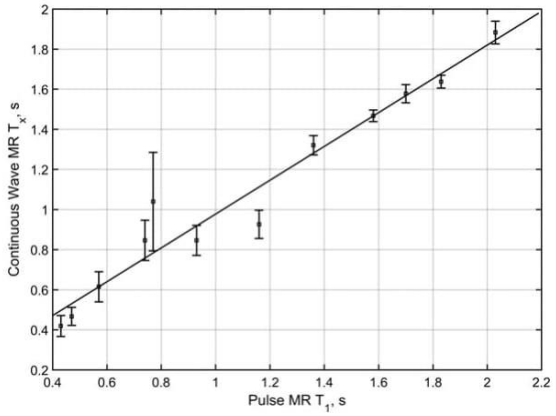

Figure 4. The value to Tx plotted against the value of T1 as determined by pulsed NMR.

scatter can be seen, there is a clear linear correlation between the two. It should be noted that the T_x value we determine is not the same as the value of T_1 in seconds. There are a number of parameters which change the gradient of this relationship including the amplitude setting of the oscillator. For the data presented, we used the central 'sweet spot' where all the samples presented a sustained oscillation without changing the amplitude setting. As the relationship between T_1 and T_x is linear, unknown measurements are easily collapsed to a gradient of 1 by using two reference samples (one high and one low T_1 values) to provide the calibration factor.

Conclusion

In this work, we have revisited a qualitative MR relaxation technique with modern data capture equipment to investigate the transient response that occurs following the start of a field sweep in a commercial CW-NMR system. We have demonstrated that such a system can provide a method for determination of the spin–lattice relaxation time T_1 when a measurement commences with two known calibration samples. This work will provide additional learning opportunities for students using educational CW-NMR

systems and may open up new industrial quality control applications where the measurement of T_1 brings useful information but the use of pulsed NMR was previously considered too expensive.

Acknowledgement

The authors wish to thank Nick Howard for producing the amplifier circuit used in this work.

Robert H. Morris,* Nur Mostafa, Steven Parslow and Michael I. Newton

School of Science and Technology, Nottingham Trent University, Clifton Campus, Clifton Lane, Nottingham, UK, NG11 8NS

*Correspondence to: Robert H. Morris, School of Science and Technology, Nottingham Trent University, Clifton Campus, Clifton Lane, Nottingham, UK, NG11 8NS. E-mail: rob.morris@ntu.ac.uk

Received: 25 January 2017; Revised: 17 March 2017; Accepted: 23 March 2017

References

[1] E. M. Purcell, H. C. Torrey, R. V. Pound. *Phys. Rev.* **1945**, *69*, 37–38. https://doi.org/10.1103/PhysRev.69.37.

[2] F. Bloch. *Phys. Rev.* **1946**, *70*, 460–474. https://doi.org/10.1103/PhysRev.70.460.

[3] F. Bloch, W. W. Hansen, M. E. Packard. *Phys. Rev.* **1946**, *70*, 474–485. https://doi.org/10.1103/PhysRev.70.474.

[4] B. A. Jacobson, R. K. Wangsness. *Phys. Rev.* **1948**, *73*, 942–946. https://doi.org/10.1103/PhysRev.73.942.

[5] E. M. Purcell. *Science* **1948**, *107*, 433–440. https://doi.org/10.1126/science.107.2783.433.

[6] N. Bloembergen, E. M. Purcell, R. V. Pound. *Phys. Rev.* **1948**, *73*, 679–712. https://doi.org/10.1103/PhysRev.73.679.

[7] E. Fukushima, S. B. W. Roeder*Experimental Pulse NMR*, Westview Press, Colorado, **1981**.

[8] R. V. Pound, W. D. Knight. *Rev. Sci. Instrum.* **1950**, *21*, 219–225. https://doi.org/10.1063/1.1745537.

[9] F. N. H. Robinson. *J. Sci. Instrum.* **1959**, *36*, 481–487. https://doi.org/10.1088/0950-7671/36/12/301.

[10] K. J. Wilson, C. P. G. Vallabhan. *Meas. Sci. Technol.* **1990**, *1*, 458–460. https://doi.org/10.1088/0957-0233/1/5/015.

[11] H. R. Opplinger, P. Schmid, H. H. GmHard. *J. Sci. Instrum.* **1965**, *42*, 865–868. https://doi.org/10.1088/0950-7671/42/12/309.

[12] K. Weyand. *IEEE T. Instrum. Meas.* **1989**, *38*, 410–414. https://doi.org/10.1109/19.192317.

[13] S. Begus, D. Fefer. *Meas. Sci. Technol.* **2007**, *18*, 901–906. https://doi.org/10.1088/0957-0233/18/3/045.

[14] A. J. Fagan, G. R. Davies, J. M. S. Hutchison, F. P. Glasser, D. J. Lurie. *J. Magn. Reson.* **2005**, *176*, 140–150. https://doi.org/10.1016/j.jmr.2005.05.022.

[15] A. J. Fagan, G. R. Davies, J. S. M. Hutchison, D. J. Lurie. *J. Magn. Reson.* **2003**, *163*, 318–324. https://doi.org/10.1016/S1090-7807(03)00128-9.

[16] L. D. Firth. *Eur. J. Phys.* **1983**, *3*, 10–13. https://doi.org/10.1088/0143-0807/3/1/003/.

proceedings

MDPI

Proceedings

A Microcontroller System for the Automation of Transient Effect Determination of the Spin-Lattice Relaxation Time Using Continuous Wave NMR †

Steven T. Parslow, Michael I. Newton * and Robert H. Morris

School of Science and Technology, Nottingham Trent University, Clifton Lane, Nottingham NG11 8NS, UK; steven.parslow2008@my.ntu.ac.uk (S.T.P.); rob.morris@ntu.ac.uk (R.H.M.)

* Correspondence: Michael.newton@ntu.ac.uk; Tel.: +44-115-848-3365

† Presented at the 5th International Electronic Conference on Sensors and Applications, 15–30 November 2018; Available online: https://ecsa-5.sciforum.net.

Published: 6 November 2018

Abstract: A simple transient effect method for the determination of the spin-lattice relaxation time using continuous wave NMR (TEDSpiL) with a marginal oscillator was recently reported (doi:10.1002/mrc.4594). Such a system measures a parameter called T_x that is related to T_1 and allows T_1 to be determined with the aid of calibration samples. For such a system, the process of making the T_x measurement does not require variable parameters and so is ideal for implementing in microcontroller code. In this article, we demonstrate that TEDSpiL may be automated using two microcontrollers from the Teensy family to make a low power and portable system.

Keywords: continuous wave NMR; microcontroller; teensy; TEDSpiL; spin lattice relaxation time; T_1

1. Introduction

Nuclear magnetic resonance (NMR) has many applications, from the chemical fingerprints of NMR spectroscopy [1] to the whole body magnetic resonance imaging (MRI) scanners found in many hospitals [2]. Two of the parameters that can be used in the production of MRI images are the spin-lattice (T_1) and spin-spin (T_2) relaxation times, and measurements of these have been used in a wide variety of sensor applications that may use permanent magnets and less expensive electronics [3–5]. Most applications use pulsed NMR for these measurements; however, continuous wave (CW), which was the predecessor to pulsed, is conceptually simpler and has simpler electronics but is often more difficult to implement and so fell out of favor. Recent advances in permanent magnet technology and speed of low-cost electronics have sparked some interest in the topic and the electronics have been recently reviewed [6]. A simplified view of NMR considers the intrinsic nuclear magnetic moments of certain nuclei to be like microscopic bar magnets that tend to orientate in a generally aligned manner with or opposed to the presence of a strong magnetic field (B_0). Radio frequency (rf) radiation can be absorbed at a frequency that satisfies the Larmor condition $\omega = \gamma B_0$ (where ω is the angular frequency and γ is the gyromagnetic ratio which is a constant for a given nucleus) corresponding to the energy difference between the two states. In CW-NMR, either the frequency of the rf can be fixed and the magnetic field swept through the resonance condition, or the magnetic field is held constant and the frequency of the rf changes. Where the field is swept, an alternative strategy is to use a marginal oscillator where the oscillation amplitude dips as it passes through resonance [7,8]. Look and Locker [9] demonstrated that there is a transient effect when the sweep of the magnetic field is initiated and that this may be used to determine the value of T_1. More recently, a simple variation using a marginal oscillator and calibration samples was presented, which is referred to as the

transient effect determination of the spin-lattice relaxation time using continuous wave NMR, or TEDSpiL [10]. In this work we demonstrate that TEDSpiL may be automated using two microcontrollers from the Teensy family.

2. Materials and Methods

A schematic diagram of the continuous wave system is shown in Figure 1. The sample is placed in a coil which forms part of a marginal oscillator tank circuit. For convenience, we use a commercial marginal oscillator operating from around 14 MHz to 21 MHz [11]; however, there have been many different marginal oscillator circuits published, which were reviewed recently [6]. The coil used, also produced by LD Didactic as part of their NMR probe bar (514–606), is placed in the fixed magnetic field with sweep coils that allow the field to be swept about the resonance value. The fixed field can be produced by using Neodymium Iron Boron (NdFeB) magnets, as shown in Figure 1, or by electromagnet coils; however, the latter do draw significant current and cause elevated sample temperatures. A digital to analogue converter on a Teensy 3.5 [12] microcontroller is used to generate 100 cycles of a voltage ramp which are amplified using a power amplifier built from a 2N3055H power transistor and LM 358N buffer amplifier [10] and providing a gain of five, before driving the sweep coils (part of the 514–606). The oscillator frequency is adjusted such that the resonance occurs at the center of the ramp. The ramp is started using a push button attached to a digital input (pin 12) on the Teensy 3.5 microcontroller and a digital output (pin 11) is used to trigger a Teensy 3.6 [13] to make measurements of the marginal oscillator output after it has been amplified by a simple inverting op-amp (MCP6002) with a 1 kΩ input resistor and a 10 kΩ feedback resistor, giving a gain of −10. A liquid crystal display (LCD) is attached to pin 10 of the Teensy 3.5 to display the calculated value of T_x. The code for the Teensy 3.5 is shown in Supplementary S1.

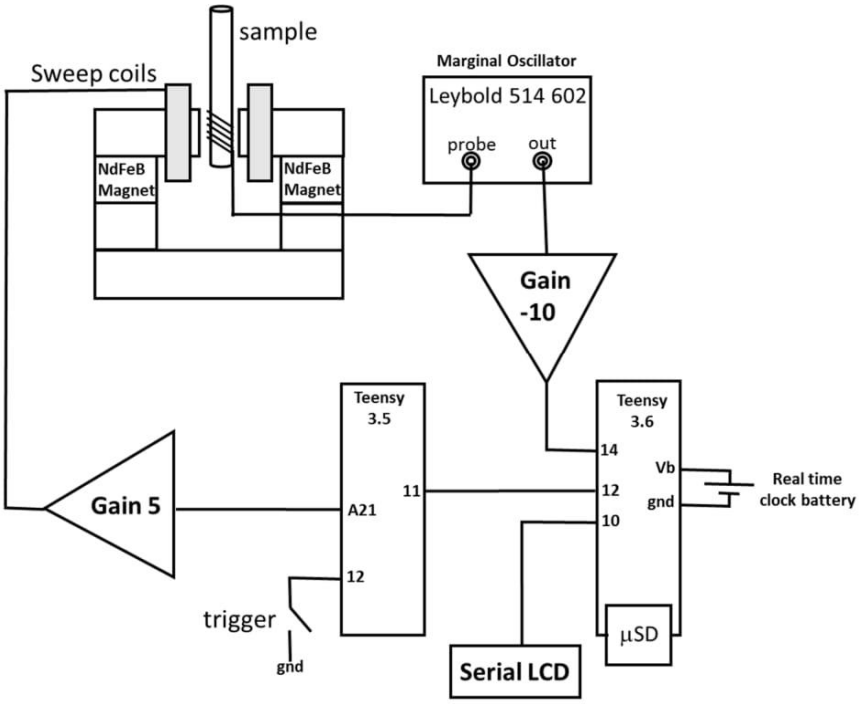

Figure 1. Schematic diagram of the experimental arrangement. Only the power (4.5V to 'Vin' pins) and ground (power ground to pin 'GND' and analogue input ground to 'Analog GND') connections have been left off the Teensy circuits, and the gain −10 amplifier is an inverting op-amp.

The Teensy 3.6 is a 32-bit 180 MHz ARM Cortex-M4 processor with floating point unit, 256 Kbytes of RAM, and 1024 Kbytes of flash memory, including an on-board microSD card holder. It costs less than US$30. It contains two analogue to digital converters (ADC) with a usable resolution of 13 bits. Much of the material for the Teensy was developed open source by Paul Stoffregen and his

team at pjrc.com; however, there is an implementation library for the ADC that was created by Pedro Villanueva [14] which allows the full power of the ADC to be utilized

For maximum speed, data are saved into an array in memory, and the maximum array size for 16-bit sample data is around 64,000 data points. This is not sufficient to capture the whole of the data for 60 sweeps at 40 Hz, and a lower sample rate may not clearly identify the peak value. To allow for this, the Teensy 3.5 provides a trigger pulse to the Teensy 3.6 a quarter of the way up the ramp sweep so that only the 1000 points around the peak are captured to an array in memory. It is then a straightforward loop to find the maximum value within those data to give the peak value which is stored in a separate array of peak values.

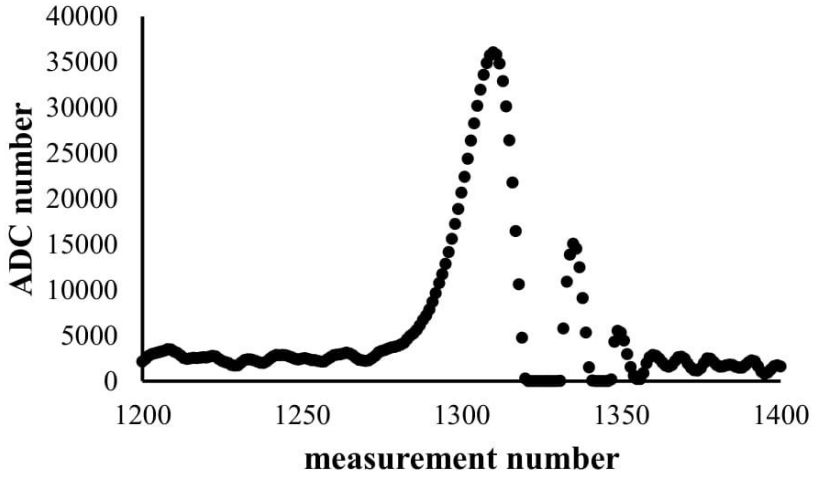

Figure 2. The number returned from the Teensy 3.6 ADC (analogue to digital converter) from the amplified marginal oscillator signal for a single magnetic field sweep. This demonstrates that the Teensy ADC is capable of accurately capturing the peak amplitude.

The Teensy 3.6 code then carries out a simple least squares fit on the natural log of the peak values, and the gradient gives a value for T_x, which is displayed on the serial LCD display. The time from pressing the trigger to the display of T_x is less than five seconds, and the system then waits for a further ten seconds before the trigger can be pressed again to allow the sample to equilibrate away from the resonant value of magnetic field. All the data from the arrays and the peak values are stored on the onboard microSD card with the real time clock being used to generate a file name which is the last 8 digits of the UNIX time stamp of when the measurement was made. It should be noted that the Teensy 3.6, unlike the 3.5, is not 5 V tolerant, so the amplifier is supplied with only 3 V from two 1.5 V batteries, and both the Teensy 3.5 and 3.6 are supplied with 4.5 V from three 1.5-volt batteries. In our circuit, both amplifier and Teensy share batteries to save weight, and the amplifier supply is 'tapped' off.

3. Results

Figure 2 shows the number returned from the Teensy 3.6 ADC from the amplified marginal oscillator signal for a single magnetic field sweep. With a sampling speed of around 160 kSample/second, this demonstrates that the Teensy ADC is capable of accurately capturing the peak amplitude. Note that the positive going "wiggles'" that are common in this type of system [6] are also visible, but as we are only interested in the peak value, no offset is provided to the amplifier to capture the negative going part of the "wiggles". By triggering the 3.6 to capture partway through the sweep ramp, it is easily possible to capture up to 60 peaks with the available RAM, but only around 25 peaks are required to get a reasonable linear fit to provide a value for T_x; the first five values are also discarded.

Figure 3 shows a typical example for a sample of water of natural log of the peak amplitude from the amplified marginal oscillator signal as a function of time for peaks 5 to 25. Note that the scatter in the data increases as the marginal oscillator peak amplitude tends towards the equilibrium value, so including peaks beyond the 25th does not improve the T_x measurement. In Figure 4, we show a set of T_x values as a function of the concentration of copper sulphate, which is often used as a standard test set of T_1 values in pulsed NMR; the change is consistent with data reported for pulsed NMR [15,16].

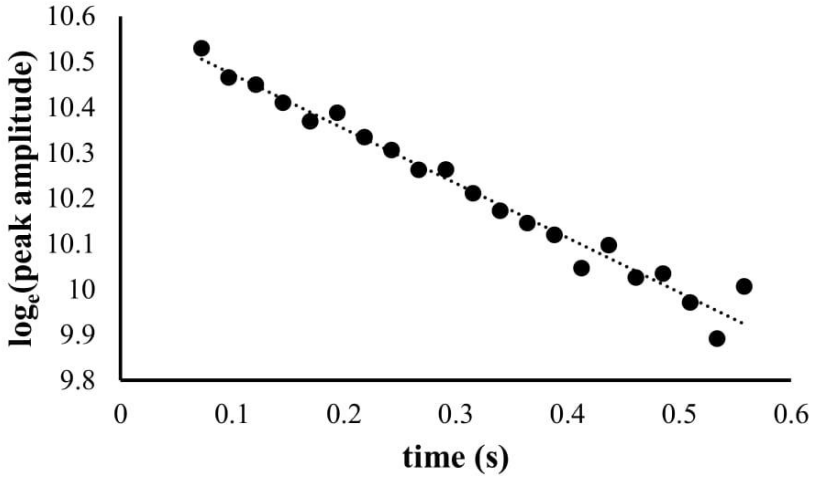

Figure 3. Typical example for water of the natural log of the peak amplitude from the amplified marginal oscillator signal as a function of time for peaks 5 to 25. The gradient of the linear fit, shown as the dotted line, gives a value for T_x.

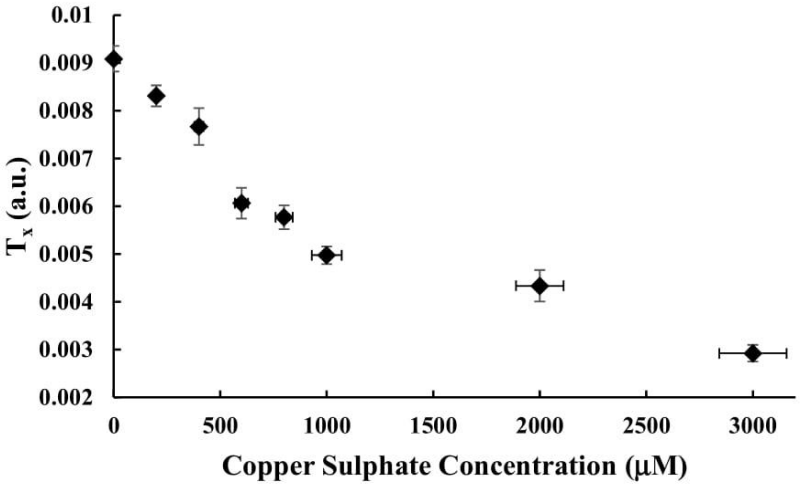

Figure 4. T_x values as a function of concentration of copper sulphate in water.

4. Discussion

The electronics, commonly referred to as the console, for low field pulsed NMR systems typically cost in excess of $20k as they are designed to be wide band and highly programmable spectrometers. The process of making T_1 measurements with such a pulsed system usually uses recovery sequences that will typically take many minutes to give a single T_1 value. Whilst the T_x value is not a direct equivalent to T_1, there are applications where the use of T_x may provide a cost-effective measurement solution. One such application may be to sample the outlet water from a constructed wetland

treatment bed for coal mine drainage water. Such water often contains iron oxide, which is a known T_1 contrast agent, and the presence of a significant amount of iron oxide in the water would indicate that a constructed wetland bed is no longer functioning correctly and that remediation work is required. As there are environmental, and possibly financial, consequences for clogged beds discharging untreated water, the measurement system reported in this article could form the basis of an appropriate monitoring system.

Author Contributions: Conceptualization and Methodology, M.I.N. and R.H.M.; Software, M.I.N. and S.T.P.; Investigation, M.I.N. and S.T.P.; Writing—Original Draft Preparation, M.I.N.; Writing—Review & Editing, R.H.M. and S.T.P.

Funding: This research received no external funding

Conflicts of Interest: The authors declare no conflict of interest.

References

1. Weber, U.; Thiele, H. *NMR Spectroscopy: Modern Spectral Analysis*, 1st ed.; Wiley VCH: Weinheim, Germany, 1998; ISBN-10 3527288287.
2. Dale, B.M.; Brown, M.A.; Semelka, R.C. *MRI: Basic Principles and Applications*; Wiley-Blackwell: Hoboken, NJ, USA, 2015; ISBN-10 1119013054.
3. Blumich, B.; Perlo, J.; Casanova, F. Mobile single-sided NMR. *Prog. Nucl. Magn. Reson. Spectrosc.* **2008**, *52*, 197–269, doi:10.1016/j.pnmrs.2007.10.002.
4. Blümich, B. Introduction to compact NMR: A review of methods. *Trends Anal. Chem.* **2016**, *83*, 2–11, doi:10.1016/j.trac.2015.12.012.
5. Kirtil, E.; Cikrikci, S.; McCarthy, M.J.; Oztop, M.H. Recent advances in time domain NMR & MRI sensors and their food applications *Curr. Opin. Food Sci.* **2017**, *17*, 9–15, doi:10.1016/j.cofs.2017.07.005.
6. Newton, M.I.; Breeds, E.A.; Morris, R.H. Advances in Electronics Prompt a Fresh Look at Continuous Wave (CW) Nuclear Magnetic Resonance (NMR). *Electronics* **2017**, *6*, 89, doi:10.3390/electronics6040089.
7. Robinson, F.N.H. A high field nuclear magnetic resonance probe using transistors. *J. Sci. Instrum.* **1965**, *42*, 653–654, doi: 10.1088/0950-7671/42/8/344.
8. Wilson, K.J.; Vallabhan, C.P.G. An improved MOSFET-based Robinson oscillator for NMR detection. *Meas. Sci. Technol.* **1990**, *1*, 458–460, doi:10.1088/0957-0233/1/5/015.
9. Look, D.C.; Locker, D.R. Nuclear Spin-Lattice Relaxation Measurements by Tone-Burst Modulation. *Phys. Rev. Lett.* **1968**, *20*, 987–989, doi:10.1103/PhysRevLett.20.987.
10. Morris, R.H.; Mostafa, N.; Parslow, S.; Newton, M.I. Transient effect determination of spin–lattice (TEDSpiL) relaxation times using continuous wave NMR. *Magn. Reson. Chem.* **2017**, *55*, 853–855, doi:10.1002/mrc.4594.
11. LD Didactic GmbH, Hürth, Germany part number 514–602 http://www.ld-didactic.de/(accessed on 22 January 2019).
12. Teensy USB Development Board 3.5. Available online: https://www.pjrc.com/store/teensy35.html (accessed on 19 June 2018).
13. Teensy USB Development Board 3.6. Available online: https://www.pjrc.com/store/teensy36.html (accessed on 19 June 2018).
14. Teensy 3.x/LC ADC Implementation. Available online: https://github.com/pedvide/ADC (accessed on 19 June 2018).
15. Van Geet, A.L.; Hume, D.N. Measurement of Proton Relaxation Times with a High Resolution Nuclear Magnetic Resonance Spectrometer. Progressive Saturation Method. *Anal. Chem.* **1965**, *37*, 979–983, doi:10.1021/ac60227a008.
16. Thangavel, K.; Saritas, E.U. Aqueous paramagnetic solutions for MRI phantoms at 3 T: A detailed study on Relaxivities. *Turk. J. Electr. Eng. Comput. Sci.* **2017**, *25*, 2108–2121, doi:10.3906/elk-1602-123.

Received: 30 September 2018 | Revised: 22 January 2019 | Accepted: 25 January 2019

DOI: 10.1002/mrc.4845

SPECIAL ISSUE RESEARCH ARTICLE

WILEY

A preliminary study of milk powder hydration using TEDSpiL continuous wave NMR

Steven T. Parslow | Najlaa K. Almazrouei | Michael I. Newton | Elizabeth R. Dye | Robert H. Morris

School of Science and Technology, Nottingham Trent University, Nottingham, UK

Correspondence
Michael I. Newton, School of Science and Technology, Nottingham Trent University, Clifton Lane, Nottingham NG11 8NS, UK.
Email: michael.newton@ntu.ac.uk

Funding information
Nottingham Trent University; Ministry of Higher Education and Scientific Research (MOHESR) in the United Arab Emirates; Dubai Health Authority (DHA)

Abstract

Moisture content of foodstuffs are typically assessed by Titration or Near Infrared Spectroscopy, which are labour-intensive as a manual measurement or costly when automated. Magnetic resonance offers a method for moisture evaluation but is also normally costly. In this work, we revisit Look and Locker's "Tone Burst" experiment with a marginal oscillator to evaluate moisture content of powdered–skimmed milk subjected to increased humidity. We refer to this technique as the Transient Effect Determination of Spin–Lattice (TEDSpiL) relaxation times. Moisture content in the samples ranged from 0–12% as determined from the weight gained by the dry powder when re-suspended in water to reach a concentration of 40% w/v. The relaxation properties of re-hydrated samples were measured with a CW NMR sensor. Solutions made up from powders with a higher retained moisture content provided lower measured relaxation values providing a method of measuring the moisture content of the powder. This technique provides a moisture measurement in under 5~s compared with several minutes for the equivalent pulsed method using low-field hardware.

KEYWORDS

continuous wave, hydration, milk powder, moisture content, spin–lattice relaxation

1 | INTRODUCTION

The shelf life of milk can be extended by partial evaporation of the liquid fraction before spray drying into a vacuum vessel or roto drying thus reducing the biological activity. The resulting powder is hygroscopic by nature and will readily absorb atmospheric moisture from its surroundings, which will promote microbial growth and reduce the overall life and quality of the powder. The primary goal of storage is to limit the availability of atmospheric moisture. There are numerous methods for the measurement of water content in food[1–6] such as Karl Fischer Titration and near-infrared spectroscopy though these are challenging to automate, labour-intensive, or require significant cost investment in equipment. As water contains a large amount of hydrogen, magnetic resonance (MR) offers a useful tool for moisture measurement. Traditionally, MR is often an expensive technique although increasingly low-cost hardware is becoming available for such measurements.

Relaxation parameters in nuclear magnetic resonance (NMR) are often measured using pulsed echo sequences such as inversion recovery for T1 and Carr-Purcell-Meiboom-Gill (CPMG) for T2. Inversion recovery sequences can be time-intensive to operate although "one-shot" methods[7] are becoming more

commonplace. With the dominance of pulsed NMR techniques, continuous wave (CW) NMR has been consigned mainly to student experiments and use in high-sensitivity magnetometers. Although conceptually simpler, even with modern hardware, using CW NMR to determine relaxation parameters is not straight forward. However, the hardware for CW NMR can be an order of magnitude cheaper than a pulsed NMR system and requires significantly less power to operate. A standard CW NMR experiment involves measuring the radio frequency (RF) power absorbed by a sample although it is swept through resonance either by varying the magnetic field (typically using so-called sweep coils in addition to a static magnetic field as used here and shown in Figure 1) or varying the frequency of the RF source. So long as the rate of this sweep is short in comparison with T_2^*, the line width of the resulting dip in RF power can be used to determine T_2^*. This is possible in highly homogeneous fields, which are challenging to achieve whilst keeping the costs low and the system portable. For measurements of T_1, Look and Locker[8] utilised a fixed frequency and gated sweep waveform they called a "tone burst" where the sample was left aligned with the magnetic field but off resonance before the start of the measurement. Several cycles of the sweep coils follow during which each absorption trace was collected providing exponentially varying amplitudes with time constant T_1 until saturation was reached. More recently,[9] it was shown that a variation on this technique using a marginal oscillator could be used to produce a parameter related to T_1, which is termed T_x and that calibration samples could then be used to relate this to T_1. We refer to this technique as the Transient Effect Determination of Spin–Lattice (TEDSpiL) relaxation times. The use of inexpensive NdFeB magnets and low-cost microcontrollers to perform this have also been reported[10] giving the potential of a relatively inexpensive, low power, and portable system. This technique has the advantage of giving a value related to T_1 in under 5∼s compared with several minutes for pulsed determination of T_1 with traditional low-field hardware. In this work, we demonstrate that the parameter T_x can be used to screen for moisture changes in re-hydrated milk from powders that have absorbed different levels of moisture during storage.

2 | METHOD

2.1 | Equipment

The continuous-wave NMR sensor used comprises two 0.5T NbFeB magnets mounted on an iron yoke (562 11 Leybold Didactic GmbH, Germany) to generate a closed loop as shown in Figure 1. This arrangement provides a reasonably homogeneous field between the iron yokes corresponding to a larmor frequency for proton of 19.15∼Mhz. A commercial RF coil is incorporated within an RF shield and forms a resonant circuit along with a marginal oscillator (P/N 514 606 and 514 602, respectively, both parts Leybold Didactic GmbH, Germany). The setup also includes sweep coils to modulate the magnetic field. The RF power used to irradiate the sample is provided by the marginal oscillator unit and is fed into a microcontroller (Teensy 3.6, PJRC, OR, USA), which automatically fits the resulting peaks and displays the value of T_x on a serial LCD screen (further explained in 2.3). A second microcontroller (Teensy 3.5, PJRC, OR, USA) was utilised to generate the ramp voltage, which was amplified to drive the sweep coils. These sweep coils were set to 15∼V, providing an additional field between 0 and 13.5∼mT. Using the 0.3∼mT/K temperature drift reported,[11] this sweep range compensates for fluctuations in field caused by thermal drift. A further in-depth discussion of the measurement electronics has been reported.[12]

2.2 | Sample preparation

To measure the effect of milk powder concentration on measured T_x, 0.1% fat skimmed milk powder (Sainsbury's, UK) is mixed with distilled water to prepare test samples at

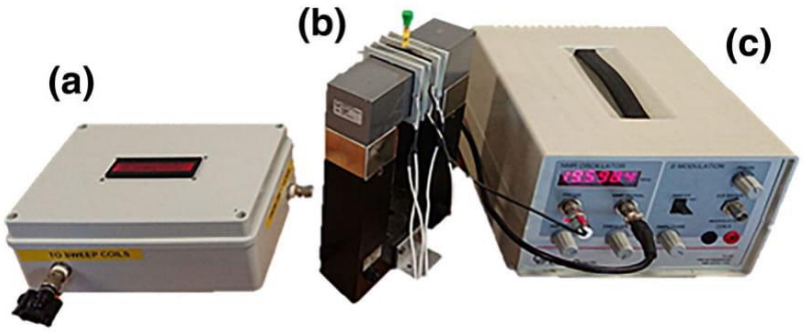

FIGURE 1 Cropped photograph of the experimental apparatus. (a) A plastic junction box housing the Teensy microcontrollers, MCP6002 inverting operational amplifier and batteries. (b) Nuclear magnetic resonance sensor and sweep coils. (c) Leybold Marginal Oscillator

six different concentrations (5%, 10%, 15%, 20%, 25%, and 30% w/v). These samples are loaded into NMR tubes before being placed into the CW sensor.

In order to measure the effect of moisture uptake by the milk powder on T_x, nine additional 5-g samples of 0.1% fat skimmed milk powder are loaded into lidless petri dishes and placed into a bench-top environmental chamber (3200, Thermotron, MI, USA) and subjected to various times under controlled humidity. The wetted powder is mixed with distilled water to a concentration of 40% w/v and moved to an ultrasound bath for 40∼min to ensure it had been reasonably degassed after mixing. The water in the ultrasound bath is replaced with fresh room temperature water every 10∼min to prevent heating the sample. These degassed samples are then loaded into NMR tubes before placing them into the CW sensor.

2.3 | Measurement

As the magnetic field is swept through resonance, an absorption event occurs characterised by a voltage change in the marginal oscillator (see example signal in Figure 2). These voltage values are passed into the analogue-to-digital converter (ADC) in the Teensy microcontroller converting it to an ADC number. The maximum magnitude value from each absorption peak is stored in an array. The maximum magnitude for each sweep is processed with a least squares fit[13] after it has been converted to a natural logarithm value by the microcontroller. This process provides a y=mx+c fitting where the gradient is assigned as the value of T_x for this specific sample. See Figure 2 for an example array of such data with the resulting fit.

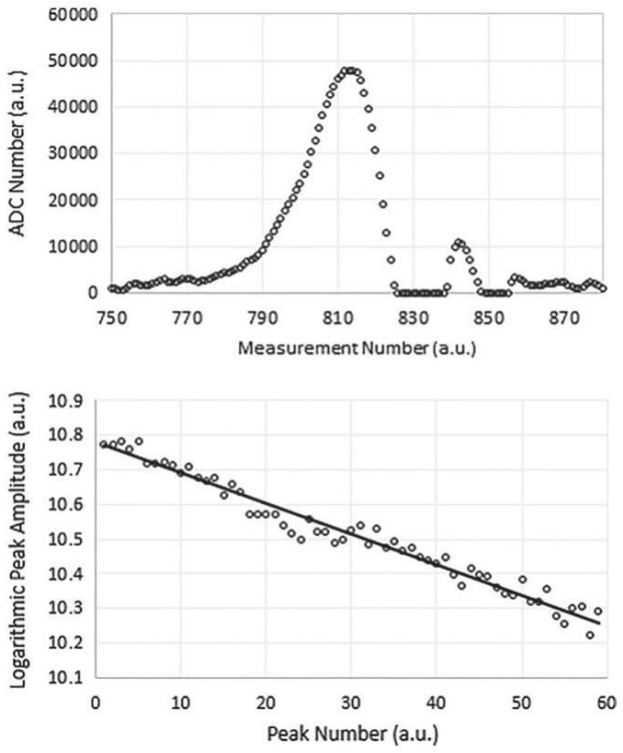

FIGURE 2 *Top* The analogue-to-digital converter values returned from the Teensy 3.6 for a single linear sweep through resonance. *Bottom* An example of the logarithmic peak values of water returned from the peak value array with a least squares fit. The gradient of the linear fit provides the numerical value to the parameter T_x

Longitudinal relaxation times are measured using a selection of the hydrated milk powder solutions using a 1.5T clinical whole body MRI scanner (Magnetom Avanto, Siemens, Germany). These samples were imaged using a series of images collected with different inversion times. Similar voxels from each scan form an exponential decay, which is fitted with in-house Matlab (Mathworks, USA) routines to produce a T_1 map.

3 | PRELIMINARY EXPERIMENTS

A 20-g sample of milk powder is stored in the environment chamber for 90-min to ensure a large uptake of moisture. Milk powder solutions are then made at varying concentrations (20%, 25%, 30%, 35%, and 40% w/v) with both the wet powder and a dry control powder. The T_x of each concentration was compared for the wet and dry powder solutions to decide on the appropriate concentration to be used for future experiments. For concentrations under 40% w/v, the difference in T_x values between the wet and dry samples is marginal, but at 40% w/v, the difference between wet and dry becomes significant. For this reason, 40% w/v solutions were used as the standard concentration for all future experiments.The data for this experiment are not shown.

A similar experiment is undertaken to find the most appropriate humidity value to which the powder should be exposed to give a good variation in moisture content in a reasonable time frame. A higher relative humidity corresponds to a faster uptake in atmospheric moisture as well as increasing the maximum amount of retained moisture. Samples are placed inside at 75%, 85%, and 95% relative humidity, all at 20°*C*. It was found that 85% relative humidity presents a good balance between maximum retained moisture and the rate of uptake and is used in future experiments. The data for this experiment are not shown.

Whilst the samples are being mixed with water, they become aerated, which causes an unknown and variable change in the spin–lattice relaxation time and hence T_x. It was found that placing the sample in an ultrasonic bath helped remove trapped air in the milk mixture assisting the reliability of measurements. A single cycle of 10∼min

in a 70-W ultrasonic jewellery cleaner bath removes a significant proportion of the additional gas, but it was found that after four such cycles (40~min total in ultrasonic bath) resulted in a plateau of signal and standard deviation. As such, all samples are sonicated for 40~min.

4 | RESULTS

The variation in T_x of solutions due to changes in the concentration of milk powder is demonstrated in Figure 3. Higher concentrations of milk powder in distilled water leads to an increase in viscosity due to the abundance of lactose, proteins, and fats, which is known to decrease spin–lattice relaxation times, [14,15] reproducing the results of Almazrouei et al.[16]

When powders that have been subjected to longer duration in a humid environment are made up into a 40% w/v concentration solution, the measured T_x decreases as can be seen in Figure 4. It is likely that this is simply due to

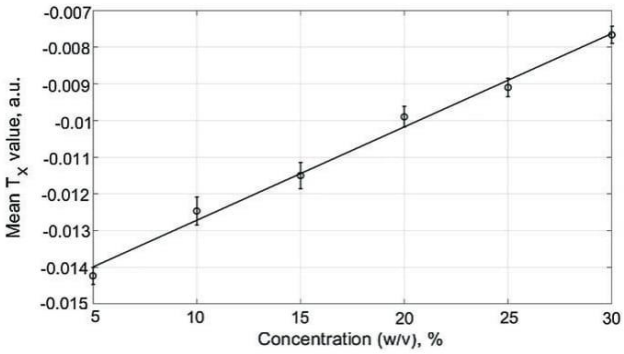

FIGURE 3 Continuous wave Tx values against the concentration of skimmed milk powder solutions using the continuous wave nuclear magnetic resonance apparatus. The gradient of the fit is $2.5E^{-4} a.u. \cdot \%^{-1}$ mass

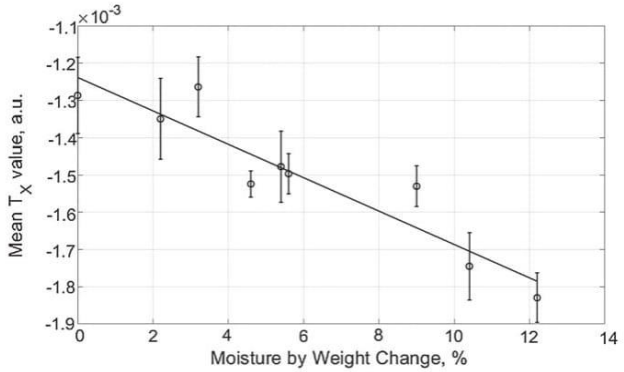

FIGURE 4 Continuous wave T_x values against percentage moisture of milk powder made into 40% w/v solutions. The gradient of the fit is $-4.5E^{-5} a.u. \cdot \%^{-1}$ moisture

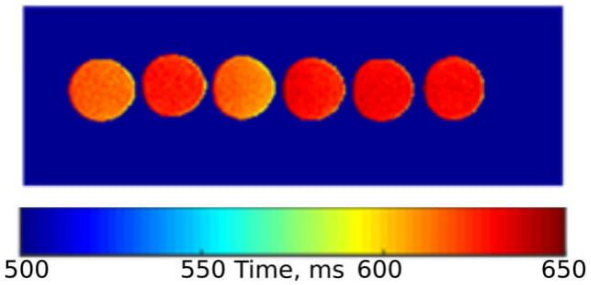

FIGURE 5 T1 map of milk powder solutions made from powders exposed to the humid environment chamber for (left to right) 0, 10, 20, 40, 60, and 90~min

less milk powder making up the 2-g weight, with some of it being water. As such, the true concentration will be lower than that which is measured. Through this concept, it is possible to create a calibration set of known moisture levels in milk powders and use it to measure the amount of water in an unknown sample (prepared with weight to volume) to ensure it has been successfully and appropriately dehydrated. Furthermore, this measurement would be suitable for quality assurance of products comprising powdered milk solutions.

The T_1 map described in the previous section is shown in Figure 5. It is found that the differences in T_1 is less than 50~ms and is outside the range, which is statistically differentiated by such a measurement suggesting an advantage in terms of the sensitivity of the CW NMR method in comparison with traditional pulsed imaging techniques.

5 | CONCLUSION

CW NMR has been demonstrated to distinguish between the moisture levels of skimmed milk powder when it is re-hydrated to a 40% solution by weight. The sensor and electronics used in this investigation are orders of magnitude cheaper than the industry standard of using an automated Karl Fischer titration system to measure the moisture level of the milk powder, proving a cost-effective analytical method that is easy and intuitive to use. All pieces of equipment and reagents were selected due to how readily purchasable they are requiring minimal modifications to rebuild a working system. A major advantage in using CW NMR with permanent magnets is that as the Larmor frequency is swept, frequency changes that could arise from the thermal drift of the NeFeB magnets can be compensated for, and therefore, the device does not need to undergo re-tuning or thermal control measures. Any extreme changes in temperature can be compensated for easily by changing the fundamental frequency of the marginal oscillator tank circuit, which is as simple as adjusting a variable capacitor. The sensitivity of CW

NMR has also been compared with mainstream pulsed imaging techniques showing that it can more easily distinguish between smaller changes in T_1 in this sample. This technique offers promise for online process monitoring for quality control purposes or as a stand-alone sampling system.

ACKNOWLEDGEMENTS

S. T. P. gratefully acknowledges Nottingham Trent University for funding under the Vice Chancellors Bursary Award. E. R. D. gratefully acknowledges Nottingham Trent University's 50/50 funded studentship with Diamond Light Source. N. K. A gratefully acknowledges the Ministry of Higher Education and Scientific Research (MOHESR) in the United Arab Emirates for funding and the Dubai Health Authority (DHA) for study leave.

CONFLICT OF INTEREST

There are no conflicts of interest for this work.

ORCID

Steven T. Parslow https://orcid.org/0000-0003-0861-6347
Robert H. Morris https://orcid.org/0000-0001-5511-3457

REFERENCES

[1] C. Reh, S. N. Bhat, S. Berrut, *Food Chem.* **2004**, *86*(3), 457. http://www.sciencedirect.com/science/article/pii/S0308814603005946

[2] H.-D. Isengard, *Food Chem.* **2008**, *106*(4), 1393. http://www.sciencedirect.com/science/article/pii/S0308814607005845, 4th International Workshop on Water in Foods.

[3] C. A. D. Caro, A. Aichert, C. M. Walter, *Food Control* **2001**, *12*(7), 431. http://www.sciencedirect.com/science/article/pii/S0956713501000202, Water Determination in Food - a Challenge for the Analysts.

[4] H.-D. Isengard, *Food Control* **2001**, *12*(7), 395. http://www.sciencedirect.com/science/article/pii/S0956713501000433, Water Determination in Food - a Challenge for the Analysts.

[5] J. Christie, I. G. Platt, in 2014 IEEE Sensors Applications Symposium (SAS), Queenstown, New Zealand, **2014**, 161.

[6] S. Rückold, K. H. Grobecker, H.-D. Isengard, *Fresenius J. Anal. Chem.* **2000**, *368*(5), 522. http://link.springer.com/10.1007/s002160000511

[7] T. B. Moraes, T. Monaretto, L. A. Colnago, *J. Magn. Reson.* **2016**, *270*, 1. https://www.sciencedirect.com/science/article/pii/S1090780716300957

[8] D. C. Look, D. R. Locker, *Phys. Rev. Lett.* **1968**, *20*, 987. https://link.aps.org/doi/10.1103/PhysRevLett.20.987

[9] R. H. Morris, N. Mostafa, S. Parslow, M. I. Newton, *Magn. Reson. Chem.* **2017**, *55*(9), 853. https://onlinelibrary.wiley.com/doi/abs/10.1002/mrc.4594

[10] M. I. Newton, E. A. Breeds, R. H. Morris, *Electronics* **2017**, *6*(4), 89. http://www.mdpi.com/2079-9292/6/4/89

[11] T. Hughes-Riley, E. R. Dye, D. O. Anderez, F. Hill-Casey, M. I. Newton, R. H. Morris, *Sens. Actuators, A Phys.* **2016**, *241*, 19–26. https://www.sciencedirect.com/science/article/pii/S0924424716300504

[12] S. T. Parslow, M. I. Newton, R. H. Morris, *Proceedings* **2019**, *4*(1), 21. https://www.mdpi.com/2504-3900/4/1/21

[13] W. H. Press, S. A. Teukolsky, W. T. Vetterling, B. P. Flannery **1992**.

[14] H. Todt, G. Guthausen, W. Burk, D. Schmalbein, A. Kamlowski, *Food Chem.* **2006**, *96*(3), 436.

[15] R. Colsenet, F. Mariette, M. Cambert, *J. Agric. Food Chem.* **2005**, *53*(17), 6784. https://doi.org/10.1021/jf050162k, PMID: 16104800.

[16] N. K. Almazrouei, M. I. Newton, E. R. Dye, R. H. Morris, *Proceedings* **2018**, *2*(3), 122. http://www.mdpi.com/2504-3900/2/3/122

How to cite this article: Parslow ST, Almazrouei NK, Newton MI, Dye ER, Morris RH. A preliminary study of milk powder hydration using TEDSpiL continuous wave NMR. *Magn Reson Chem*. 2019;1–5. https://doi.org/10.1002/mrc.4845

APPENDIX C: TABLE OF FIGURES